Nuclear Magnetic Resonance Logging

By

Howard Fred Sklar

B.S.E. Engineering Science
The University of Michigan, 1980

M.S. Physics
The University of Michigan, 1983

SUBMITTED TO THE DEPARTMENT OF EARTH ATMOSPHERIC AND PLANETARY SCIENCES IN PARTIAL FULFILLMENT OF THE REQUIREMENTS FOR THE DEGREE OF

MASTER OF SCIENCE IN EARTH AND PLANETARY SCIENCE
AT THE
MASSACHUSETTS INSTITUTE OF TECHNOLOGY

JUNE 1997

© 1997 Massachusetts Institute of Technology
All Rights Reserved

Signature of Author .....
Department of Earth Atmospheric and Planetary Sciences
May 1997

Certified By.....
M. Nafi Toksöz
Professor of Geophysics
Thesis Supervisor

Accepted by .....
Thomas H. Jordan
Department Head

ARCHIVES

MASSACHUSETTS INSTITUTE OF TECHNOLOGY

JUN 18 1997

LIBRARIES

NUCLEAR MAGNETIC RESONANCE LOGGING

By

HOWARD FRED SKLAR

Submitted to the Department of Earth Atmospheric and Planetary Sciences
On May 23, 1997, in partial fulfillment of the
Requirements for the Degree of Master of Science in
Earth and Planetary Science

ABSTRACT

The application of nuclear magnetic resonance (NMR) in petroleum well logging is rapidly expanding. A new generation of pulsed NMR tools, similar in technology to devices in used in medical imaging, is gaining wide acceptance in petroleum exploration. However, methods of NMR data collection and interpretation are not as mature in this application as in medicine; refinement is needed, in particular to maximize the benefit of a costly methodology. Herein is described a novel approach to formation evaluation in NMR well logging, enhanced by a nonconventional means of acquiring the logging data. Heretofore, both NMR and conventional logs (e.g., acoustic, density, neutron, gamma-ray, spontaneous potential) were analyzed as input into a gross water-saturation model based on resistivity. In the new evaluative approach, in contrast, the NMR measurements—pore size, free fluid, capillary-bound water, effective porosity, and direct hydrocarbon imaging—are the key parameters; resistivity and other logs are input into the NMR model. The effectiveness of this evaluation has been enabled by the development of specific pulse sequences to improve direct hydrocarbon imaging through imaging of pore fluids. The technique, representing an extension of the differential spectrum method, exploits T_1 and T_2 relaxation methods used effectively to improve tissue contrast in medical magnetic resonance imaging. In practical application, the NMR evaluative model with use of pore size has described many prolific geologic formations deemed nonproductive or marginal by conventional saturation models and analyses. Example novel NMR logs and evaluations are provided, as is a review of NMR physics and previous NMR and conventional formation evaluation models.

Thesis Supervisor: M. Nafi Toksöz

Title: Professor of Geophysics

Chapter 1
Introduction

1.1 Background

Purcell and Block first discovered nuclear magnetic resonance (NMR) in 1942, and won the 1952 Nobel Prize in Physics for their NMR work. The following half-century has seen many enhancements to the science of NMR and numerous well-established applications, including use in medicine through magnetic resonance imaging (MRI) and application in chemistry to crystallography and spectroscopy. NMR is used in a wide variety of the physical and biological sciences for both imaging and examining the magnetic properties of different types of materials. In the petroleum industry, mature NMR technology is robustly applied to geologic formation evaluation. This thesis will review the physics of NMR and the application of NMR to well logging.

NMR well logging has been tremendously advanced in the past few years, through, for example, higher resolution, an improved signal-to-noise ratio without the need to add paramagnetic salts to kill the water signal (dope) in the drilling mud, and the ability to image hydrocarbons directly. The key breakthrough in NMR well logging came in 1984, when J. A. Jackson at the Los Alamos National Laboratory developed a gradient field–pulsed NMR device (Jackson, 1984) similar to the MRI device used in the medical industry. The magnetic field used in the Jackson device is spatially varying: it falls off as $1/R^2$ (a dipole) as a function of distance from the tool. This is "inside–out" NMR, as opposed to the "outside–in" of medical MRI in which the patient is inside the magnet. The pulsed NMR logging tool uses a sequence of pulses of radio frequency (RF) energy to determine the properties of the material under study. The gradient field is used to select different slices of material and can be used to measure the diffusion of liquids and gas.

As described in the present thesis, NMR techniques developed in medicine can be successfully applied in well logging. The well data obtained through this extension can be used to predict petrophysical characteristics such as bound water, free fluid, and free hydrocarbons. It is also important to be able to predict the type of hydrocarbons in the formation as well as the permeability and producibility of the formation being studied. Furthermore, the data provide not just relative permeability, but a measure of permeability to within a factor of 2 (as opposed to, at best, permeability within a factor of 10 observed in previous down hole logging or sidewall coring measurements). The permeability value can be used as a very accurate measure of relative permeability from one zone to the next, even if the absolute numbers are not precise.

NMR well logging, including direct detection of hydrocarbons, may challenge resistivity as providing the best resolution between hydrocarbons and formation or filtrate water. In most situations with the resistivity approach, especially in shaley sands or certain complex carbonates, there are almost as many exceptions as there are illustrations of the rules. NMR logging might provide a more efficient method of prospecting for hydrocarbons.

Beyond low-resistivity situations, an important application of NMR is in low-contrast situations such as very tight formations or complex carbonates. In these cases, the productive hydrocarbon-bearing zones (pay) and water have almost identical characteristics in terms of resistivity, neutron, density, or sonic-type logging.

One of the most important measurements we make with NMR is bulk volume of irreducible fluids (BVI), so that not only porosity but also how much bound water is present in the pore space is known. In many cases, knowing the amount of bound water in the pore space is as important to any kind of saturation model as knowing what is in the pore space. There are often very high percentages of water; if all that water is bound, all the pore space left over may be free for hydrocarbons to move through. No other logging suite directly provides a pore size distribution or BVI.

In most cases in petroleum exploration, NMR provides a better method of imaging than resistivity. In many respects, however, NMR research is only now beginning in the petroleum industry, akin to the early MRI research in medicine ten years ago. We need to develop new pulse sequences to enhance resolution and to better define hydrocarbons and pore size along with porosity, permeability, and mobility of fluids.

1.2 Outline

Chapter 2 discusses the physics of NMR. It covers the classical description of the physical process of NMR, as well as proton precession and the NMR experiment. The important parameters used to measure relaxation of spins T_1 and T_2 are discussed. The Carr–Purcell–Meiboom-Gill (CPMG) pulse sequence (Carr and Purcell 1954; Meiboom and Gill, 1958) is explained in detail.

Chapter 3 addresses the specific measurements of NMR applied to well logging. The key petrophysical parameters used in NMR are bound water, (or bulk volume irreducible, BVI) and free fluid (as the free fluid index, FFI) in the pore space. Also measured are effective porosity (MPHI), NMR-derived permeability (MPERM), and pore size distribution.

In Chapter 4, some of the main tools used in NMR well logging are presented. The first tool described is the nuclear magnetic log (NML), the original NMR logging device and the predecessor of modern NMR logging tools. Many of the data presented in this thesis were acquired with the magnetic resonance imaging log (MRIL-C) tool of the NUMAR Corporation. The second of the modern commercially available tools described is the Schlumberger combinable magnetic resonance (CMR) logging tool. The three tools are compared and their physical descriptions are given.

Chapter 5 begins with examples of the customary role of NMR in formation evaluation. The data are presented as processed by the NUMAR MRIAN (magnetic

resonance imaging analysis) program (Coates et al., 1994). How the data curves are used to determine a basic interpretation model is explained. From these data, a novel way of evaluating formations using the NMR measurements as the key input into the model is developed. Saturation models, and how the NMR parameters are incorporated into these models, are described. A sensitivity analysis of the measurements leads to the optimum acquisition of NMR logs.

Chapter 6 describes direct hydrocarbon imaging and its application to formation evaluation. The method involves designing specific pulse sequences to detect the amount of hydrocarbons in the pores, and whether they are gas or oil. Also, it is necessary to determine whether there is movable water in the pores, and how the method can be refined. The chapter covers T_1 and T_2 relaxation mechanisms, in relation to pore fluids, and how to exploit their contrasts to better image hydrocarbons. Log examples and interpretations are given to complete the thesis NMR-based method of formation evaluation.

Chapter 7 concludes the thesis through summary and discussion of future directions. Historically, NMR, nuclear logging (including porosity, density, and gamma ray), and core work were all inputs into a gross water-saturation model based on resistivity logging. Now, we can define a new method of formation evaluation based on pore size, BVI, and effective porosity, as well as direct hydrocarbon detection using NMR. In this NMR-based model, resistivity and the other conventional logging measurements are secondary rather than primary inputs. The future holds much promise for development of NMR logging. There may be a paradigm shift from resistivity-based water-saturation models to direct detection of hydrocarbons using NMR.

In summary, Chapters 2 through 4 provide background on NMR in general and in specific applications in well logging; Chapters 5 and 6 describe the original work of this thesis, in development of a novel formation evaluation model and improved direct hydrocarbon imaging, respectively; and Chapter 7 recaps the thesis work and points to directions in research.

Chapter 2

Nuclear Magnetic Resonance Physics

This chapter examines the physical background of NMR. It describes Larmor precession, which is the precession of a magnetic moment about a constant magnetic field. The basic NMR experiment is described, and a classical derivation of the Larmor frequency is given. The longitudinal (T_1) and transverse (T_2) relaxations, the principal measurements we make in NMR, are described. Also, other experimental NMR parameters such as echo time (T_E), wait time (T_W), repeat time (T_R), and free induction decay (FID) are shown. The Carr–Purcell–Meiboom–Gill pulse sequence (CPMG), which is used in medical imaging as well as in modern NMR well logging, is described.

2.1 Larmor Precession

The concept of NMR begins with $\mathbf{B_0}$, a constant magnetic field, and $\boldsymbol{\mu}$, a net magnetic moment, (the spins of hydrogen nuclei in water). Each of these magnetic moments will start to precess at a certain frequency, ν, around the constant magnetic field $\mathbf{B_0}$ (Figure 2.1). The direction of precession is the same as the direction of the torque $\boldsymbol{\tau}$, equal to $\boldsymbol{\mu}$ **X B**, in which the spins precess around the constant magnetic field. That frequency, the Larmor frequency, is ν. It is equal to the gyromagnetic ratio, γ, divided by 2π, multiplied by the magnitude of the constant magnetic field, $\mathbf{B_0}$:

$$\nu = (\gamma/2\pi)\, B_0 \tag{2.1}$$

The magnetic moment, $\boldsymbol{\mu}$, and the magnetic field, $\mathbf{B_0}$, are brought in contact with each other. Note in Figure 2.1 the direction of the precession. There is a positive constant magnetic field and a positive magnetic moment in the direction $\boldsymbol{\mu}$ **X B**; in this case, it would

be clockwise, looking down into the field.

2.2 The Nuclear Magnetic Resonance Experiment

The basic NMR experiment (Figure 2.2) begins with a number of protons that have magnetic moments randomly distributed in space (in this case, hydrogen atoms in water), which are brought in contact with a constant magnetic field, $\mathbf{B_0}$. As these protons come in contact with the constant magnetic field, they begin to precess around the magnetic field at the Larmor frequency, ν.

In addition to the constant magnetic field, a sinusoidally varying magnetic field, $\mathbf{B_1}$, perpendicular to $\mathbf{B_0}$, is applied. In Figure 2.2, since the constant magnetic field is in the z direction, the magnetic field $\mathbf{B_1}$ will be applied in the x direction. Application of the second magnetic field will cause the spins to flip. The spins begin in a net positive z direction, but when $\mathbf{B_1}$ is applied for a specified duration, the spins tip into the x–y (transverse) plane. Tipped into the transverse plane, they will still precess at the Larmor frequency about the z axis.

2.2.1 Net Magnetization

When a large number of magnetic moments begin to precess around the constant magnetic field, $\mathbf{B_0}$, these moments can be summed into a single vector, the net magnetization, or the single vector $\mathbf{M_0}$ (Figure 2.3). $\mathbf{M_0}$ points in the z direction, parallel to $\mathbf{B_0}$. In other words, the net effect of all the spins precessing about the z axis can be represented as the single spin $\mathbf{M_0}$. The purpose of the second magnetic field, $\mathbf{B_1}$, is to flip the net magnetization 90° (Figure 2.4). A field, $\mathbf{B_1}$, is applied in the x direction, which causes $\mathbf{M_0}$ to precess in the y–z plane about $\mathbf{B_1}$.

The Larmor frequency is equal to the number of cycles per second that a given spin precesses about a magnetic field. The Larmor period (T) is the amount of time in seconds

for one cycle, or the inverse of the frequency. Therefore, a 90° spin–flip would be equal to 1/4 of a Larmor period. If $\mathbf{B_1}$ were applied for 1/4 of the Larmor period, the net magnetization would precess 90° in the y–z plane and would point in the y direction.

$$\nu = (\gamma/2\pi)\, B_1 \tag{2.2}$$

$$T = 1/\nu \tag{2.3}$$

$$\theta = \gamma\, B_1\, t \tag{2.4}$$

In Equations 2.2 and 2.4, $\mathbf{B_1}$ is used because the Larmor precession of $\mathbf{M_0}$ about $\mathbf{B_1}$ is of interest, whereas in Equation 2.1, the Larmor frequency is proportional to $\mathbf{B_0}$. Equation 2.2 is the Larmor period for a spin that precesses about the $\mathbf{B_1}$ axis for one cycle. In Equation 2.4, the flip angle θ is shown to be proportional to the Larmor frequency multiplied by time (t). A 90° spin–flip occurs when θ is equal to $\pi/2$ and t is solved for in Equation 2.4. A 180° spin–flip occurs when θ is equal to π and t is solved for, that is, in twice the time as the 90° case.

2.2.2 Rotating Reference Frame

To understand the rotating reference frame, begin with an RF antenna, which is a coil of wire aligned to be perpendicular to the rotating net magnetization. This is similar to a coil of wire whose axis is in the x direction (Figure 2.5), which has a magnet in front of it that is spinning in the x–y plane. The magnet is spinning at the Larmor frequency; thus, it will induce a sinusoidally varying current in the coil, which is also at the Larmor frequency.

Another way of looking at this experiment is to begin with a sinusoidally varying current in the RF coil, with an axis of symmetry in the x direction. A magnetic field is created that is sinusoidally varying, also in the x direction. It can be seen from the two examples above that there is reciprocity between the two scenarios. If we stand in the laboratory frame of reference looking down the axis of the coil and see a magnet spinning at

the Larmor frequency, we will see a magnetic field that is varying sinusoidally along the x axis. We also see, in this frame of reference, an alternating current induced in the RF coil.

A varying magnetic field in the laboratory frame is seen as a constant magnetic field moving with the net magnetization in the rotating reference frame. A constant magnetization moving in the rotating reference frame is seen as a varying magnetic field in the laboratory frame. From the above reciprocity, an RF coil with an alternating current will create a magnetic field that is varying in the laboratory frame in the x direction. In the frame of reference in which there is rotation at the Larmor frequency with the net magnetization $\mathbf{M}_0$, the magnetic field is seen as constant in the x′ direction. It is a matter of reference frame to say whether there is a constant magnetic field rotating with the particle or an RF field continually varying in the laboratory frame.

Thus, an RF pulse in the x direction is seen as a constant magnetic field in the x′ direction in the rotating frame. The net magnetization in the rotating reference frame, which points in the z′ direction, will now precess about the magnetic field $\mathbf{B}_1$, which is constant in the rotating frame. If the magnetic field $\mathbf{B}_1$ is turned off after the net magnetization has gone through 1/4 of a Larmor period around $\mathbf{B}_1$, it will have been tipped 90° in the y′ direction. This is a 90° RF pulse because the net magnetization has been tipped by 90°, and now the spins are precessing about the z axis in the transverse x–y plane at the Larmor frequency (Figure 2.6). The motion of the net magnetization in the laboratory frame is seen as a beehive (Figure 2.7).

2.3 Classical Derivation of the Larmor Frequency

Next is described the classical derivation of the Larmor frequency (Feynman et al., 1965). As seen in Figure 2.8, a particle with mass m and charge q is moving with a tangential velocity **v** in a circle of radius **r**.

The angular momentum, **J**, of a particle of mass m is defined as

$$\mathbf{J} = \mathbf{r} \mathbf{X} \mathbf{p} \tag{2.5}$$

where **r** is the radius vector and **p** is the momentum vector, which is perpendicular to the circle, and **p** is equal to mv. The direction of **J** is up and is perpendicular to the plane of rotation of the particle with mass m.

Next, because a charged particle is rotating in a circle, the particle not only has angular momentum, but also has a magnetic moment, $\boldsymbol{\mu}$.

The magnetic moment of an orbiting charged particle is the current it generates times the area of the circle in which it is moving. So,

$$\boldsymbol{\mu} = \mathrm{I}\, \mathbf{a} \tag{2.6}$$

where **a** in this case is πr^2. The current, I, is measured by the number of coulombs that travel by a certain point per second. Current is given in amperes, equal to coulombs per second. In this case, that would be

$$\mathrm{I} = \mathrm{q}\, \nu \tag{2.7}$$

that is, the charge, q, in coulombs times the frequency, ν, in inverse seconds.

The frequency of a particle moving around in a circle with the tangential speed v is the velocity divided by the distance around the circle. The frequency is

$$\nu = \mathrm{v}/2\pi r \tag{2.8}$$

Plugging Equation 2.8 (for frequency) into Equation 2.7 (for current) and plugging that into Equation 2.6 (for magnetic moment), yields

$$\boldsymbol{\mu} = \mathrm{qvr} / 2 \tag{2.9}$$

Since $\mathbf{J} = mvr$, $vr = J/m$. Plugging this into the equation for μ shows proportionality between μ and $\mathbf{J}$. The relation between the magnetic moment, μ, and the angular momentum, $\mathbf{J}$, of a charged particle moving around in a circle is

$$\mu = g\,(q/2\,m)\,\mathbf{J} \tag{2.10}$$

The additional factor, g, or the Landé g factor, is a quantum mechanical effect that can be calculated or measured. In other words, it is a quantum mechanical constant that relates μ to $\mathbf{J}$. In some cases it would be 1; in others it would be 2. In this case, it is 5.6. Thus, a general relation for a charged particle orbiting in a circle has been derived; γ, which is equal to g (q/2m) is the gyromagnetic ratio and relates the angular momentum, $\mathbf{J}$, to the magnetic moment, μ.

To continue the derivation of the Larmor frequency, see Figure 2.9. The protons with angular momentum $\mathbf{J}$ and magnetic moment μ are precessing about the magnetic field $\mathbf{B}$ at an angular frequency of ω. The vector $\mathbf{J}$ precesses about the magnetic field $\mathbf{B}$ at an angular velocity ω; therefore, the change in angle is $\Delta\theta$.

$$\Delta\theta = \omega\,\Delta t \tag{2.11}$$

As the vector moves from $\mathbf{J}$ to $\mathbf{J}'$ through the angle $\Delta\theta$,

$$\Delta\,\mathbf{J} = \mathbf{J}\sin\theta\,\Delta\theta \tag{2.12}$$

From Equations 2.11 and 2.12, it is seen that the time rate of change of the angular momentum vector is

$$d\mathbf{J}/dt = \omega\,\mathbf{J}\sin\theta \tag{2.13}$$

A magnetic moment μ in an external magnetic field $\mathbf{B}$ experiences torque τ that causes μ to precess about $\mathbf{B}$.

$$\tau = \mu \mathbf{X} \mathbf{B} \tag{2.14}$$

By definition a torque is equal to the time rate of change of angular momentum dJ/dt. So, from Equations 2.13 and 2.14 it is seen that

$$\tau = \mu \mathbf{B} \sin\theta = \omega \mathbf{J} \sin\theta \tag{2.15}$$

Equation 2.15 can now be solved for the angular frequency ω:

$$\omega = \mu \mathbf{B}/\mathbf{J} \tag{2.16}$$

From Equation 2.10, however, it is known that μ/J is equal to g(q/2m) or γ. From the above derivation, the angular velocity, ω, can be described by γ and **B**, the strength of the magnetic field:

$$\omega = \gamma \mathbf{B} \tag{2.17}$$

From the above derivation the Larmor frequency can be rewritten as

$$\omega = g(q/2m)\,\mathbf{B} \tag{2.18}$$

that is, an equation in terms of known constants except for g (Figure 2.10). For the case of hydrogen in water, g = 5.5847, q = 1.60217733 E-19 C and m = 1.6726231 E-27 kg. Using these numbers in Equation 2.18 yields

$$\nu = 4257\ \mathrm{B\ Hz} \tag{2.19}$$

where the Larmor frequency, ν, is equal to ω/2π. The Larmor frequency is proportional to the strength of the magnetic field B and equal to 4257 Hz per gauss. The only quantum mechanical value requiring measurement was the Landé g factor. All the other constants were from the classical derivation of a magnetic moment precessing in an external magnetic field.

2.4 Nuclear Magnetic Resonance Parameters

This section describes the basic parameters of NMR: longitudinal relaxation (T_1), transverse relaxation (T_2), echo time (T_E), time to repeat (T_R), wait time (T_W), and free induction decay (FID). The most important measurement made by NMR is the relaxation time. Relaxation time is the parameter that relates to the mobility of hydrogen protons in water or hydrocarbon. Relaxation time in medical imaging can be related to free water in tissue or water bound in fats. Relaxation time of protons in porous media can be related to pore size, allowing discrimination of whether the water in the pores is free or capillary bound (irreducible).

2.4.1 T_1 (Longitudinal Relaxation)

When a constant magnetic field moves into a given region in space, protons will start to precess around that constant magnetic field. The amount of time that it takes these protons, once they are exposed to the magnetic field, to begin precessing at the Larmor frequency is called the longitudinal relaxation, or T_1 (also described as the spin–lattice interaction). This recovery time can be described mathematically as

$$M(t) = M_0 (1 - e^{-t/T_1}) \tag{2.20}$$

where M(t) is the net magnetization in the direction of $\mathbf{B_0}$, or z. This describes T_1 (Figure 2.11) as the amount of time it takes for the net magnetization to be recovered 63.2% in the direction of $\mathbf{B_0}$.

2.4.2 T_2 (Transverse Relaxation)

After the protons have all recovered in the z, or longitudinal, direction, the next step in the NMR experiment is to tip them by 90° into the x–y, or transverse, plane. This is done by applying the RF pulse in the x direction ($\mathbf{B_1}$). After the application of the 90° RF pulse, the protons will precess in the transverse plane at the Larmor frequency, ν, about the

constant magnetic field, $\mathbf{B_0}$, in the z direction.

T_2 is the transverse relaxation time (or spin–spin interaction). It is the amount of time it takes the spins to relax from precessing once they have been tipped by the 90^0 RF pulse into the transverse plane. This can be shown as

$$M_{XY}(t) = M_0 \, e^{-t/T_2} \tag{2.21}$$

This process can be thought of as a loss of magnetization in the x–y (transverse) plane due to spin–spin interactions (Figure 2.12). The above description of the two relaxation mechanisms T_1 and T_2 are the fundamental measurements made with NMR. The NMR experiment can now be restated in terms of T_1 and T_2. Begin with a permanent magnetic field $\mathbf{B_0}$ in the z direction; the protons recover at a rate of T1. Next, apply an RF pulse $\mathbf{B_1}$ in the x direction, causing the net magnetization M_0 to flip 90° into the transverse plane. T_2 is the rate of decay of the net magnetization M_0 in the transverse plane, due to spin-spin interactions.

2.4.3 Dephasing after the Radio Frequency Pulse

Dephasing is well reviewed by Keller (1988). After $\mathbf{B_1}$ is applied, all the protons are in phase in the transverse plane, precessing at the Larmor frequency about $\mathbf{B_0}$. As indicated in Figure 2.13a, the net magnetization, which is initially in the z direction, is tipped by 90° into the y direction. This net magnetization will precess in the transverse plane at the Larmor frequency, ω (in radians per second). The spins will begin to lose phase coherence (dephase), as shown in Figure 2.13, b–d, because no material will have a magnetic field that is 100% constant. The Larmor frequency is linearly proportional to the magnetic field; because the field is not constant, some spins will precess faster than others. When the field is larger, spins will precess faster. As seen in Figure 2.13e, if nothing else is done after the 90° RF pulse, the spins will completely dephase.

2.4.4 Free Induction Decay

A great response is seen in the RF coil because the spins, as they precess, induce a current in the coil. The greatest current is induced if most or all of them are spinning around coherently. As the spins dephase, however, the magnetic field begins to be lost. As the field becomes less coherent, less current is induced and free induction decay (FID) occurs (Figure 2.14).

FID is defined as decay of the signal amplitude (A) at the time constant T_2^* during dephasing after a 90° RF pulse:

$$A(t) = e^{-t/T_2^*} \tag{2.22}$$

The free induction decay (FID) (Figure 2.14) shows a signal amplitude that decays away with a time constant of T_2^*. The FID is a combination of a sine wave with frequency equal to the Larmor Frequency and a decaying envelope with time constant T_2^*.

The difficulty with the free induction decay is that dephasing is a combination of the effects of the transverse relaxation T_2 and the magnetic field that is not totally homogenous. The problem posed by FID in NMR imaging is the difficulty in describing T_2 when T_2^* is present. Although maximum amplitude (A_0) can be related to some properties of the material under study, the key information needed is T_2. To measure T_2 accurately, dephasing after the 90° RF pulse needs to be impeded.

2.4.5 Carr–Purcell–Meiboom–Gill Pulse Sequence

A solution for impeding the spins' dephasing was provided by a sequence of pulses developed by Carr, Purcell, Meiboom, and Gill (Carr and Purcell, 1954; Meiboom and Gill, 1958), named the CPMG pulse sequence for them. The CPMG pulse sequence is the

cornerstone of NMR used in medical imaging and in the physical and biological sciences and technologies. Its effect is summarized in Figure 2.15.

After a 90° RF pulse is applied, the spins are initially in phase (Figure 2.15a). The spins will start to dephase, some spinning faster and others spinning slower according to whether they are in stronger or weaker magnetic fields (Figure 2.15b). In the laboratory frame, they are all spinning clockwise around the magnetic field and at approximately the Larmor frequency.

After a time ($T_E/2$, where T_E is the time to echo), the pulses have been allowed to dephase to an extent (Figure 2.15b). At this point in the CPMG solution a 180° RF pulse is applied (Figure 2.15c), which causes the spins to be rotated 180° about a fixed axis. For the 180° tipping, the pulse is applied for twice as long as for 90° tipping. The spins continue to precess clockwise, but the fast spins now lag behind the slow spins (Figure 2.15d). As time goes on, the former begins to catch up with the latter (Figure 2.15e). After a time ($T_E/2$), all the spins are again in phase; this coherency of spins creates a pulse echo (Figure 2.15f).

After the first echo the spins begin to dephase once again. After $T_E/2$, another 180° RF pulse is applied, as before (Figure 2.16). After $T_E/2$, the spins are again in phase for a second pulse echo. The process is repeated continually until the experiment is ended, with the number of required echoes recorded. With each succeeding echo, the amplitude diminishes; each echo is associated with an FID (Figure 2.16). The time between echoes (time to echo or T_E) equals the time between 180° RF pulses. The envelope of the first spin echo decays at a rate of T_2, and each echo decays in an FID at a rate of T_2^*.

The final part of the CPMG pulse sequence is a wait time (T_W) to enable the spins to recover (i.e., to become polarized in the longitudinal, or $\mathbf{B_0}$, direction) before the next experiment is begun. Thus, the CPMG pulse sequence consists of a 90° RF pulse followed by a number (N) of 180° RF pulses and, finally, time (T_W) to allow the spins to realign with

the constant magnetic field. The total time between NMR experiments is the amount of time between successive 90° RF pulses and is given as T_R, or time to repeat. Thus, the following equation applies to the CPMG pulse sequence:

$$T_R = N\,T_E + T_W \tag{2.23}$$

Because the CPMG pulse sequence causes the spins to remain in the transverse plane, it allows measurement of T_2. The data from typical NMR well logging experiments are shown in Figure 2.17. The amplitude of each echo is scaled in porosity units, and the height of the first echo can be related to the total effective porosity (see Section 3.1). The figure does not show T_W, which would be determined by the T_1 of the sample. After the required wait time, the experiment can be repeated as many times as necessary to achieve an appropriately high signal-to-noise ratio. (In well logging applications, three experiments are normally run for each foot logged, with a running average of 8 to 12 adjacent experiments for each data point. The aperture of resolution will be about 2 ft using these parameters.)

The CPMG pulse sequence, one of many key pulse sequences used in NMR (Abragam, 1961), is the most widely used in logging applications and in medical imaging. The measurement made with CPMG is T_2 in a continuous mode. To measure T_1, a saturation-recovery pulse sequence is needed. (In many instances in well logging, T_1 measurement is not practical because a station stop is required. In many formations, a logging tool that is not moving is at high risk for becoming differentially stuck.)

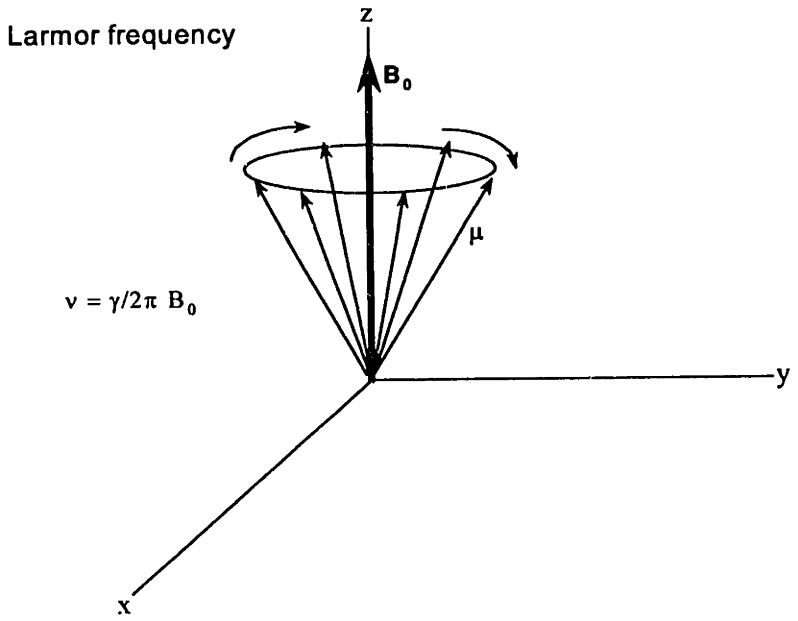

Figure 2.1 The precession of magnetic moments (μ) about a constant magnetic field ($\mathbf{B_0}$) is illustrated.

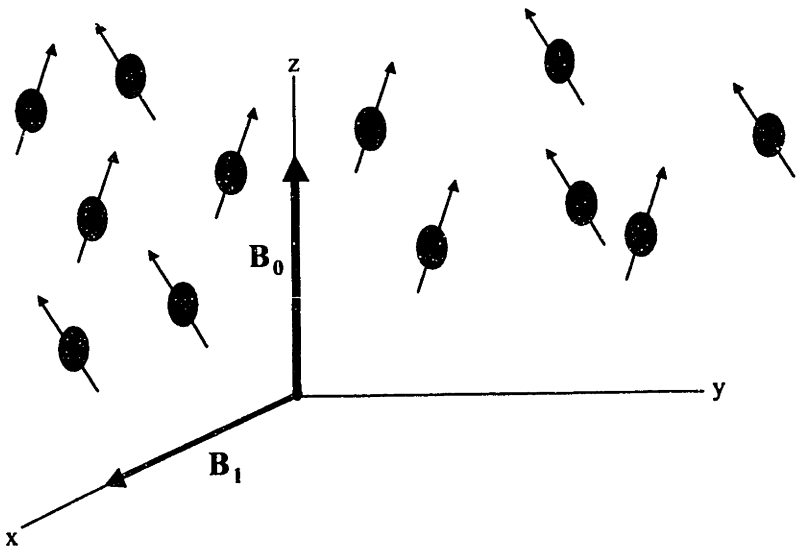

Figure 2.2 Spins in a constant magnetic field, $\mathbf{B_0}$, are tipped into the transverse plane by an RF pulse of $\mathbf{B_1}$ in the x direction.

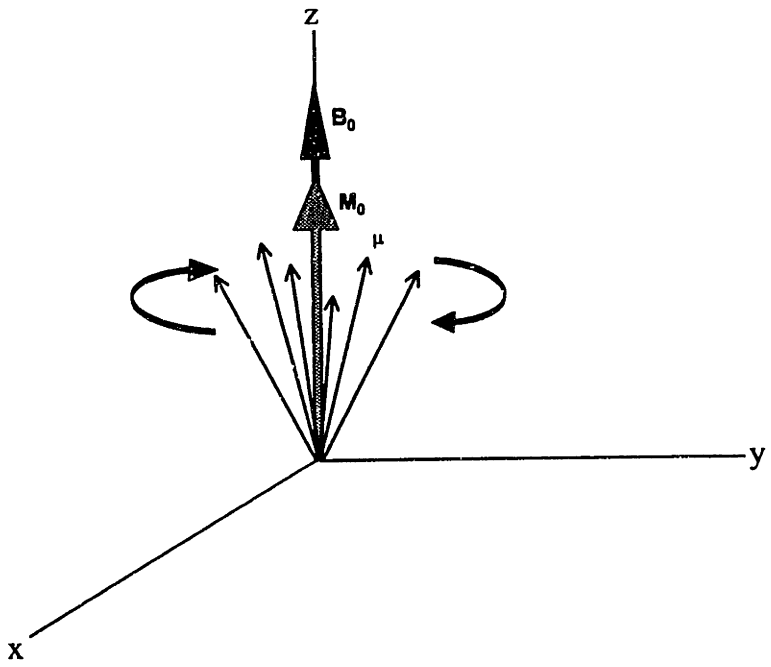

Figure 2.3 The sum of the spins μ precessing about the constant magnetic field, $\mathbf{B_0}$, add up to give $\mathbf{M_0}$, the net magnetization in the z direction.

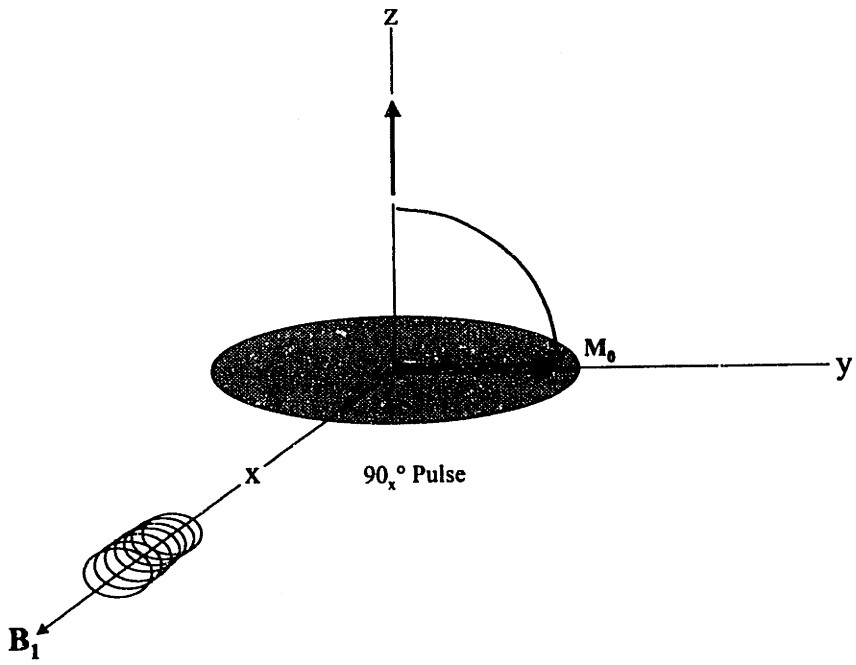

Figure 2.4 The magnetic field $\mathbf{B_1}$ is pulsed in the x direction to tip the net magnetization 90° into the transverse plane.

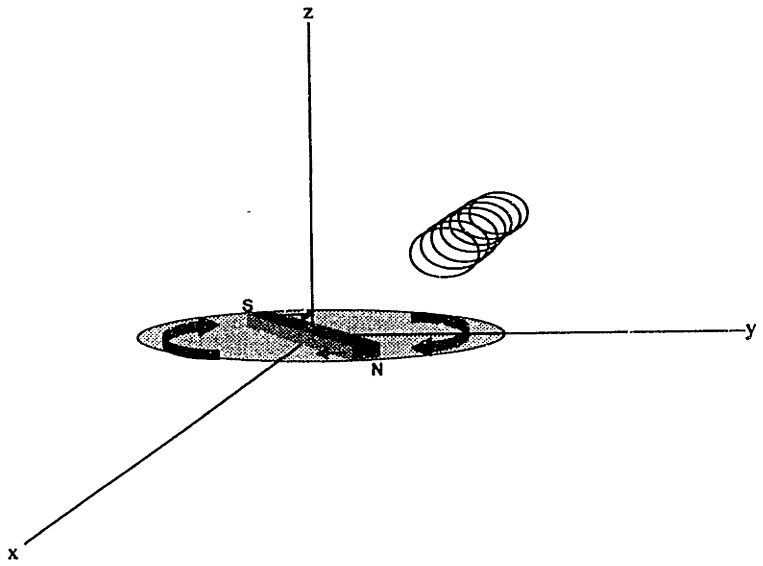

Figure 2.5 The magnet is spinning in the x–y plane at the Larmor frequency, in front of a coil that is oriented along the x axis.

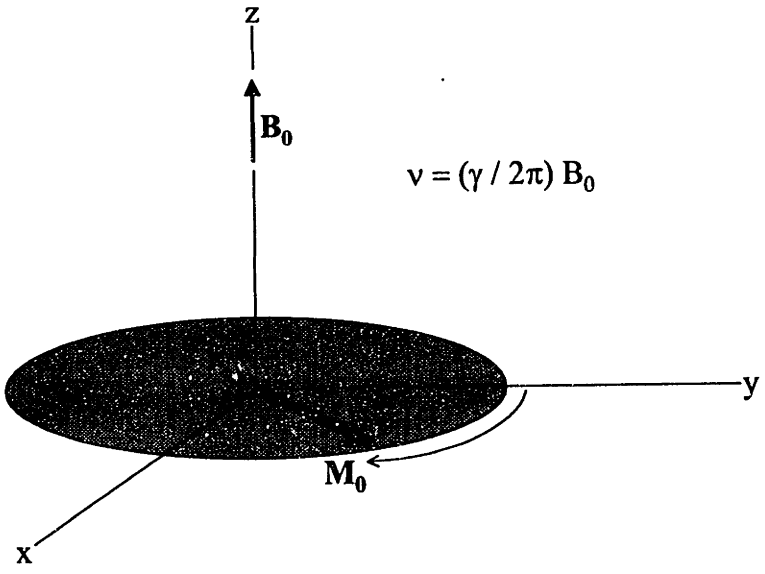

Figure 2.6 The net magnetization, M_0, has been tipped 90° and the spins are now precessing in the transverse (x–y) plane at the Larmor frequency.

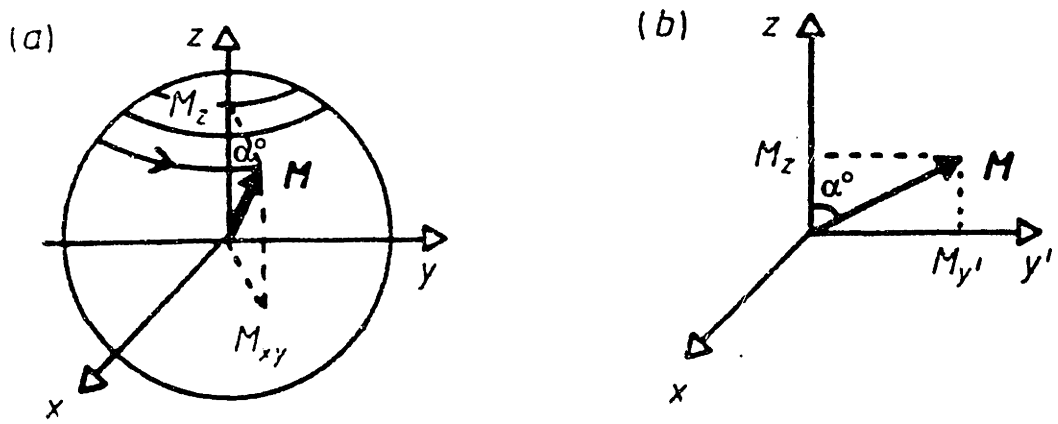

Figure 2.7 The motion of the net magnetization **M** after an α° RF pulse is seen (a) in the laboratory frame as a beehive, and (b) as a spin–flip of α° in the rotating reference frame. From Leach, 1988.

$J = mvr$

$\mu = I\,a$

$a = \pi r^2$

$I = q\,\nu$

$\nu = v/2\pi r$

$\mu = qvr/2$

g = Lande' g-factor

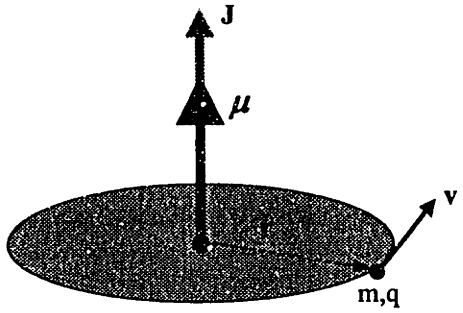

$$\mu = g\left(\frac{q}{2m}\right)J$$

Figure 2.8 The magnetic moment, μ, and angular momentum, **J**, of a particle of mass m and charge q orbiting in a circle of radius **r** are illustrated. The gyromagnetic ratio is equal to g(q/2m). From Feynman et al., 1965.

$\Delta\theta = \omega\Delta t$

$\Delta J = J \sin\theta\ \Delta\theta$

$d\mathbf{J}/dt = \omega\,\mathbf{J}\sin\theta$

$\tau = \mu\, x\, \mathbf{B} = d\mathbf{J}/dt$

$\tau = \mu\, B \sin\theta = \omega\, J \sin\theta$

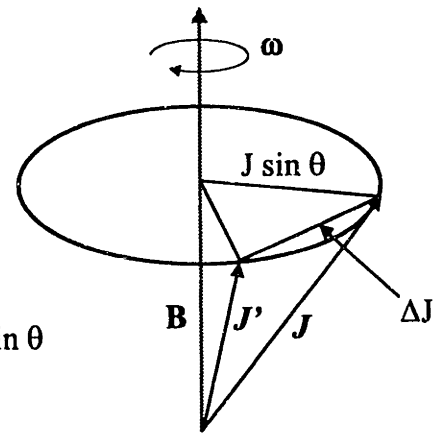

$$\boldsymbol{\omega = \mu\, B / J} \qquad \therefore\ \omega = g\left(\frac{q}{2m}\right)B$$

Figure 2.9 The torque, τ, is equal to μ **X B**, or also equal to the time rate of change of angular momentum, d**J**/dt; therefore, the Larmor precession frequency (ω) equals μ**B/J**. Working from $\mu = g(q/2m)$ **J** (Equation 2.10), $\omega = g(q/2m)$**B**. From Feynman et al., 1965.

$$\omega = g\,(q/2m)\,B \qquad g = 5.5847$$

$$\omega = \gamma\,B \qquad q = 1.60217733\ \text{E-19 C}$$

$$\nu = (\gamma / 2\pi)\,B \qquad m = 1.6726231\ \text{E-27 kg}$$

$$\nu = 4257\ B \quad \text{Hz}$$

Figure 2.10 The Larmor frequency for hydrogen in water is equal to 4257 Hz per gauss of magnetic field B. This is in terms of the physical constants q (the charge) and m (the mass) of a proton. The Landé g-factor is the only quantum mechanical constant in the equations.

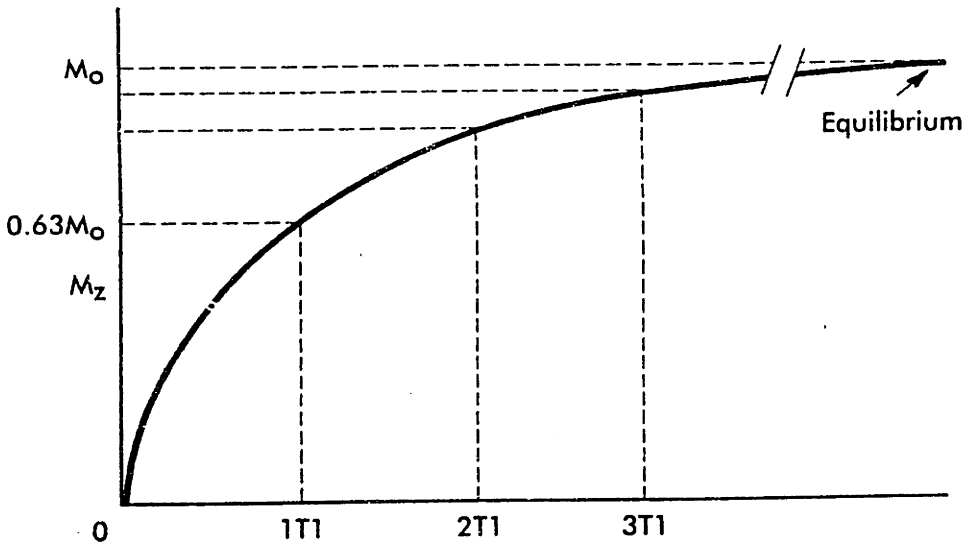

Figure 2.11 T_1 (relaxation time, or spin–lattice interaction) is equal to the amount of time it takes for the longitudinal magnetization $\mathbf{M_Z}$, to recover 63% of the net magnetization, $\mathbf{M_0}$. From Bushong, 1996.

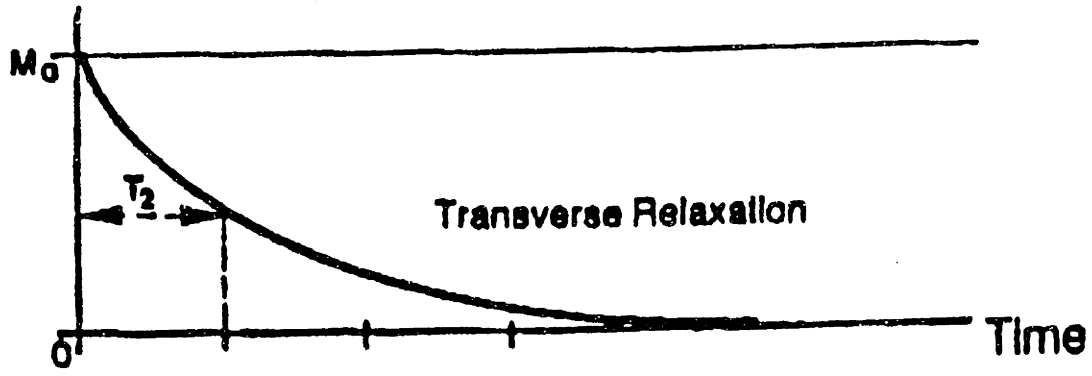

Figure 2.12 T_2 (relaxation time, or spin–spin interaction) is the time it takes for the transverse magnetization, $\mathbf{M_{XY}}$, to decay down to 37% of the maximum value, $\mathbf{M_0}$. From Miller et al., 1990.

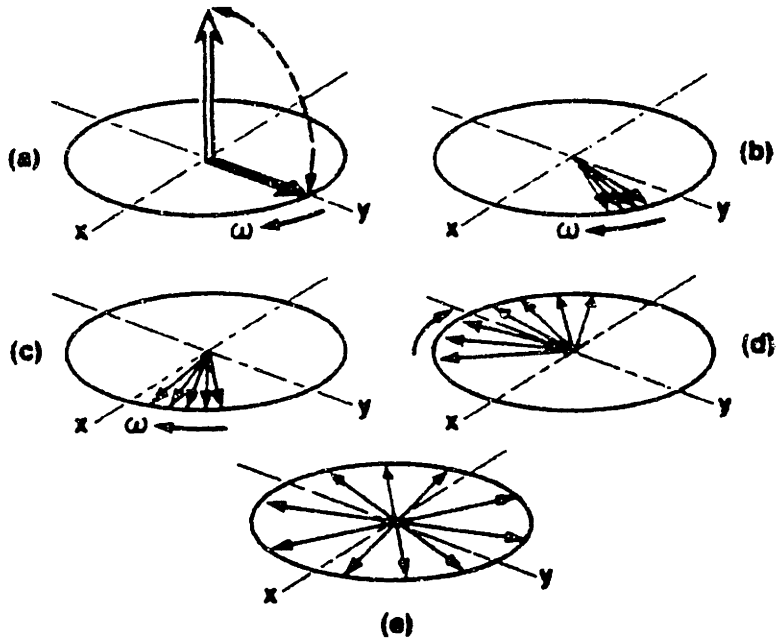

Figure 2.13 In (a), a 90° RF pulse tips the net magnetization into the transverse (x–y) plane. In (b) through (d), the spins start to dephase because of nonhomogeneity of the constant magnetic field B_0. In (e), the loss of phase coherence leads to total cancellation of the signal. From Keller, 1988.

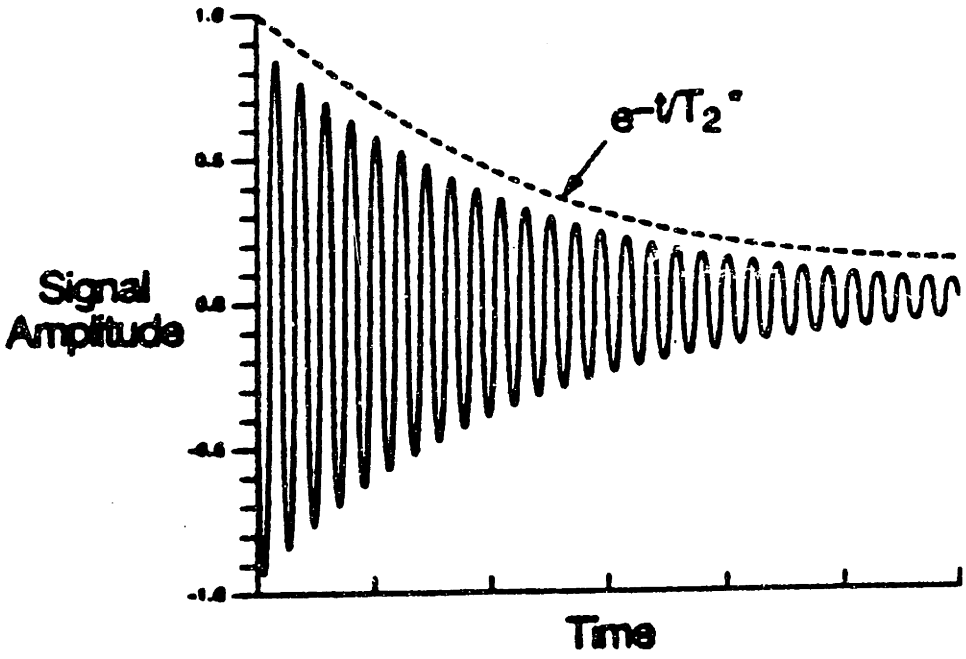

Figure 2.14 As the spins dephase, the signal in the RF coil decays away at T_2^*. This loss of signal after the 90° RF pulse is defined as free induction decay (FID). From Keller, 1988.

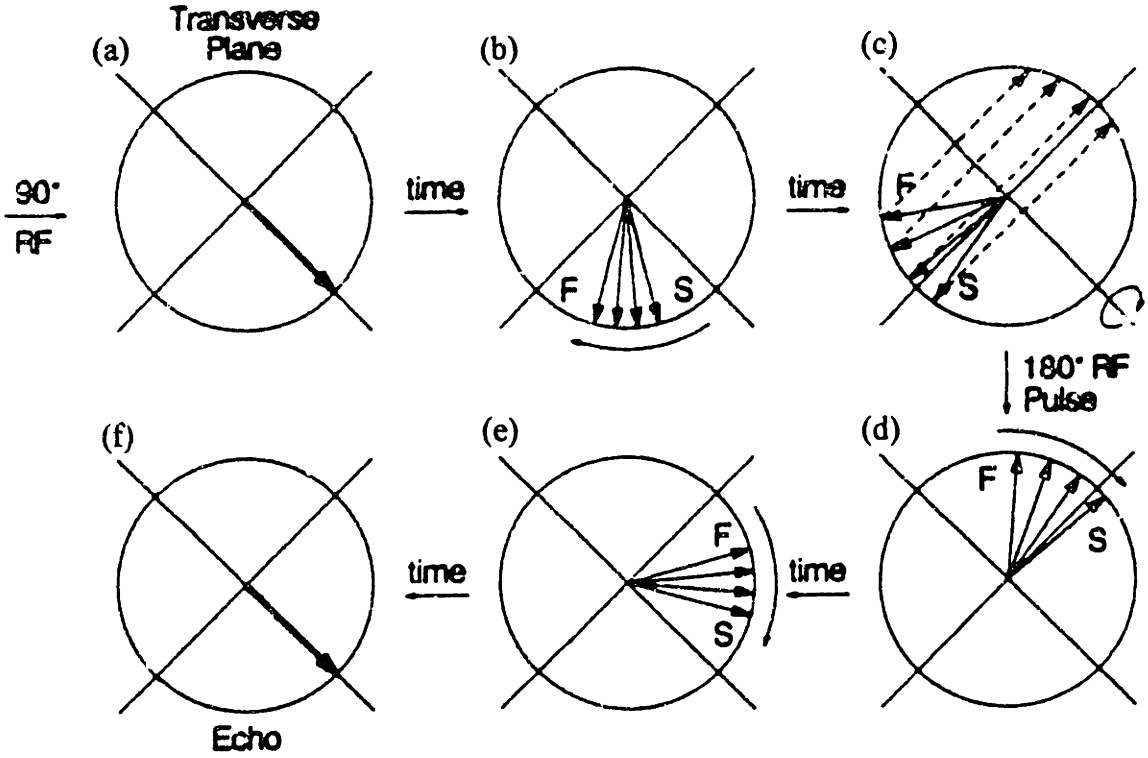

Figure 2.15 To impede dephasing of the spins and loss of signal through FID, CPMG pulse sequence is used. In (a), the net magnetization is tipped into the transverse plane by a 90° RF pulse and the spins are initially all in phase. As seen in (b), some spins will precess faster (F) and some slower (S) because of nonhomogeneity of $\mathbf{B_0}$. As seen in (c) and (d), after a 180° RF pulse, the spins are flipped 180° about the y axis, so that the slower spins move ahead of the faster spins. As time goes on, the faster spins begin to catch up to the slower spins (e); when all are once again in phase, a spin echo is created (f). From Keller, 1988.

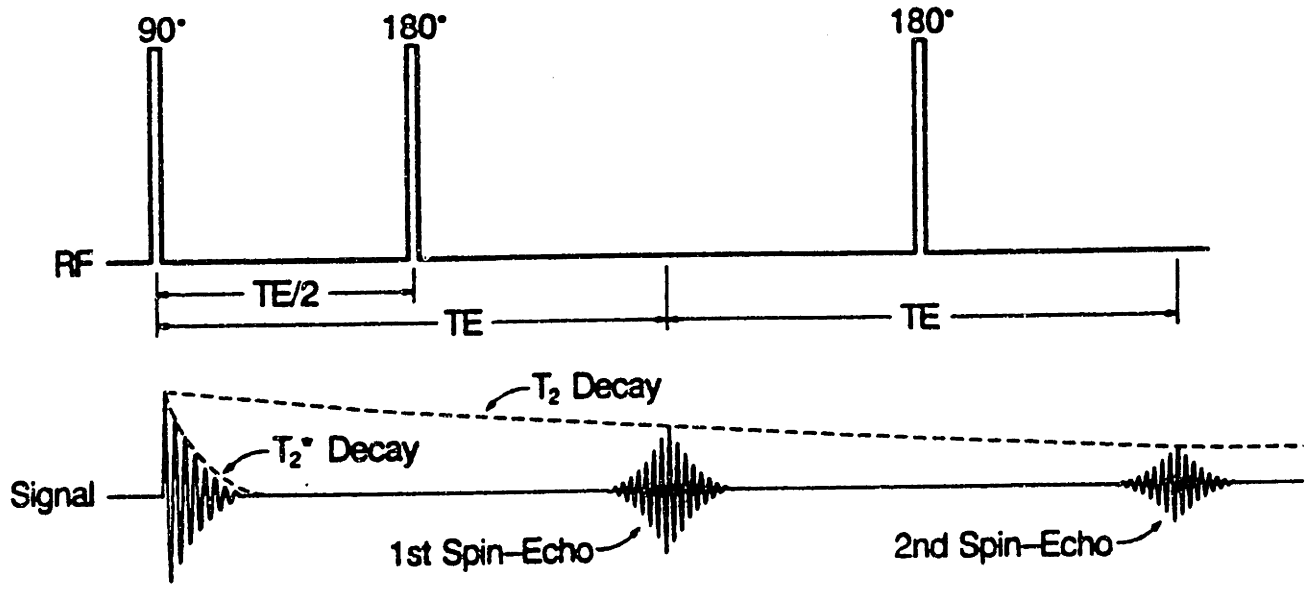

Figure 2.16 Top: The CPMG pulse sequence starts with a 90° RF pulse followed by a 180° RF pulse $T_E/2$ later in time. Successive 180° RF pulses are separated by T_E. Bottom: The spin echoes each have an FID. T_2 decay is seen as the envelope of the maximum amplitude of the echoes. From Keller, 1988.

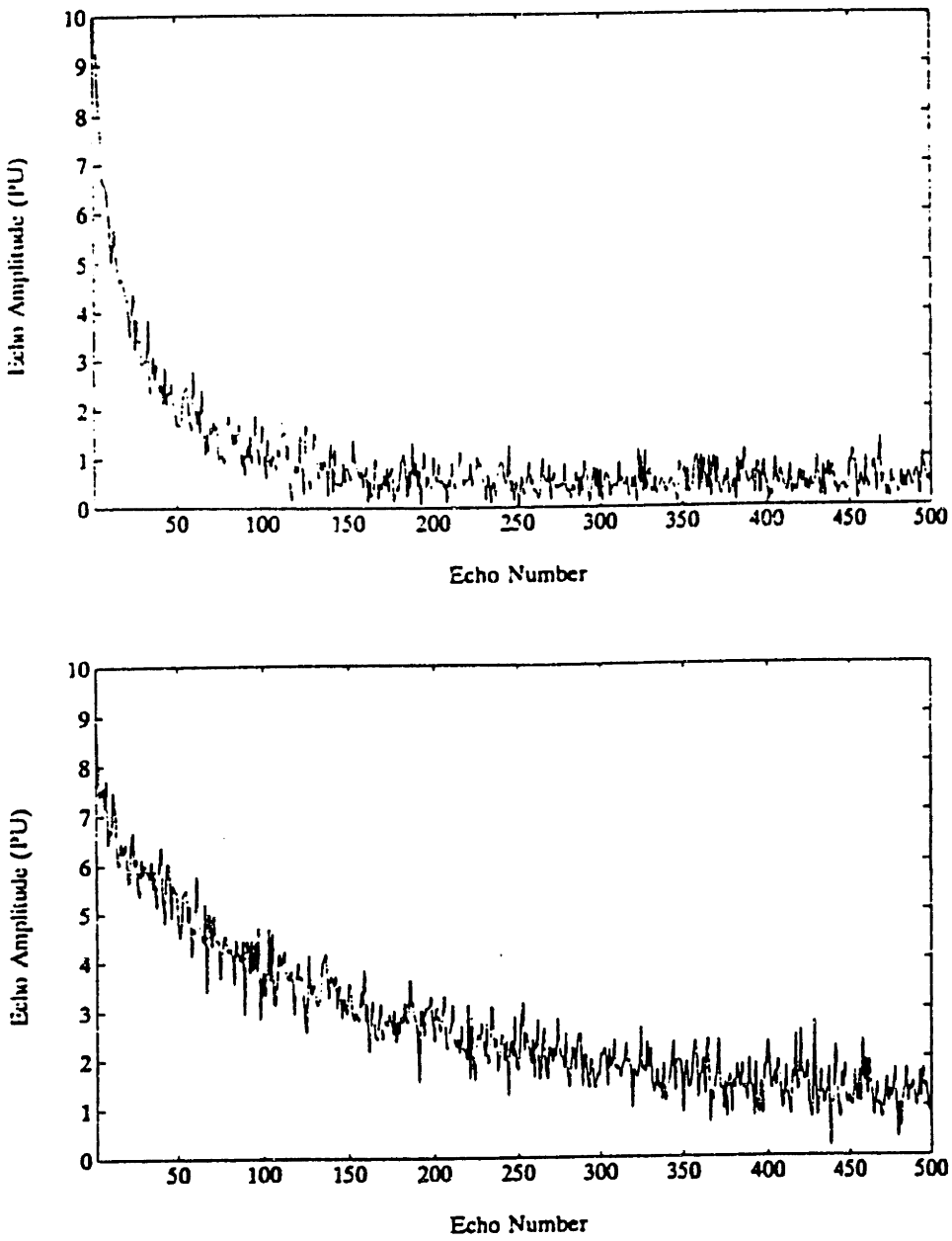

Figure 2.17 NMR echo trains from the Shell Test Well in Johnson City, Texas: Top example: echo train from logging data in a clean sand at 1084 feet; Bottom example: echo train from logging data in a shaley interval at 1147 feet. (N=500 echoes and T_E=1.2 ms.) From Chandler, et al., 1994.

Chapter 3
Nuclear Magnetic Resonance Log Measurements

This chapter discusses the well logging measurements that can be made with NMR. NMR is a robust way of measuring total effective porosity. Clay-bound porosity and microporosity are more difficult to measure with a logging tool because they both have very fast decay times. The T_2 decay of most clay-bound porosity is on the order of 2 ms. The down-hole technology to measure clay-bound porosity has not been developed, although it can be measured in the laboratory. At present, clay-bound porosity and microporosity must be derived as the difference between the total porosity measured with nuclear or sonic logs and the effective porosity measured with NMR logs.

3.1 Total Effective Porosity (MPHI)

NMR porosity (MPHI) is the total effective porosity as measured by the NMR logging tools. It represents all the porosity except for clay-bound porosity and microporosity. The NMR relaxation curve of Figure 3.1 shows that the total amplitude of the relaxation curve at $t = 0$ is equal to the effective porosity. Clay- or mineral-bound hydrogen is missed by the measurement because most of it has decayed by the time of the first pulse echo at 1.2 ms. In laboratory experiments, T_E is on the order of 0.2 ms, which will give five pulse echoes during the decay of the clay-bound water. In this case, the relaxation curve will have a larger value at $t = 0$. This value will represent total porosity.

Current NMR well logging technology does not have the signal-to-noise ratio or the very small echo spacing (T_E) of the laboratory and cannot measure total porosity. In the

near future, new tools using pulse sequences and electronics will be developed that will allow NMR measurements while logging that are at present only possible in the laboratory.

3.2 Bulk Volume Irreducible

Bulk volume irreducible (BVI) is the total amount of capillary-bound water. In other words, it is the water that resides in the smallest pores, the pores where the surface-to-volume ratio is such that the surface tension does not allow the water to move at all. In the case of sandstone, BVI is all pore space with diameters less than 20 microns. In terms of T_2, BVI for clastics is all the T_2 distribution of less than 33 ms decay time. In the case of carbonates, BVI is more complicated but generally is all the T_2 distribution of less than 100 ms decay time. Carbonates have a larger surface relaxivity (ρ) and, thus, their T_2 decay rate is more gradual. In the Figure 3.1, BVI is equal to MPHI-FFI.

3.3 Free Fluid Index

Free fluid index (FFI) is the total amount of porosity that lies in the larger pores. The pore space that makes up the free fluid has a small surface-to-volume ratio such that the surface tension allows most of the fluid to flow freely; a relatively small amount of water remains on the surface of the grains. For clastics, FFI resides in pores larger than 20 microns and less than 140 microns in diameter. The T_2 relaxation for FFI is that part of the distribution that is 33 ms or larger. The integral of the T_2 distribution from t = 33 ms to t = 1024 ms is equal to the FFI. In Figure 3.1, MPHI (total effective porosity) is the value of the T_2 relaxation curve extrapolated back to t = 0. FFI is the value of the relaxation curve extrapolated back from t = 33 ms. Therefore, the difference in these two porosities, MPHI–FFI, is the porosity that decays in the first 33 ms, which is the BVI.

The idealized NMR relaxation curve can be represented as made up of three major components: free fluid porosity, BVI, and clay-bound porosity plus microporosity. In Figure 3.1, free fluid porosity and BVI, as well as MPHI, are represented by three decay

curves. As noted above, free fluid decay is the decay of all the components at $t > 33$ ms. It is the decay of the protons in the largest pores and, thus, represents the portion of porosity in which fluids can freely flow. BVI is decay of components at less than 33 ms, that is, of protons in smaller pores. BVI represents capillary-bound water, which is not free to flow. Also as noted above, a curve representing clay-bound porosity and microporosity is not shown because decay occurs in the first 2 ms. This part of the NMR relaxation spectrum is not seen by logging tools because it precedes the first pulse echo.

3.4 MPERM Permeability

The NMR well logging estimation of permeability that is used in this thesis is MPERM, which is derived from other NMR values according to the Coates's equation (Timur, 1969):

$$\text{MPERM} = [(\text{MPHI}/10)^2 (\text{FFI}/\text{BVI})]^2 \tag{3.1}$$

where permeability is given in millidarcies (md) and MPHI, FFI, and BVI are given in porosity units (pu).

Another important equation for estimating permeability by NMR is the Kozeny–Carman equation (Kenyon et al., 1988), based on the logarithmic mean of the T_2 distribution:

$$k = 1.6 \cdot 10^{-8}\ \text{MPHI}^{4.3} (1.5 \cdot T_2, \text{log mean})^{2.} \tag{3.2}$$

Such permeability models are continually being updated as new NMR data are compiled.

Permeability values from Coates's equation compare well with permeability determined by conventional core and production tests. They are accurate in many cases to within a factor of 2 of known values; in contrast, conventional log and percussion core values are rarely accurate to within an order of magnitude in many circumstances. MPERM

is also reliable as a relative measure in comparing two zones in a given well.

3.5 T_2 Distribution (Pore Size)

The T_2 distribution is derived from the NMR relaxation curve. The time-domain (actual) data measured in an NMR experiment are represented by a number of points separated by time T_E, where the number of points is equal to the number of echoes (n) in the CPMG pulse sequence. The amplitude of each point, calibrated in porosity units, is plotted versus time (t) after the 90° RF pulse; therefore, the hundredth point would happen at t = 100 T_E (Figure 3.3).

The T_2 distribution is an inversion (see Appendix) of the time-domain data into the T_2 domain. The object of this inversion is to obtain a least-squares fit of the data into 8 or 10 bins, so that the total porosity is distributed among the bins. An example is provided by Figure 3.4: the distribution is plotted as the value of each bin in porosity units according to the time center of the bin. The bins are centered at 2^{n+1} ms (Table 3.1).

The inversion of the echoes into the bins is done using MAP processing (Figure 3.5). Each echo is a linear combination of x_i multiplied by the decay curve of each bin. In addition to the linear combination ($A_{ij}\ x_j$), a given amount of noise (ε_i) exists within each echo. The MAP processing can be written in matrix form:

$$y_i = A_{ij}\ x_j + \varepsilon_i\ ;\ A_{ij} = e^{(-t_i/T_{2j})} \qquad (3.3)$$

where y is a vector whose ith entry represents the amplitude of the ith echo where i goes from 1 to n (the number of echoes); A_{ij} is the matrix where t_i is the time of the echo and T_{2j} is the T_2 of the jth bin; and the vector ε_i represents the noise.

The T_2 distributions for many sandstones is bimodal (Figure 3.4). The first part of the distribution, which represents the BVI, is given by the first three bins, which are centered at

4, 8, and 16 ms. The second part of the distribution, which represents the free fluid, is made up of the fourth through eighth bin. Integrating the first mode of the T_2 distribution from t = 0 to t = 16, or wherever the first mode ends, provides the BVI (pu) of the sample. Integrating from the beginning to the end of the second mode provides the FFI (pu). Integration of the entire T_2 distribution yields MPHI.

The T_2 distribution is important because T_1 and T_2 in porous media can be related to the surface-to-volume ratio. Therefore, knowing the distribution of T_1 or T_2 can be related to pore size in rock. Water in a small pore relaxes 10 to 1,000 times faster than in bulk fluid, where T_1 is approximately 3.5 seconds. Three factors account in large measure for the fast relaxation on a pore surface: paramagnetic centers on the pore surface; restricted diffusion within the pores; and the large magnetic susceptibility contrast and the fluid–solid boundary. Surface relaxivity ρ is fairly constant for sandstones and for carbonates.

In the center of a pore, the protons relax slowly at the bulk relaxation rate. Diffusion, however, mixes the slow-relaxing protons in the volume of the pore with the fast-relaxing protons on the surface. As outlined in Figure 3.6, because of molecular self-diffusion, protons in the center migrate to near the surface, where they quickly relax. The relatively fast diffusion time in water means that most of the protons in the center will achieve this migration.

The fast-diffusion limit for water in porous media is valid where the pores are not so large that most of the protons in the center of the pore do not have time to diffuse to near the surface between echoes. For very small pores, it takes less time on average for a proton in the center to diffuse to the surface, whereas in larger pores, the diffusion takes longer. Thus, T_1 or T_2 can be related to the surface-to-volume (s/v) ratio of the pore. The approximate equation uses a scaling factor ρ_2, the surface relaxivity:

$$\frac{1}{T_2} = \rho_2 \frac{S}{V} \tag{3.4}$$

In porous media, the T_1/T_2 ratio is constant. Therefore, if we can relate T_1 to the pore size, we can relate T_2 as well. A more complete derivation of the above equation may be found in the literature (Cohen and Mendelson, 1992). At present, predicting pore size through use of a logging tool is possible only with NMR.

The time-domain data are inverted into a T_2 distribution; from Equation 3.3, once the T_2 distribution is known, the pore size distribution can be predicted. Eight exponential decay curves representing eight bins are shown in Figure 3.7. The fastest decay curve shown, $e^{-t/4}$, represents protons in the smallest pores. The slowest decay curve, $e^{-t/512}$, represents protons in the largest pores. Any slower decay, such as $e^{-t/1024}$ (the ninth bin), would represent water in vugs or hydrocarbons; Equation 3.3 would no longer hold, however, because the spins are no longer in the fast-diffusion limit.

An example of data and their inversion into the T_2 domain is given for a fine-grain response in Figure 3.8. The time-domain curve is seen to decay very abruptly. The curves shown give the partition of porosity. Note that bins 3, 6, and 8 are missing, and bins 2 and 4 each account for about 14 pu of the porosity. Small pores account for the predominance of the 36 pu of MPHI.

Figure 3.9 provides another example, a course-grain response. Here, the time-domain curves decay gradually, and bin 7, at 11 pu, makes the largest contribution to MPHI. Bins 8, 6, and 5 are each at about 5 pu or greater, and very little porosity is found in the first three bins. As in the example of a fine-grain response, the MPHI is 36 pu, but the FFI, BVI, and MPERM values between the examples are distinctive, in particular in the very high permeability for the coarse-grain response (4200 vs. 6.7 md).

In the two examples, of fine- and coarse-grain responses, MAP processing was used to invert from a single curve in the time domain to the eight bins, or decay curves, in the T_2 domain. Once the amount of porosity in each bin is known, total porosity, MPHI, has been partitioned into eight (or 10) separate parts representing the eight (or 10) pore sizes. The

inversion from time-domain data to T_2-domain data is more precise than just finding BVI and FFI in that there is a distribution of pore sizes rather than merely a total amount of capillary-bound water and free fluid.

Table 3.1 Bins vs. T_2

	Bin Number									
	1	2	3	4	5	6	7	8	9	10
$T_{2\,(ms)}$	4	8	16	32	64	128	256	512	1024	2048

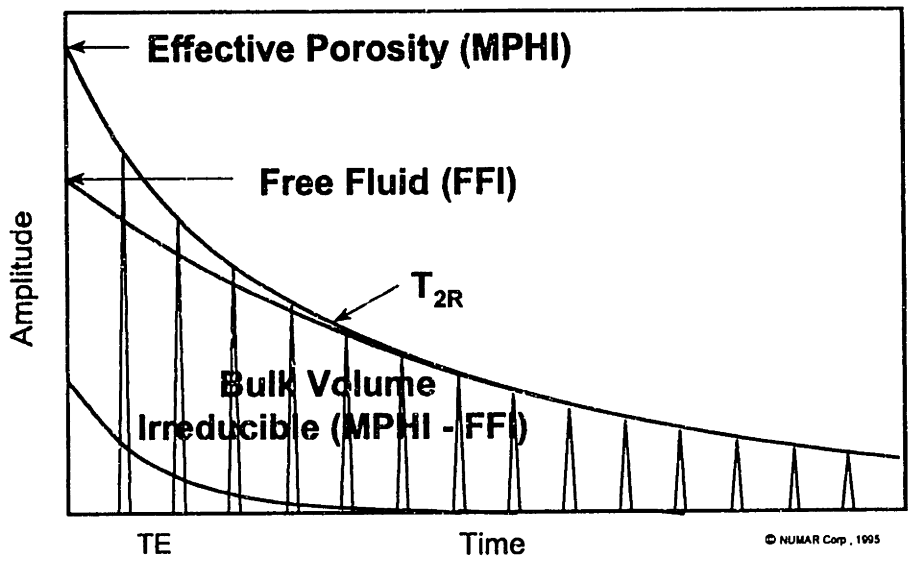

Figure 3.1 Idealized echo train showing that the t = 0 intercept of the best fit of the data from 33 ms and beyond is equal to the free fluid index (FFI). The t = 0 intercept of the best fit of the data for t = 0 to t = 32 ms is the effective porosity (MPHI). The capillary-bound water (BVI) is MPHI–FFI. From Cherry, 1995.

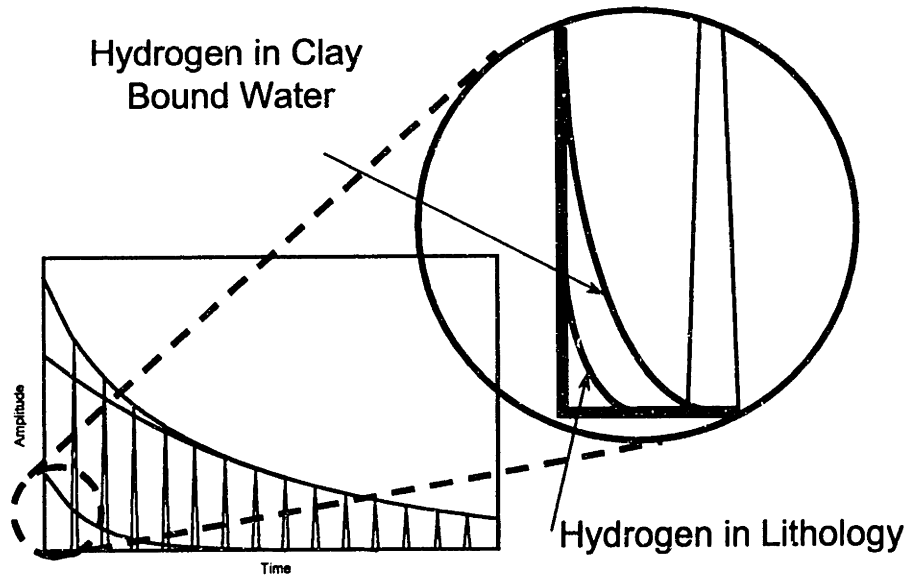

Figure 3.2 Clay-bound and mineral-bound hydrogen is missed by MPHI because most of it decays before the first echo. From Cherry, 1995.

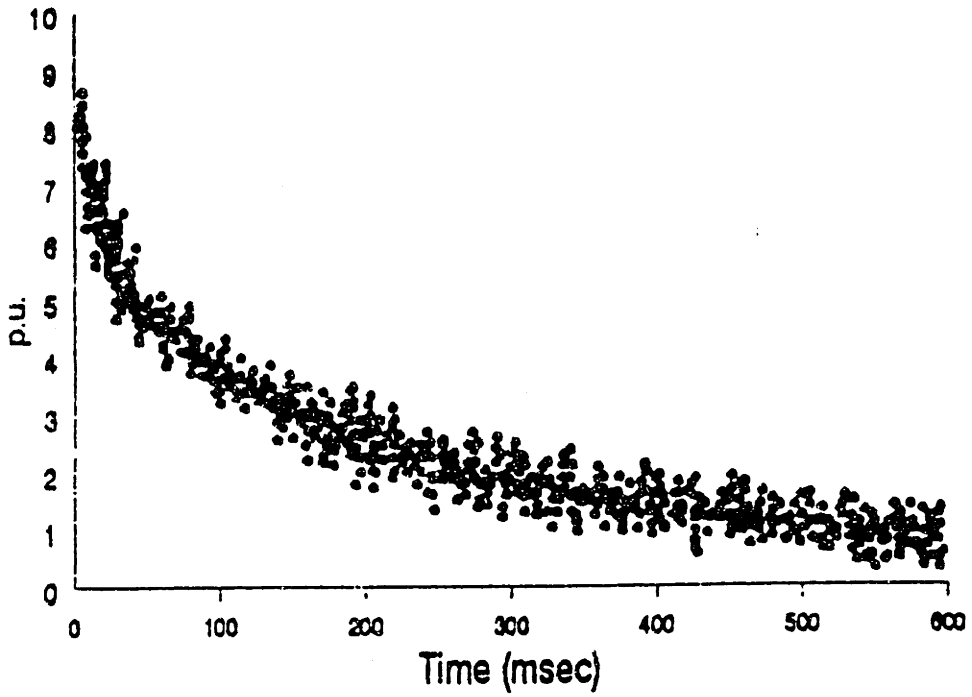

Figure 3.3 Time-domain data from an NMR logging experiment with 500 echoes. From Prammer, 1994.

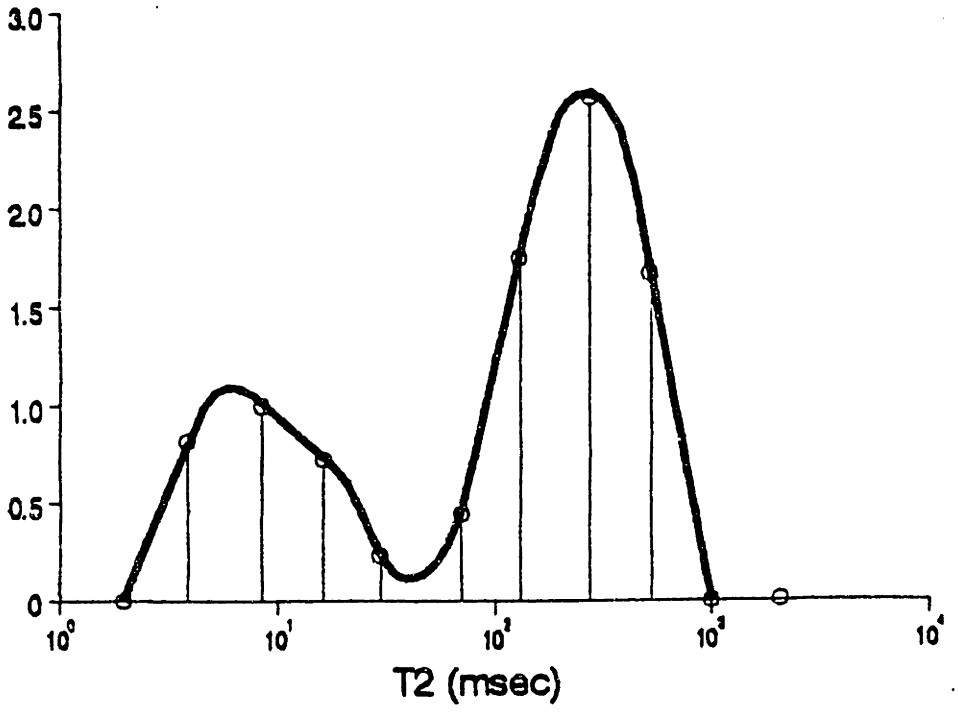

Figure 3.4 T_2 distribution from the time-domain data in Figure 3.3, showing the porosity plotted at each of the 10 bins. The integral of the T_2 distribution is equal to the t = 0 intercept of the time-domain data in Figure 3.3 (i.e., the total effective porosity, or MPHI). From Prammer, 1994.

$$\text{Echo 1} = x_1 e^{-t/4} + x_2 e^{-t/8} + x_3 e^{-t/16} + x_4 e^{-t/32} + x_5 e^{-t/64} + x_6 e^{-t/128} + x_7 e^{-t/256} + x_8 e^{-t/512} + \text{Noise}$$

$$\text{Echo 2} = x_1 e^{-2t/4} + x_2 e^{-2t/8} + x_3 e^{-2t/16} + x_4 e^{-2t/32} + x_5 e^{-2t/64} + x_6 e^{-2t/128} + x_7 e^{-2t/256} + x_8 e^{-2t/512} + \text{Noise}$$

$$\text{Echo 3} = x_1 e^{-3t/4} + x_2 e^{-3t/8} + x_3 e^{-3t/16} + x_4 e^{-3t/32} + x_5 e^{-3t/64} + x_6 e^{-3t/128} + x_7 e^{-3t/256} + x_8 e^{-3t/512} + \text{Noise}$$

$$\bullet$$

$$\bullet$$

$$\bullet$$

$$\text{Echo n} = x_1 e^{-nt/4} + x_2 e^{-nt/8} + x_3 e^{-nt/16} + x_4 e^{-nt/32} + x_5 e^{-nt/64} + x_6 e^{-nt/128} + x_7 e^{-nt/256} + x_8 e^{-nt/512} + \text{Noise}$$

Figure 3.5 MAP processing is an inversion scheme to expand the echoes into a linear combination of the eight decay curves plus the noise. The coefficients that can be solved for are x_i, which are the partial porosities of the eight bins. The fast decays ($e^{-t/4}$) represent the smallest pore sizes and the slow decays ($e^{-t/512}$) represent the largest pore sizes. Adapted from Cherry, 1995.

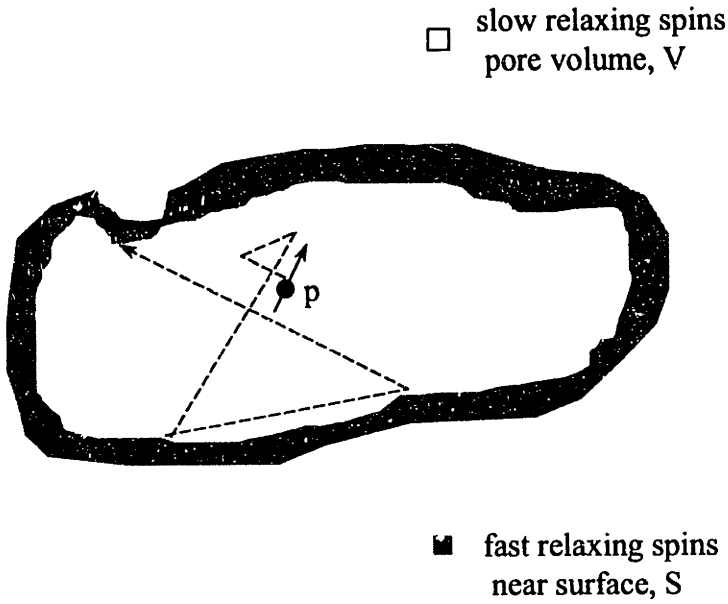

Figure 3.6 T_2 relaxation in a water-filled pore takes place when slow-relaxing-protons in the center of the pore diffuse to near the surface, where they quickly relax. In large pores, it takes the protons longer to diffuse to the surface, so that the total T_2 relaxation time is greater.

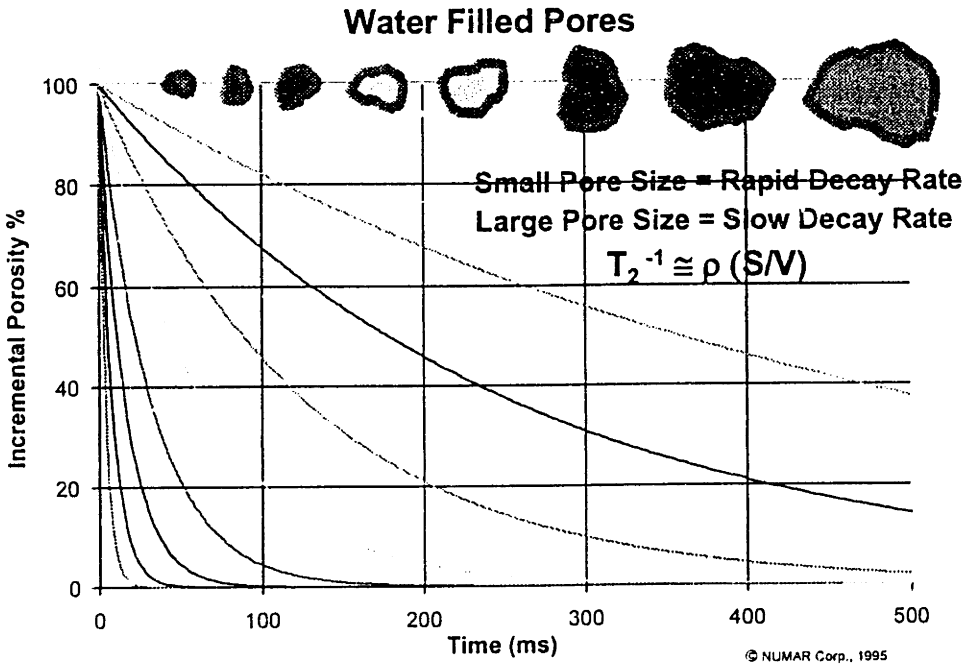

Figure 3.7 T_2 decay can be related to pore size. The protons in the largest pores (bin 8) decay slowly, at $e^{-t/512}$. The protons in the smallest pores (bin 1) decay rapidly at $e^{-t/4}$. From Cherry, 1995.

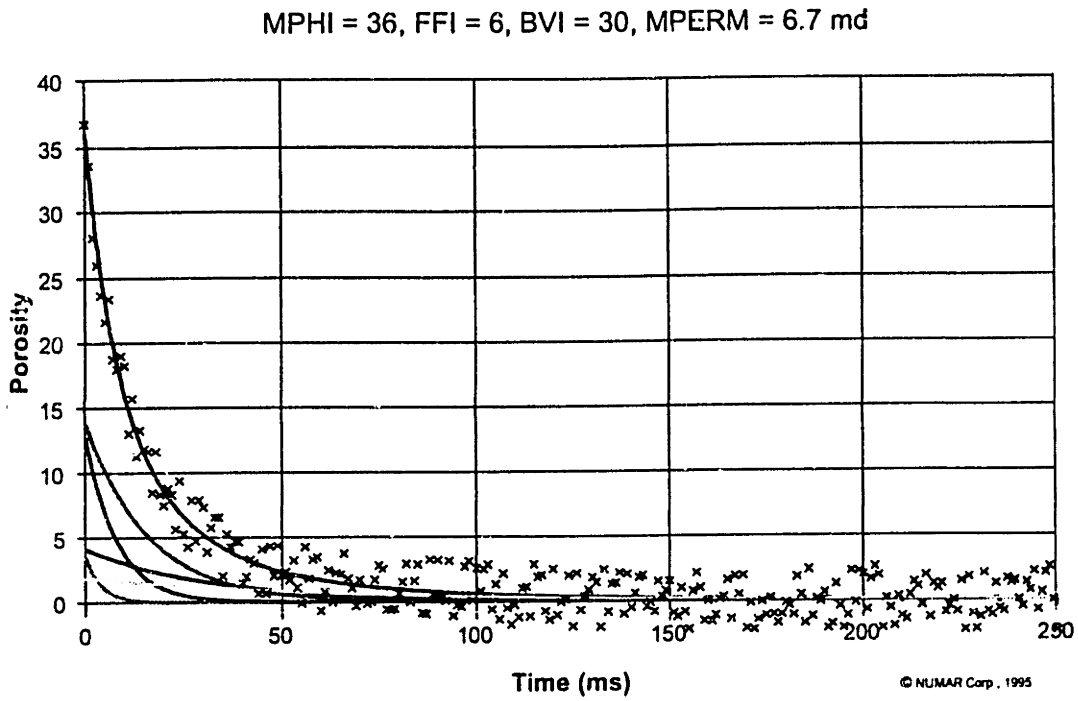

Figure 3.8 This fine-grain sand has high porosity (36 pu), high BVI (30 pu), and low permeability (6.7 md). The porosity is predominantly in the early bins (steepest decays). The sand has 13 pu in bin 2 and 14 pu in bin 4, and less than 5 pu in each of bins 1, 5, and 7. From Cherry, 1995.

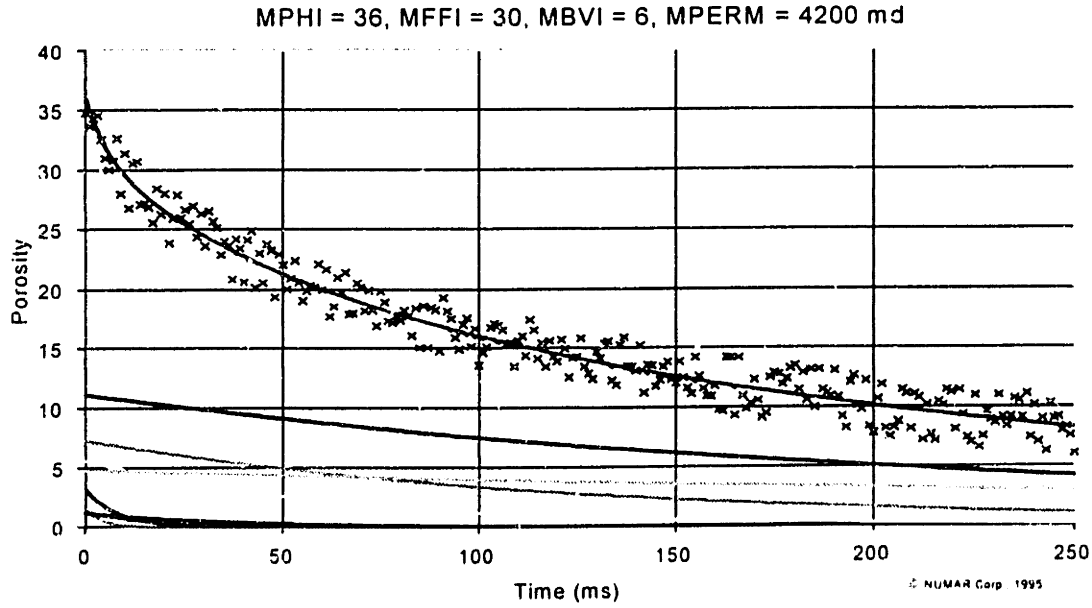

Figure 3.9 This coarse-grain sand has high porosity (36 pu), low BVI (6 pu), and very high permeability (4200 md). The porosity is predominantly in the late bins (slowest decays). The sand has 11 pu of bin 7 and [illegible] pu of bin 6, and about 5 pu in each of bins 5 and 8. The other bins are each below 4 pu. From Cherry, 1995.

Chapter 4

Nuclear Magnetic Resonance Logging Tools

Commercially available NMR logging tools have evolved tremendously since the development of the first tool, by Chevron, in 1965. That tool, the NML (Nuclear Magnetic Log), did not have the capability of slice selection because its magnet was the earth's magnetic field, a local constant. The modern commercial NMR logging tools, the NUMAR MRIL (Magnetic Resonance Imaging Log) and the Schlumberger CMR (Combinable Magnetic Resonance), both use CPMG pulse sequencing and do not require any doping of the drilling mud.

4.1 The Chevron Nuclear Magnetic Log (NML)

The first NMR logging tool, Chevron's NML (Nuclear Magnetic Log), was commercially available through the Schlumberger Corporation. As noted above, the NML uses the earth's magnetic field, a local constant equal to ½ gauss, as $\mathbf{B}_0$. The transverse magnetic field, $\mathbf{B}_1$, must have a frequency of approximately 2 kHz, which is the Larmor frequency, for a ½-gauss constant magnetic field. The tool uses a 90° RF pulse in the $\mathbf{B}_1$ direction, followed by free induction decay (FID) (Figure 4.1). Because of the 30-ms lag after the RF pulse, the FID can be used to measure only the free fluid index (FFI) of the sample. The maximum amplitude of the FID can be used to estimate free fluid porosity. The tool cannot measure BVI because the signal of the bound water entirely decays in the first 30 ms after the 90° RF pulse.

The NML does not measure the clay-bound or capillary-bound (BVI) water; these porosities must be measured with conventional logs. However, when no water is clay bound, BVI (one of the most important values from NMR logging) can be determined by subtracting FFI from total porosity determined by nuclear or sonic logs. The NML measures the relaxation of protons in fluid, so most of the signal comes from the fluid-filled borehole and not the formation. To "kill" the signal from the borehole when using the NML, it is necessary to add a paramagnetic salt to the drilling mud (i.e., to "dope" the mud).

While the NML was useful in measuring free fluid in some very silty, low-permeability reservoirs, it could not attain the resolution of modern tools. Because the NML did not use the CPMG pulse sequence and had to rely on a single FID, measurement was much less accurate. As discussed in Chapter 2, FID alone measures T_2^* and not T_2; therefore, the NML was unable to examine pore size and some of the other rock properties that can be derived from the intrinsic T_2. The T_2^* value extrapolated back to $t = 0$ is a fairly reliable measure of free fluid porosity.

As noted above, the tool did not have the ability of slice selection. Therefore, the signal measured at the RF coil was a combination of all the decaying protons in the surrounding fluid. The doping of the drilling mud to kill that part of the signal made the NML a much more complex procedure operationally. Because the NML uses the magnetic field of the earth, which is not globally constant, the calibration of the tool is geography dependent. Although the NML was not as accurate as modern NMR logging tools, it represented the first logging response in which free fluid and bound water, as well as permeability, could be inferred from a down-hole measurement.

4.2 The NUMAR Magnetic Resonance Imaging Log

One of the modern pulsed NMR logging tools is the MRIL (Magnetic Resonance Imaging Log) of the NUMAR Corporation of Malvern, Pennsylvania. The MRIL (Chandler et al., 1994) uses much of the technology from medical imaging. It not only uses the CPMG

pulse sequence to measure the intrinsic T_2 of the fluids, but also has a gradient magnetic field, which allows slice selection where the sensitive volume is chosen depending on the frequency of the RF pulses.

The MRIL (Figure 4.2) has been in commercial operation since 1991. It has undergone many enhancements in both electronics and software since its inception. Much of the research in the present thesis is derived from using the versatility of the MRIL technology to develop a novel approach to formation evaluation and direct hydrocarbon imaging. Many of the techniques used are combined from NMR core analysis and logging applications, as well as medical imaging.

The gradient magnetic field gives the possibility of making many measurements that provide a wider range of applicability for the tool. As seen in Figure 4.3, the magnetic field falls off as 1/r 2. The field strength is 200 gauss at $r \cong 8$ inches and there is a 25-gauss/cm uniform-gradient magnetic field. The Larmor frequency is equal to a constant γ, the gyromagnetic ratio for protons multiplied by the magnetic field strength B_0. Therefore, as the frequency of the RF pulse is changed, the depth of investigation is changed. Since the magnetic field is radially symmetric, the sensitive volume will be an annular slice of 1-mm thickness, owing to the bandwidth of the RF pulse, and 2-ft height, owing to the aperture of the RF antenna. The depth of investigation as a function of frequency and temperature is schematized in Figure 4.4. The graph demonstrates that at a lower frequency, imaging is deeper. Very deep imaging is limited by the weakening of the NMR signal measured at the RF antenna, with rapid degradation of the signal-to-noise ratio.

One very important advantage of slice selection in well logging is that borehole rugosity and washouts do not affect the NMR signal. The sensitive volume is at approximately 8 inches from the center of the tool (Figure 4.5). Therefore, as long as the borehole is less than 16 inches in diameter, the NMR signal is unaffected. Any fluid in the borehole or in the formation that is not in the sensitive volume will make no contribution to the signal because it is not the Larmor frequency.

Because of restrictive diffusion in a gradient magnetic field, the MRIL can be used to measure the diffusion constant of the fluid as well as the intrinsic T_2. The general equation for T_2 is

$$\frac{1}{T_{2meas}} = \frac{1}{T_{2int}} + \frac{1}{T_{2D}} \tag{4.1}$$

Two decay curves taken at T_E = 1.2 ms and T_E = 3.6 ms are shown in Figure 4.6. The curve with the greater T_E decays much faster, a result of restrictive diffusion. In the above equation, the second term can be written:

$$\frac{1}{T_{2D}} = \frac{(\gamma G T_E)^2 D}{12} \tag{4.2}$$

where T_E is the echo spacing in ms, G is the magnetic field gradient, γ is the gyromagnetic ratio, and D is the diffusion constant. T_{2D} is a function of the echo spacing and the magnetic field gradient. The MRIL has a fixed-field gradient, but T_E can be varied. Now, all the quantities in Equations 4.1 and 4.2 are known except for D and intrinsic T_2. With two decay curves, there are two equations: in the example of Figure 4.6, one in which T_E = 1.2 ms and one in which T_E = 3.6 ms. Thus, it is possible to solve for the two unknowns. This approach can lead to a measurement of the diffusion constant of the fluid in porous media that is independent of both lithology and mineralogy. The application of diffusion in a gradient magnetic field is extended in Chapter 6 to direct hydrocarbon imaging.

A major hindrance in NMR logging is the long T_W (wait time) between experiments. To obtain a signal-to-noise ratio that approaches ratios achievable in the laboratory requires a minimum of three to five experiments per foot. Wait times in excess of 2 s require logging speeds of between 1 and 3 ft/min.

The gradient field of the MRIL tool enables the use of "frequency hopping" to make multiple measurements by pulsing the RF antenna at different frequencies. Figure 4.7 shows the dual mode with two adjacent slices that represent two annular sensitive volumes

separated by 3 mm. This allows the logging to proceed twice as fast as with a single frequency. If a wait time of 2 s is needed, the first frequency is pulsed, which excites the protons in the first sensitive volume. Instead of a 2-s wait, the second volume is pulsed 1 s later, and then back to the first frequency after another full second so that the full wait time is achieved. With the two- or three-frequency mode, much higher logging speeds are achievable through hopping from one frequency—and, thus, one sensitive volume—to another. The necessary wait times at each slice are achieved, yet there are enough experiments to maintain adequate signal to noise and logging speeds in the range of 10 to 15 ft/min.

The MRIL utilizes many techniques of clinical MRI, such as frequency hopping to measure multiple slices. It also employs the gradient magnetic field, not only for slice selection but also to measure diffusion of fluids without the injection of dyes. Medical imaging has a wide range of applications, and is under intensive development. Many of its new techniques may be extended to logging with the MRIL. The gradient field could be applied in future tool configuration to run at multiple depths of investigation; for example, there could be a shallow measurement in the flush zone that is filled mostly with filtrate water. The flush zone measurement gives a better value for MPHI, the effective porosity, and is less affected by hydrocarbons. The deeper measurement can be used for direct hydrocarbon detection as well as provide a check on the shallow measurement in rugose or washed-out borehole conditions.

The physical design (Chandler et al., 1994) of the MRIL-C toolstring is shown in Figure 4.8. The total length of the toolstring is 49 ft.; the weight is 1121 lb. The tool is a mandrel borehole–centered device. There are three centralizers: one above and one below the 8-ft sonde, and one on the energy cartridge. There is a 165-inch energy cartridge and 165-inch electronics cartridge which are 3 5/8" in diameter. In the applications with a salt based mud a second energy cartridge can be attached to provide an extra 500 joules of energy to the RF Antennae.

The sonde is available in two diameters: a standard 6 inches (designed for 7.875- to 12.25-inch boreholes) and 4.5 inches (for 6.5- to 8.5-inch boreholes). The sonde's permanent magnet, $\mathbf{B}_0$, is a dipole with a 17-gauss/cm gradient. Inside the sonde, there is an RF antenna that supplies $\mathbf{B}_1$ (the transverse magnetic field), with an aperture of 24 inches. The magnetic field and RF antenna are designed to give a sensitive volume that is cylindrically symmetric and 24 inches tall and approximately 1 mm thick. Running in a frequency band of 700 kHz ± 50 kHz gives a slice between 14 and 17 inches in diameter.

The MRIL-C is rated up to 350°F and can be run in a saline environment with R_{MF} as low as 0.015 ohm-m. The standard T_E is 1.2 ms, but T_E is adjustable and running can be at longer times, such as 2.4, 3.6, or 6 ms, for specialized applications. The newest series (C_{TP}) of the tool has a T_E of 0.6 ms, used for new pulse sequences to measure clay-bound porosity and microporosity. In standard mode in fresh mud when longer wait times are used, as many as 1000 echoes can be taken in a single measurement. In a salty environment, echoes are limited to the 100 to 250 range. In a salty borehole, the load on the antenna can be substantially reduced by using a cylindrical plastic fluid excluder that fits over the sonde (excluder diameter of 7 ¼ inches). Although the tool is now larger in diameter, the sonde can easily be pulled out of the fluid excluder if the tool becomes differentially stuck and fishing is necessary.

The MRIL-C is a digital tool and is through-wired, therefore, it can be combined with the Western Atlas, Schlumberger, or Halliburton toolstring. The tool has much of the versatility of a laboratory NMR device, and the parameters of the pulse sequence can be adjusted according to the specific application. For short wait times and T_R, the tool can log as fast as 30 ft/min. The signal-to-noise ratio of an echo train is as great as 240:1 for FFI; the ratio is optimized as long as the tool is run in a range of 2.5 to 5 experiments per foot.

4.3 The Schlumberger Combined Magnetic Resonance

The other commercially available modern pulsed NMR logging tool is the Schlumberger CMR (Combinable Magnetic Resonance) log. The CMR is a constant magnetic field tool that uses CPMG in a pad-type configuration. The CMR has a side-focused constant magnetic field that examines a cigar-shaped volume in the flushed zone. Its depth of investigation is between 1 and 2 inches into the formation.

Because of the pad type configuration of the CMR, like the neutron and density, it carries certain benefits and drawbacks. In a rugose or washed-out borehole, the pad sometimes does not make good contact with the borehole wall, leading to erroneous measurements representing the drilling mud or mud cake rather than the formation. The key advantage of a flushed zone tool is that it is much less affected by gas than is the case with deeper measurements. The tool gives good measures of effective porosity and bound water porosity (BVI) that can be compared with the total porosity measured by neutron and density approaches at a similar depth of investigation.

Because the CMR is a pad-type tool, at normal logging speeds it has a 6-inch resolution. The tool is not limited by high-salinity drilling mud because the pad is in contact with the borehole wall and the RF antenna does not have to pulse through the conductive drilling fluid.

The CMR has a constant magnetic field in the sensitive volume; therefore, the frequency must be swept through to match the Larmor frequency in the focused volume. Because this is not a gradient field, the tool cannot use slice selection to choose the depth of investigation. The logging speed is also limited, since in a constant magnetic field frequency hopping cannot be used to increase it.

All the basic measurements of NMR logging (BVI, FFI, pore size, and T_2 distribution) can be attained with high resolution using CMR. Because the CMR is not a gradient-field NMR device, the diffusion measurements T_{2D} are not obtained. Some

techniques, such as those necessary for oil or gas detection and those used in clinical MRI, cannot be easily applied in a nongradient magnetic field.

Physical specifications of the tool are shown in Figure 4.9. The view of the magnetic field from above, including the configuration of the magnets, is shown in Figure 4.10. The sensitive volume is shown in the figure as shaded in very light gray to the right of the antenna. The decentralizer is part of the tool that pushes the pad into the wall on the opposite side of the borehole. As mentioned above, the tool is designed so that it can be combined with conventional logging tools, to allow all the logging data (both conventional and NMR) to be acquired in a single pass.

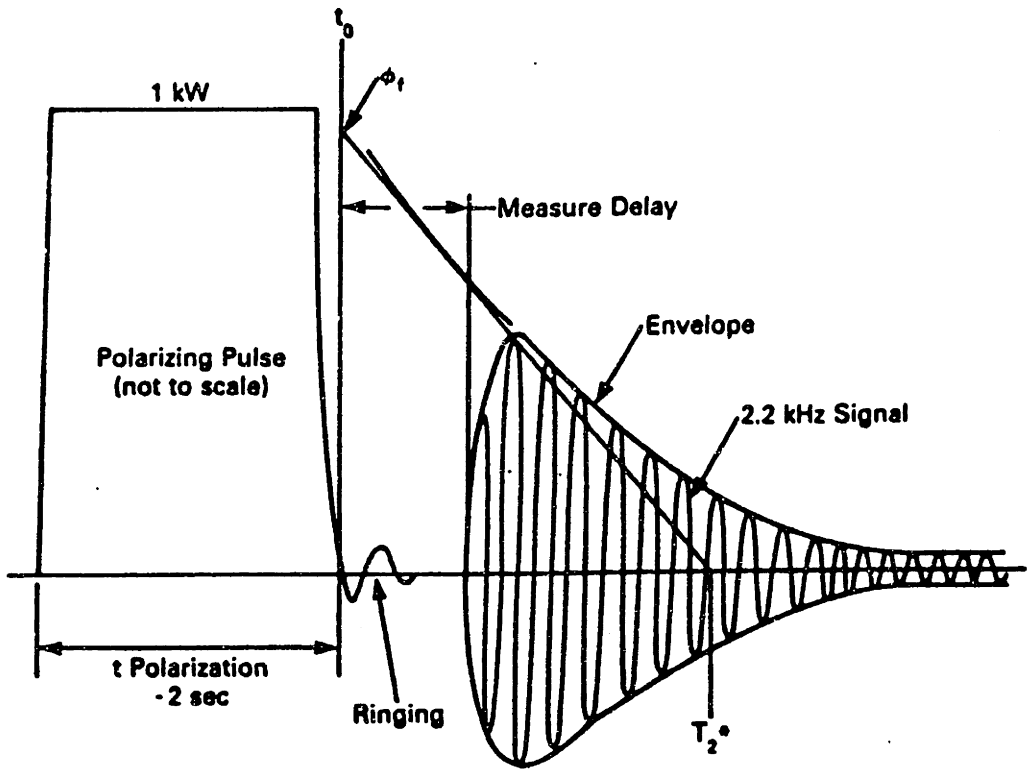

Figure 4.1 The NML pulse sequence begins with a polarizing pulse, which is followed by free induction decay (FID). The t = 0 intercept of the curve that fits the envelope of the FID represents the free fluid (FFI). From Ellis, 1987.

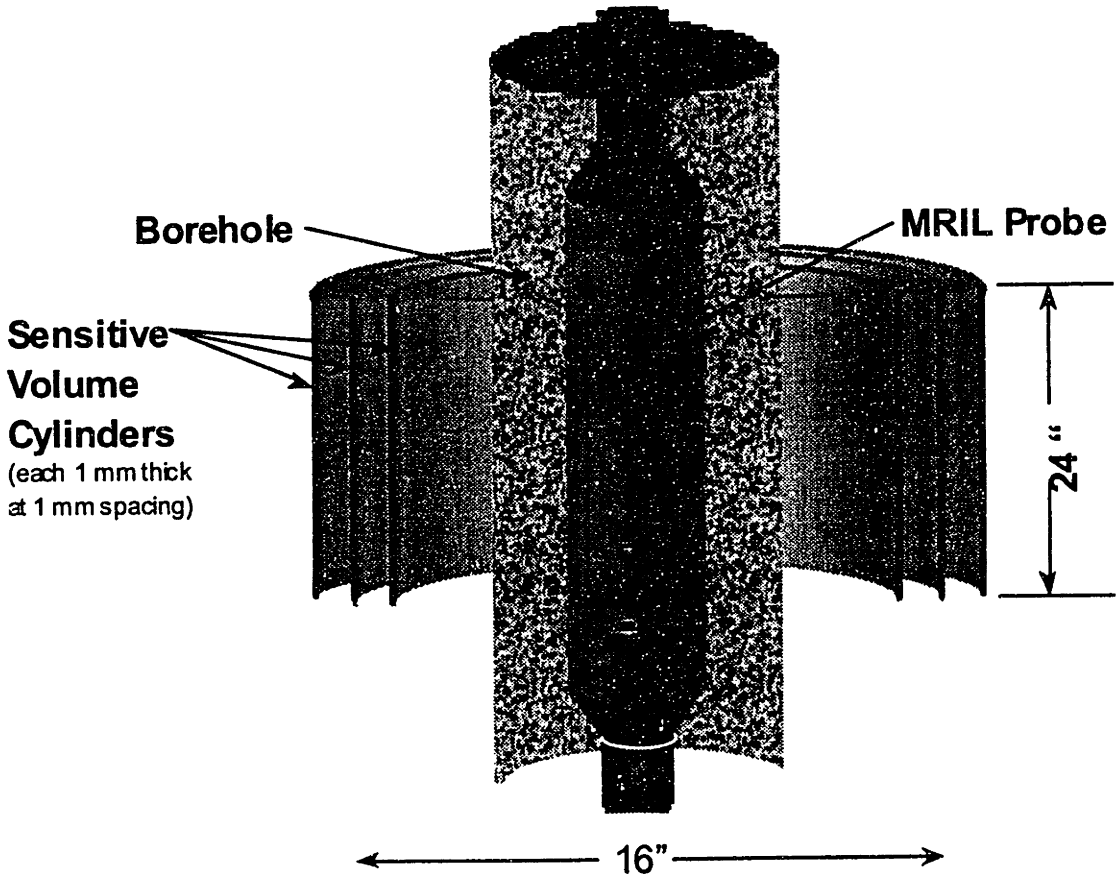

Figure 4.2 MRIL-C in the wellbore, running in triple-frequency mode, showing three diameters of investigation. From Cherry, 1995.

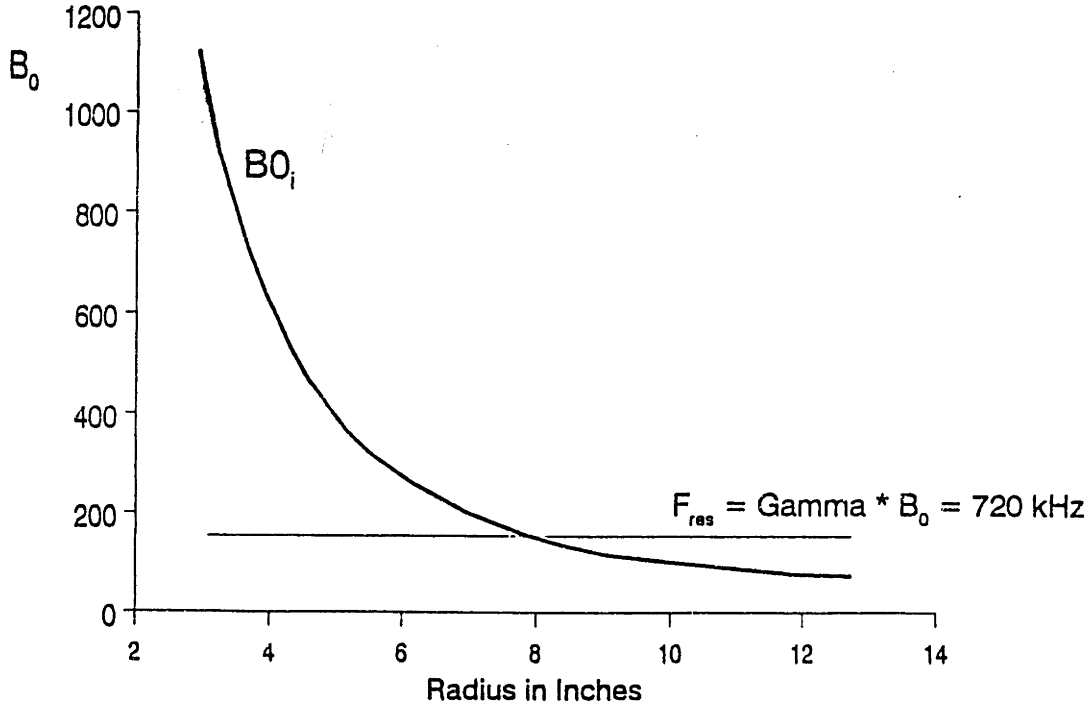

Figure 4.3 The magnetic field B_0, as a function of depth, falls off as a dipole and, at a Larmor frequency of 720 kHz, corresponds to a radius of investigation of 8 inches. From Chandler, 1995.

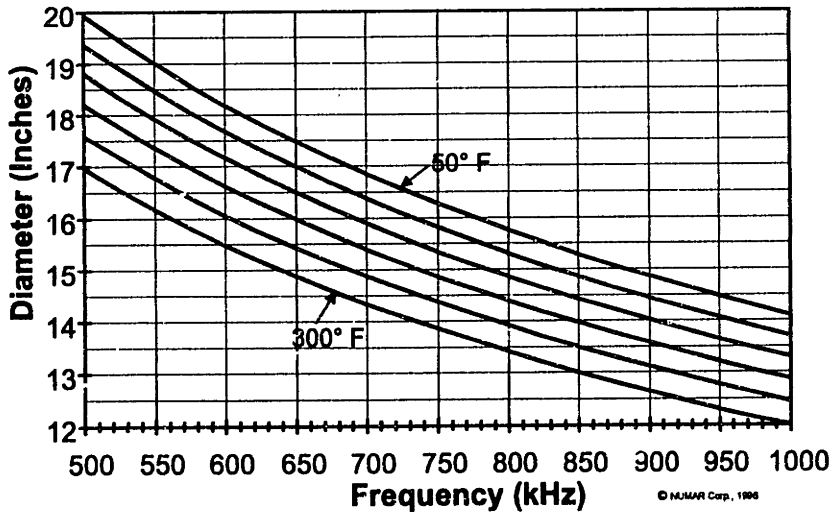

Figure 4.4 Diameter of investigation of the MRIL-C as a function of temperature and frequency. From Cherry, 1995.

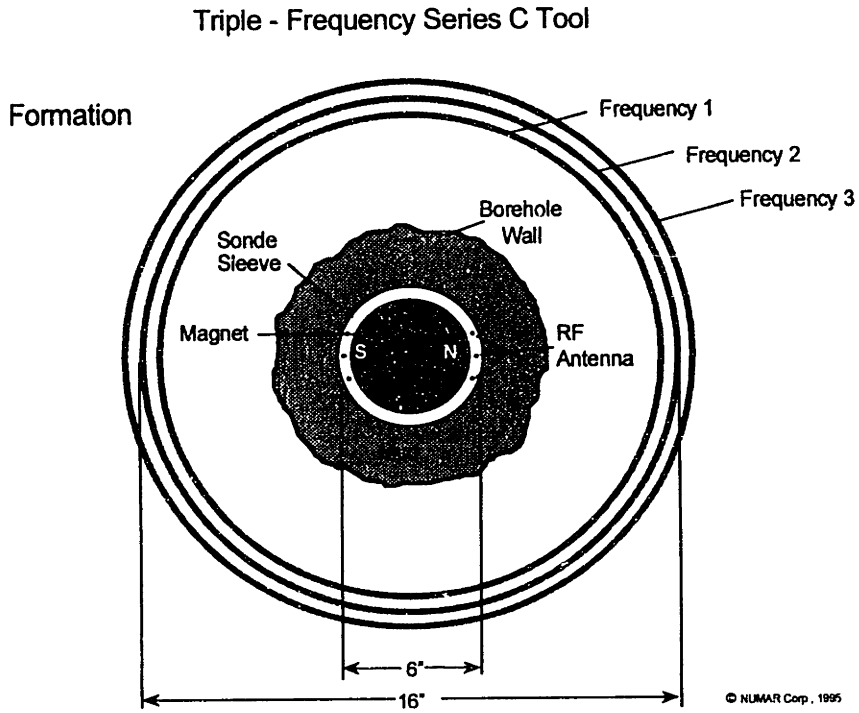

Figure 4.5 The MRIL-C, running at triple frequency, has a diameter of investigation of 16 inches. As long as the borehole does not wash out to this diameter, the measurement is unaffected. Therefore, the NMR measurement is insensitive to washouts or borehole rugosity. From Cherry, 1995.

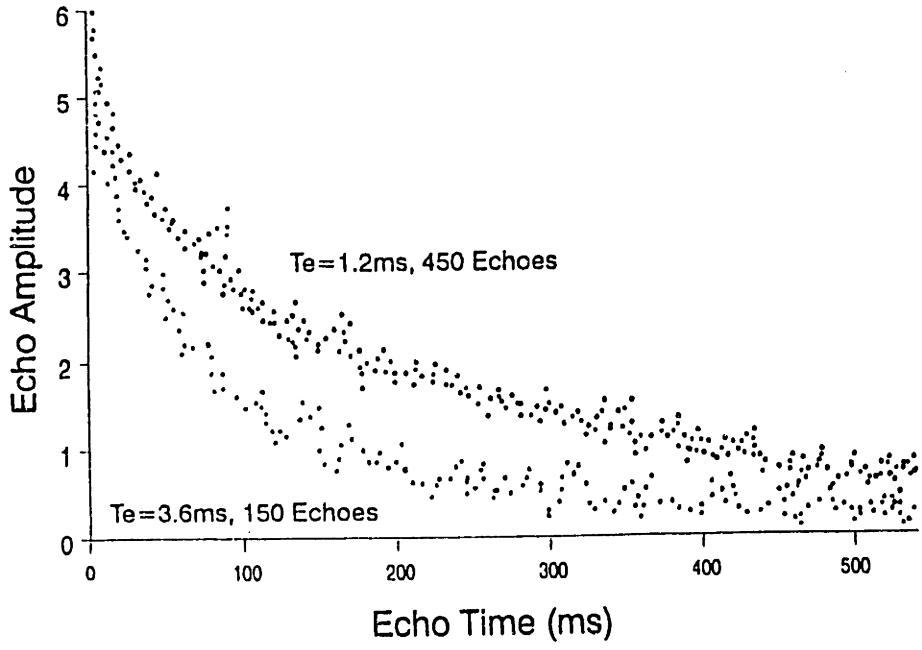

Figure 4.6 Two NMR experiments, at T_E = 1.2 ms and T_E = 3.6 ms, show the effects of diffusion. Because there are two experiments for the same zone, two parameters, T_2 and D_0, can be solved for in the sample. From Chandler, 1995.

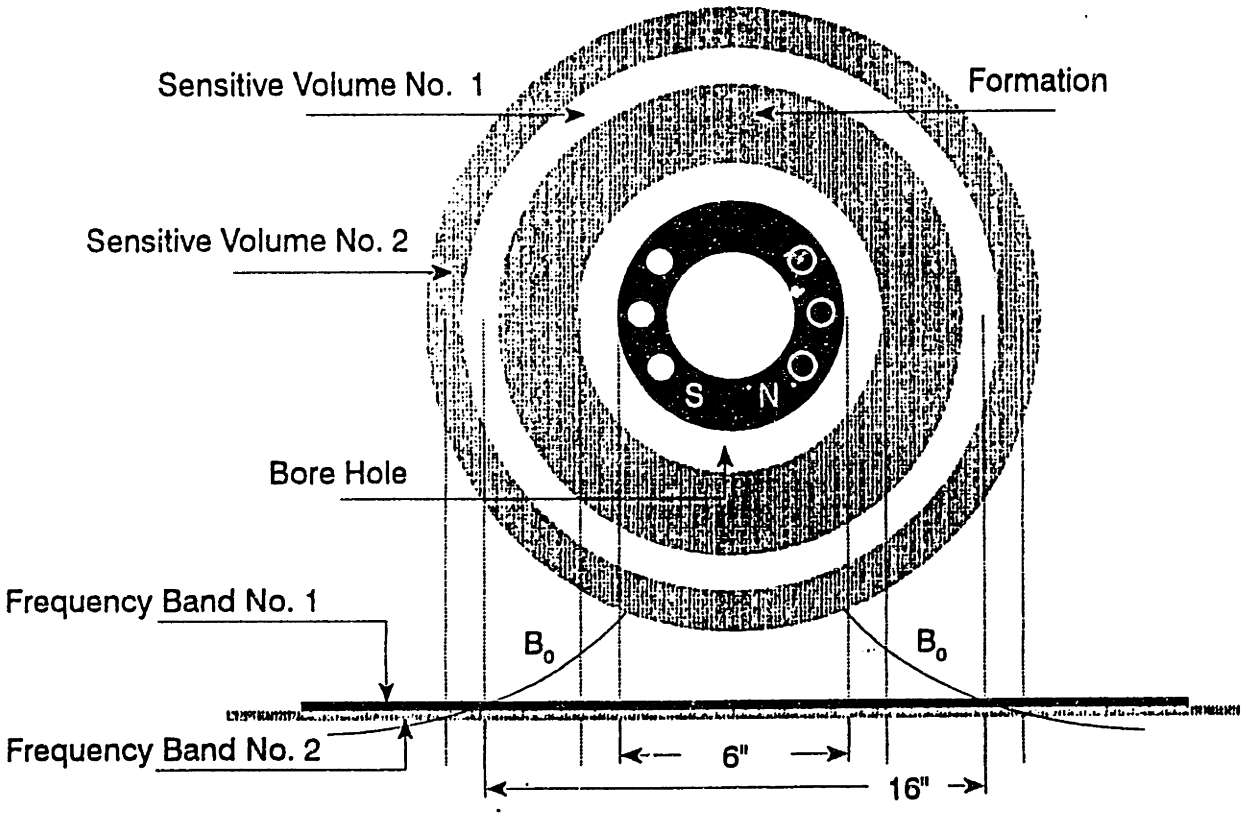

Figure 4.7 The MRIL-C running in dual-frequency mode with the two cylindrical sensitive volumes centered at 16 inches in diameter and separated by 3 mm. From Chandler, 1995.

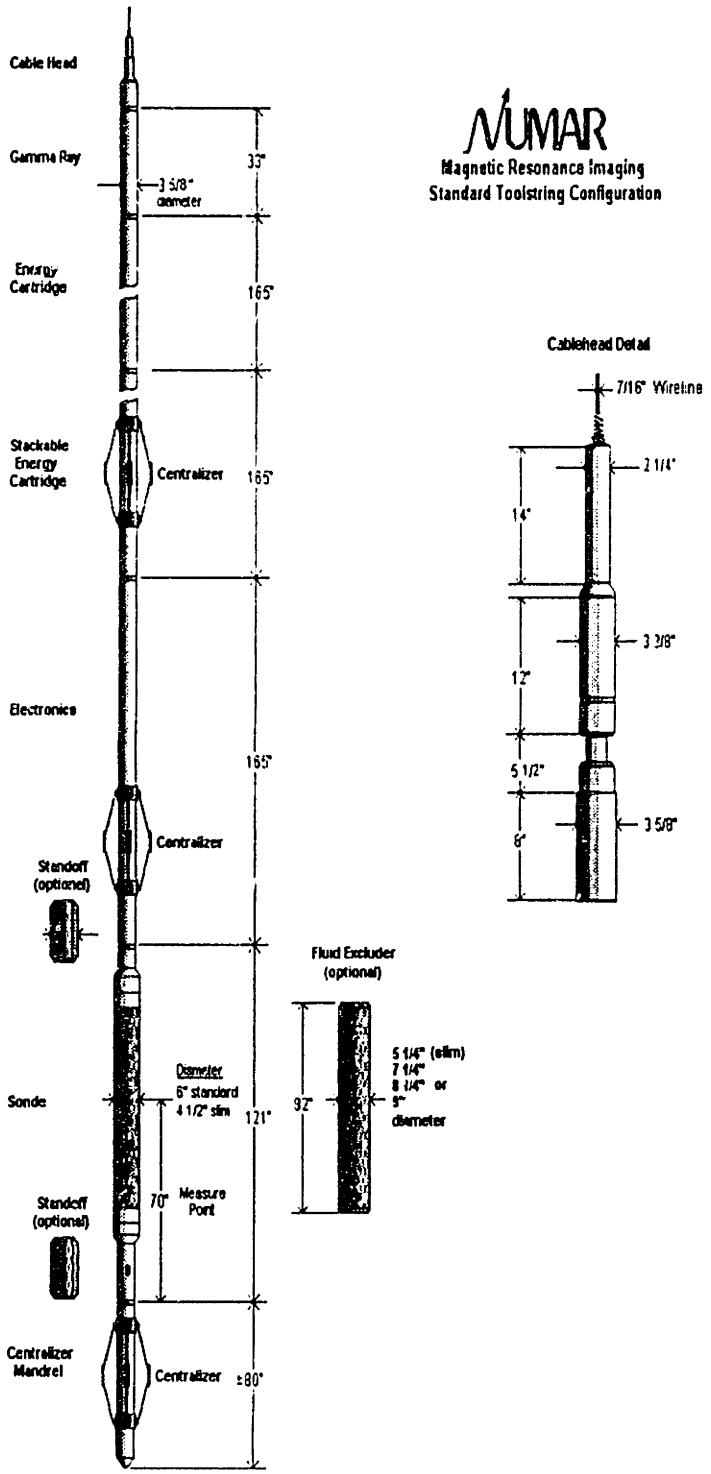

Figure 4.8 The MRIL-C toolstring configuration. Courtesy of Jay Baker, NUMAR Corporation.

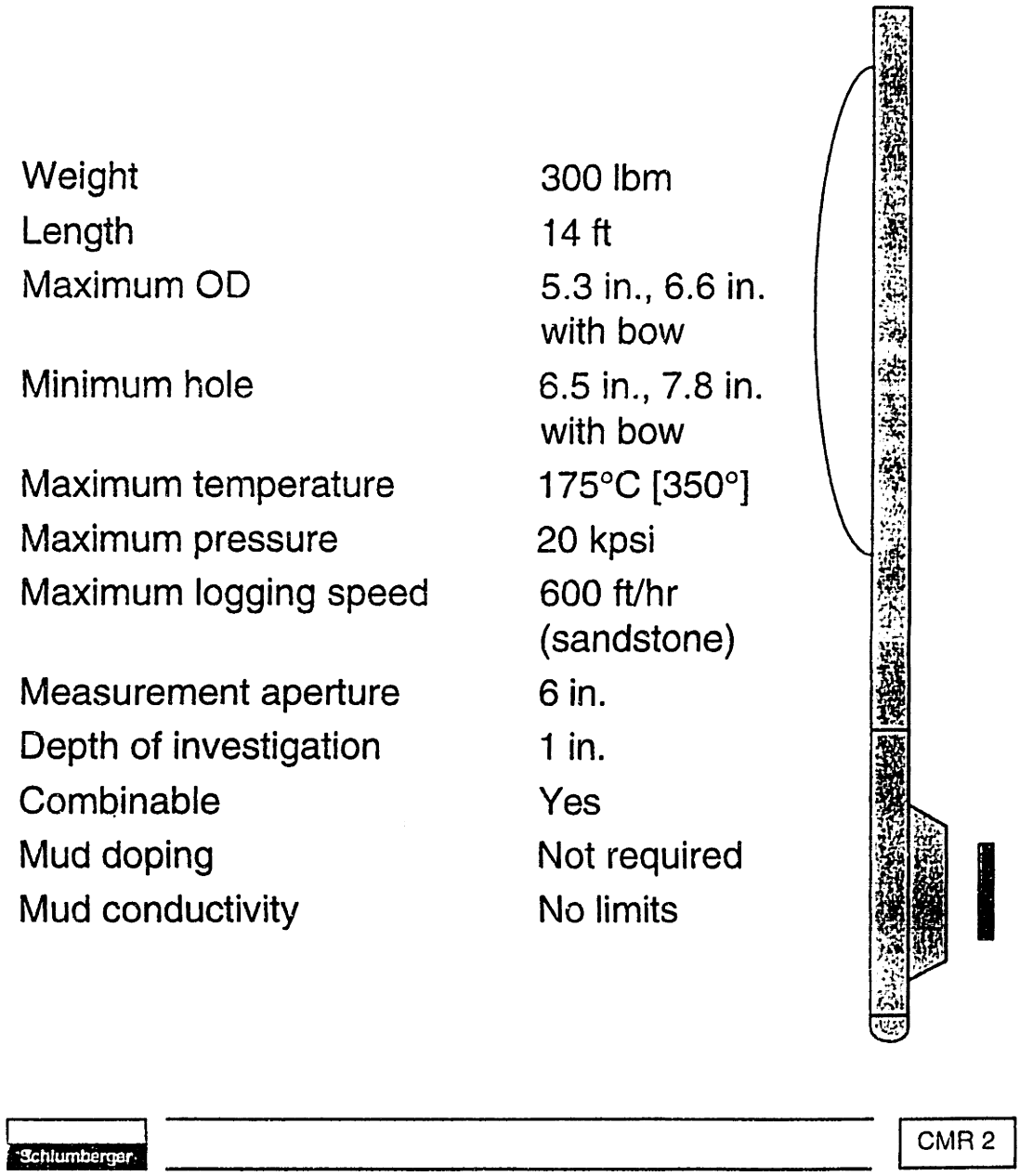

Figure 4.9 The CMR tool description. From Morriss, 1995.

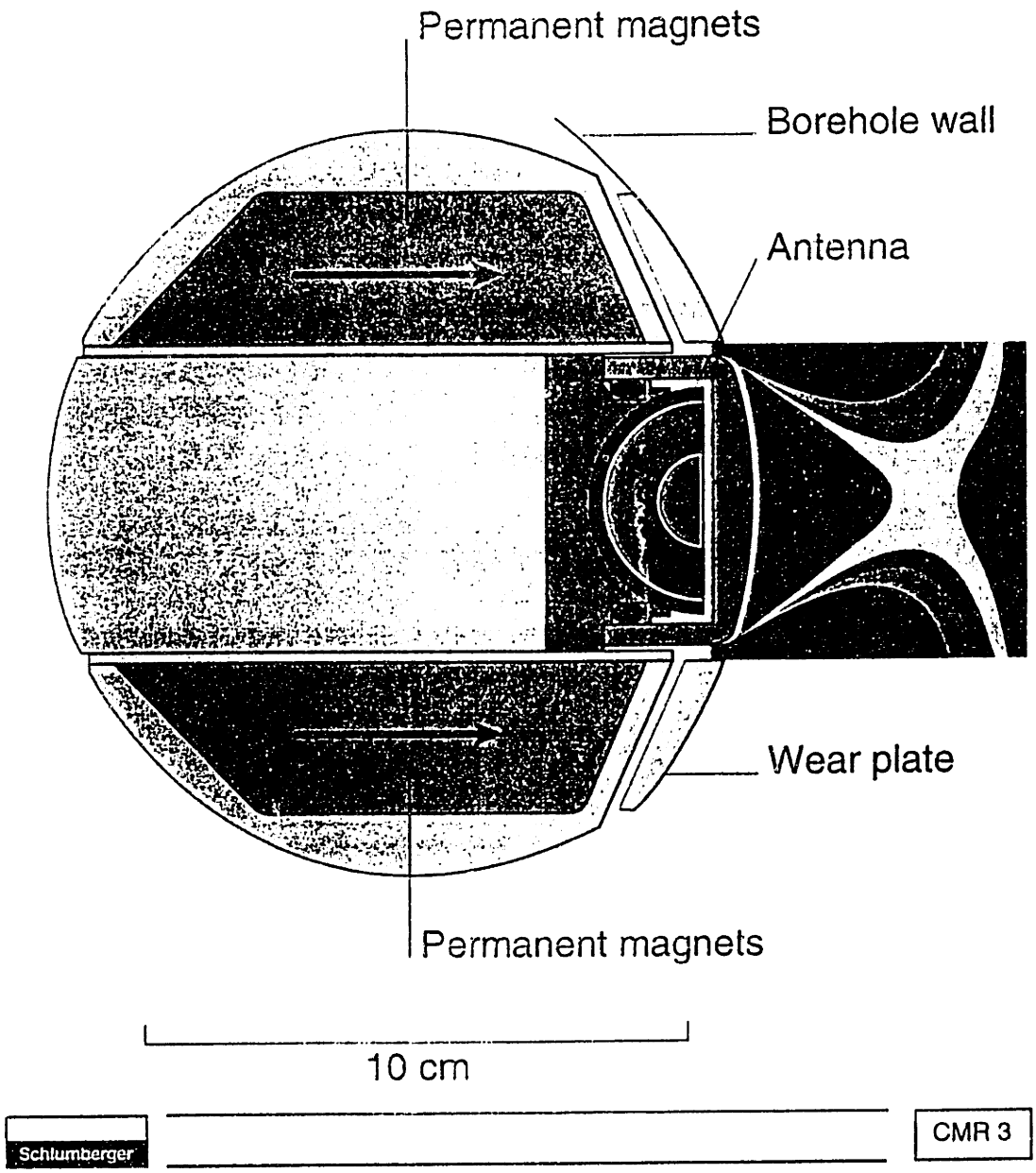

Figure 4.10 The CMR sonde cross-section showing the magnetic field shape on the right. From Morriss, 1995.

Chapter 5

Nuclear Magnetic Resonance Log Examples and Evaluation

This chapter describes the typical presentation of processed MRIL data. The first section presents the log and header presentation information from a conventional log output as processed by the NUMAR Corporation's analysis system. The log includes all the main curves as measured by the regular wireline services, such as resistivity, gamma-ray data, spontaneous potential, and porosity from neutron density on acoustic travel time. Along with the main log curves, the NMR curves are displayed—for example, the bins, the T_2 distribution, FFI, BVI, and MPHI. The saturation model, which is a version of the dual-water model (Clavier et al., 1984), is adapted for use with the parameters from the MRIL as input parameters.

The chapter includes the first iteration of the novel interpretation scheme developed by the thesis research. It also includes some of the first examples of the application of MRIL to evaluate formations in the Travis Peak and Cotton Valley of the East Texas Basin. The last section deals with optimum acquisition of NMR data. The weighting of CPMG pulse sequences to obtain optimal imaging of the formations and pore fluids is described.

5.1 Log Presentation

The standard presentation of log curves as processed by the NUMAR Corporation's MRIAN (Magnetic Resonance Imaging Log Analysis) is provided and interpreted in Figure

5.1. The printout heading is displayed in Figures 5.2a and 5.2b. The presentation combines data from the conventional suite of logs and the MRIL NMR data. Measured and calculated curves are displayed side by side to enable "quick-look" interpretation of the zones of interest. The curves fall into four tracks. The tracks read from left to right, with track one on the left.

Track 1 is a linear scale with 10 equal divisions. To the left are caliper (measured in inches), spontaneous potential (SP, in mV), photoelectric effect cross-section (PEF, in barns/El), and gamma-ray (GR, in API units), all conventional logs. The right-hand side of the first track is the bin display, given in porosity units (pu) and read right to left. In the data in the thesis, inversion is typically for eight bins; in other applications, in which many echoes are taken, nine or 10 bins are displayed. Bin 4 is the fill between the first four bins' total porosity and the first three bins' total porosity. The total effective porosity (MPHI) is the sum of all the bins; MPHI can be made up of only the first five bins if bins 6, 7, and 8 are all zero. When multiple passes are used, it is imperative to know the T_R of the pass from the bins displayed because the bin distribution changes as the wait time changes. Because the bin display is used to infer the pore size distribution, it is important to use the bins from a short-wait-time pass to ensure that the hydrocarbons are not recovered.

Track 2, a logarithmic scale with five decades, contains the resistivity curves from conventional logging and the permeability curve derived from NMR data (MPERM). The resistivity is given from three depths of investigation; deep and medium induction logs (ILD and ILM) and a spherically focused log (SFL), using a scale of 0.01 to 1000 ohm-m. The permeability curve, MPERM, is derived from FFI, BVI, and the total effective porosity (MPHI); the MPERM scale is 0.01 to 1000 millidarcies (md). Other equations for permeability (see Equation 3.1) can be used to adapt the coefficients of MPERM for specific formations. New coefficients and the overall form of Equation 3.1 can be made formation specific when NMR core studies are done (as was the case in analysis of the Travis Peak and Cotton Valley formations in East Texas, discussed below).

Track 3 is a variable density log (VDL) of the T_2 distribution. The VDL is another way of looking at the bin distribution of the formation. The logarithmic scale has 10 equal divisions, and, unlike for the bins in track 1, reading is from left to right. The first bin is centered at 4 ms, and the tenth bin is centered at 2048 ms. The VDL value for each bin is the partial porosity for that bin (i.e., the thickness of each bin in the first track). Values are represented by colors: the hotter the color of a bin, the greater the bin's porosity. VDL is, in fact, the T_2 distribution for the given depth on the log. In core analysis and many other NMR displays, the distribution is a bimodal wiggle trace (Figure 5.3). The advantage of not using a wiggle for a log presentation is that adjacent distributions do not interfere with each other as in a full wave acoustic log presentation.

Track 4, another 10-division linear scale, contains the porosity data from both conventional and NMR logging. The scale is 0 to 30 pu, and reading is right to left. The neutron and density logs are played back on the appropriate matrix, where limestone is used in a limestone matrix and sandstone in a sandstone matrix, so that there is no excess gas effect. Other porosities displayed are the effective porosity (MPHI) and bulk volume irreducible (BVI) from NMR logging. Bulk volume water effective (BVWE) is calculated from the MRIAN model and represents the total effective water in the pore space. Light-gray fills represent the capillary-bound water (see Figure 5.2a). The cross-hatched fill (movable hydrocarbons) and white fill (movable water) between the MPHI and BVI curves are derived from the dual-water saturation model. This model, discussed in section 5.2, divides the FFI into two parts. Note that the effective porosity is less than the cross-plot of the neutron and density values, as would be expected; the difference should be equal to the clay-bound porosity and microporosity not detected by NMR.

5.2 Saturation Models

The ability of NMR logging to measure capillary-bound water and effective porosity makes for excellent input into the dual-water model (Clavier et al., 1984) for saturation calculations. The model is one of the most accurate in evaluating low-resistivity pays in

shaley sands (Dewan, 1983). It is one of two models that uses cation exchange capacity (CEC) to assess the conductivity of the clay-bound water.

5.2.1 Waxman–Smits Model

The Waxman–Smits model was proposed by M.H. Waxman and L.J.M. Smits of Shell Oil Co. in 1968. It uses the idea from double layer theory that CEC accounts for the increased conductivity of clay-bound water. Clay platelets tend to have very high surface-to-volume ratios. The large surface area of clays has a negative charge density, which causes sodium ions to form a thin layer on the surface of the clay. This distribution of excess Na^+ over the clay is schematized in Figure 5.4. There is a layer of adsorbed water, and then hydrated sodium ions to balance the net negative charge of the clay surface due to broken bonds and ions substituted into the clay lattice. The conductivity in the double layer contributes where the water has an excess of cations. In Waxman–Smits the effective water conductivity, C_{WE}, is made up of the water in the pores (from both BVI and free water) and the conductivity of the clay-bound water due to CEC:

$$C_{WE} = C_W + BQ_V \tag{5.1}$$

C_W mhos/m is the conventional water conductivity equal to $1/R_W$, and BQ_V is the conductivity due to CEC. Q_V is the normalized CEC given in milliequivalents per unit of pore volume. B is the specific conductivity,

$$Q_V = CEC\ \rho\ (1-\phi)/\phi \text{ meq/cc} \tag{5.2}$$

of the counter ions in the double layer mhos/m per meq/cc. If there are hydrocarbons in the pore space, they displace the free water and the CEC term increases, yielding a new equation for effective water conductivity:

$$C_{WE} = C_W + BS / S_{WT} \tag{5.3}$$

Using Archie's saturation model with m = n = 2 yields a new value for the total conductivity, C_t:

$$C_t = (S_{WT} \cdot \phi_t)^2 (C_W + BQ_V/S_{WT}) \tag{5.4}$$

The model can be used to find S_{WT} given C_t, C_W, ϕ_t, but there is a problem in that there is no log that measures BQ_V. Values are normally derived from core work or other methods.

5.2.2 Dual-Water Model

The dual-water model, developed by C. Clavier, G. Coates, and J. Dumanoir of Schlumberger, extends and improves the Waxman–Smits model because in the latter there is no partition of the two types of water conductivity. Also, it is more easily adapted to NMR measurements. Its distinction is between the conductivity of the free water and the clay-bound water. In the model, the "free water" includes both the mobile and capillary-bound (BVI) water; the partition of porosity is total porosity (effective porosity plus clay-bound porosity), as shown in Figure 5.5.

The bulk conductivity (C_{WE}) is made up of free water conductivity plus bound water conductivity (C_{CW}) owing to cation exchange, as shown:

$$C_{WE} = (1 - S_B)\, C_W + S_B\, C_{CW} \tag{5.5}$$

Here, S_B, the saturation of the clay-bound water, is

$$S_B = V_Q\, Q_V \tag{5.6}$$

where V_Q is the amount of water in grams of water per milliequivalent of cations and Q_V is the number of milliequivalents per cc of fluid. It has previously been shown that the

specific CEC is proportional to the specific area for clays (Dewan, 1983) (Figure 5.6). Properties of four predominant clay types—montmorillonite (smectite), illite, chlorite, and kaolinite —are shown in Table 5.1.

The next step is to find the conductivity of the clay-bound water (C_{CW}). The conductivity (as before in Waxman–Smits) is

$$C_{CW} = B\, Q_{CW} \tag{5.7}$$

where B is the specific conductivity and Q_{CW} is the specific CEC of the clay-bound water (which is not the specific Q_V above and in Figure 5.6).

Here in the claybound water, the concentration of cations is higher and is given as

$$Q_{CW} = \frac{Q_V \phi_t}{V_{CW}} \tag{5.8}$$

The concentration of the cations in the total volume is divided by the clay-bound volume.

$$V_{CW} = S_B \cdot \phi_t = V_Q\, Q_V\, \phi_t \tag{5.9}$$

Therefore, if Equation 5.9 is plugged into Equation 5.8, and then 5.8 is plugged into 5.7,

$$C_{CW} = \frac{B}{V_q} \tag{5.10}$$

for an equation in which C_{CW} is made up of two variables that are dependent only on temperature, not on clay type.

To get a final value for C_{WE}, which is the effective total dual-water conductivity, the effect of hydrocarbons in the pore space must be included, taking into account that hydrocarbons displace the free water while the clay-bound water remains constant. This affects the overall distribution between free and bound water in the final equation,

$$C_{WE} = C_W (1 - S_B / S_{wt}) + C_{CW} S_B / S_{wt} \tag{5.11}$$

Equation 5.11 can be applied directly with NMR data to give a bulk water saturation, S_{wt}.

$$C_t = (S_{wt} + \phi_t)^2 [C_W (1-S_B/S_{wt}) + C_B \cdot S_B/S_{wt}] \tag{5.12}$$

This equation can be solved quadratically from S_{wt} with the assumption that in Archie's saturation model m = n = 2 and a = 1, where the general form of Archie's relation is

$$S_{wt}^n \frac{a}{\phi_t^m} \frac{C_t}{C_w} \tag{5.13}$$

Solving the quadratic for the positive root yields the saturation

$$S_{wt} = -\frac{S_b(C_b - C_w)}{2C_w} + \sqrt{\frac{S_b^2(C_w - C_b)^2}{4C_w^2} + \frac{C_t}{\phi_t^2 C_w}} \tag{5.14}$$

S_b can be measured with the newest version of the MRIL (the MRIL-C_{TP}) in which the T_E is 0.5 ms and there is a special pulse sequence for measuring clay-bound porosity. Alternatively, S_b can be calculated from the difference in the total porosity measured by neutron, density, or sonic logging and the effective porosity, ϕ_e, measured by NMR logging. The last step is to rewrite Equation 5.10 for C_{CW} as a function of temperature:

$$C_{CW} = 0.000216\,(T_F + 504.4)\,(T_F - 16.7) \tag{5.15}$$

Once S_{wt} is found from Equation 5.14, it can be used to calculate the bulk volume water (BVW) in pu:

$$BVW = S_{wt} \cdot \phi_t \tag{5.16}$$

This value can be graphed, as displayed in track 4 of an MRIL presentation (Figure 5.1). Next, the value of BVW is compared with BVI (capillary-bound water curve) measured by NMR. If the BVW from Equation 5.16 is greater than BVI, the crossover appears as a white area in track 4 and represents movable water. If BVW is not greater than BVI, the remaining effective pore space is filled with movable hydrocarbons (see the dual-water porosity model in Figure 5.5).

5.3 Log Examples

Six MRIL logging examples are provided (Figures 5.7 to 5.12) to illustrate the evolution of NMR well imaging and interpretation. Example 1 (Figure 5.7) is from the original logging by the MRIL-B tool of a formation in the East Texas Cotton Valley and Travis Peak series. The original processing of the MRIL-B did not have bins; the bins in track 1 and the VDL display in track 3 were not included in the original processing. The data were reprocessed using the MAP inversion scheme. The only NMR data available at the time the well was drilled are displayed in the fourth track: BVI, MPHI, and the dual-water model. Notice that the data from the old tool were noisy; there is an artifact (showing porosity) in bin 8 everywhere on the log. The artifact can most easily be seen as a line that appears on the right side of track 3 in the VDL display. Rectified noise in the latter part of the echo data, which is filtered out in the newer versions of the tool, accounts for the artifact.

The well was not drilled for the bottom zones at X262 and X296, but the model shows that although the resistivity is only 4 ohm-m, both zones were calculated as productive. The upper zone shows very little movable water, with a high BVI (4.5 pu) and an effective porosity of 8 pu. The lower zone shows 3 pu of movable water. Given these results, mud log findings of 65 units in the upper zone and 35 units in the lower zone, the upper zone was assumed productive and the lower zone was assumed wet.

The upper zone was perforated and produced naturally for 1 year, with an initial production of 1.5 million cubic feet of gas per day (MMCFPD) and a cumulative production of 0.43 billion cubic feet of gas (BCF). The zone reached financial limits after 1 year, and perforation of the lower zone showed it, too, to have no moveable water. This was a first indication that the dual-water approach should be used as a "quick look" and not as the final answer. In fact, the pore size given in track 1 may be the most important element in evaluating formations with NMR logs. The method of using this distribution is developed in the discussions of the other examples.

The lower and upper zones were then stimulated and produced another 0.75 BCF in the next year and a half. The study of these zones provided a breakthrough in understanding the nature of certain tight sand formations. The sands that are depleted from natural production may produce even more gas after stimulation than the initial production. Beyond the significance for new tight gas-sand field discoveries, this opens the possibility of going back to many old fields and vastly improving the recovery of reserves.

Example 2 (Figure 5.8) shows the value of the new method of evaluation using the bin distribution. The uppermost zone in this example from X430 to X450 represents a conventional pay zone. The effective porosity is 10 pu, with high resistivity (around 30 ohm-m) and BVI of 3 or less depending on whether a 3- or 4-bin BVI was used. (The BVI was assumed to be 4 bins for analyses.) The mud log demonstrated a 120-unit gas show. Track 1 shows a fairly even grain size, with porosity in bins 5, 6, and 7 and little BVI in bins 1, 2, and 3. The zone produced about 0.5 BCF in 1 year and then depleted.

At this point, the question would be whether or not to stimulate as in the Example 1. Here, the conventional analysis would lead to the zone's being abandoned. The zone from X450 to X470 is clearly wet on the conventional log. The resistivity is 2 ohm-m, and the gas show dropped to background levels. If the bin distribution is compared with the shale at X450, it is more similar to a shale than a sand. There is 6 pu out of 9 of BVI and very little porosity in bins 6 and 7 (which points to the zone's being a siltstone); there would probably act like shale on stimulation. The zone below at X500 to X510 also had a moderate show of 60 units, although tight with a 6 pu effective porosity. However, the bins show larger pores, with predominance of bins 5, 6, and 7 and less BVI, making this zone a strong candidate for hydrofracturing. The zone from X560 to X580 also is a good fracturing candidate because the bins show that when the resistivity dips to below 2 ohm-m, the sand becomes very silty and is mostly BVI. The entire interval was stimulated with 500,000 lb of sand, had an initial production of over 2 MMCFPD, and is still producing at 900 MCFPD over a year later. Conventional analysis would have assumed all the zones were wet or too near wet zones to stimulate, so all the additional reserves would have been left behind.

The dual-water model predicted movable water in the two zones (at X460 and at X568) when there was none. This emphasizes why the use of bin distribution is critical in the analysis, and the method implies that the information in track 4 should be used only as a reconnaissance pass of the log analysis.

Example 3 (Figure 5.9) shows why conventional methods such as drill stem testing (DST) and mud logs are not always reliable. The zone at X570 was assumed nonproductive (although it looks like a conventional zone from dual-water resistivity or from the bins) because the mud log show was less than a 4-unit increase over background. The zone was perforated and flowed initially at 3 MMCFPD. Because of this result, the other wells in the field were drilled deeper and the most prolific sands in the field were discovered.

The set of zones in Example 4 (Figure 5.10) began the study of a type of low-resistivity pay that had gone untested in the entire basin because it was always assumed to

be nonproductive. These sands have revitalized exploration of Cotton Valley in the East Texas Basin. The zone from X860 to X900 was drill stem–tested after having a 36 ft drilling break with a maximum show of 270 units. The test calculated a rate of 1.7 MMCFPD and no movable water. While the zone showed tremendous gas from the differential spectrum (see Chapter 6 on hydrocarbon imaging), dual-water analysis showed movable water in track 4. The other anomalous thing about the zone was its BVI and bin distribution. In an attempt to modify the model to show less movable water, it was assumed at the time that a 4-bin BVI should be used, which proved to be incorrect. In track 1, there was almost no porosity in the first three bins, yet there is very low resistivity (1 ohm-m) and no movable water.

Sidewall core analysis with scanning electron microscopy (SEM) showed smectite and a mixed layer of smectite with illite. Smectite is known to have the highest CEC (see Table 5.1), and this clay type on the photomicrographs seemed to coat the grain surfaces like a layer of honey. The grain-coating high CEC sometimes acts like a short circuit in the parallel-resistivity saturation models such as dual-water and Waxman–Smits. The short circuit makes resistivity and conventional logs insensitive to hydrocarbons.

Once again the bin distribution in track 1 and hydrocarbon imaging (Chapter 6) provide the most reliable way to find these low-resistivity zones filled with smectite and illite. The signature of these zones is a predominance of bins 4/5 or 5/6, with bin 7 rarely seen and bin 8 never seen, and a striking lack of bins 1 through 3. This simple pattern matching has been used by some to locate these zones. These zones can produce naturally for a while but need stimulation to be drained effectively. Care must be taken in stimulating these zones because the fracturing fluids easily damage the clays.

The zone at X990 to X000 showed little gas upon perforation; the zones at X935 to X945 and X860 to X990 had an initial production of more than 3.5 MMCFPD. The zones have been stimulated and will have an ultimate recovery in excess of 1.6 BCF.

Example 5 (Figure 5.11) is another zone with clay-lined pores. It tested in excess of 1.6 MMCFPD. Also, it was found in an entirely different geological setting than the other examples. Once again, the bins show that it is probably a smectite zone with no movable water.

In view of what has been learned about the other zones, it is instructive to return to Example 3 (Figure 5.9). The zone at X445 to X455 makes little sense because the dual-water model in track 3 shows water on top of gas. The bins in track 1 show that it has mostly BVI, so it is not a smectite zone. Therefore, it is probably a very silty zone with gas in it. The lowest zone was productive, as stated, but there was only a very slight gas show on the mud log. The zone from X475 to X505 also had a very slight show but was thought at the time to be wet. When the well was originally logged, there was not a bin presentation in track 1 and nothing was known about the clay-coated grains. Nearby wells are producing out of these zones. It is now known that the well is probably productive, and it is scheduled to be tested in the near future.

The final example (Figure 5.12) represents the second breakthrough in understanding of a nonconventional pay through using the information from the NMR data. The zones were known to be quite tight and because of the small shows, the entire interval from X690 to X880 was tested. The zone showed little flow rate (at most about 20 MCFPD). The dual-water showed mostly very high BVI and also a good deal of movable water. The bins in track 1 show a large amount of bins 1, 2, 3, and 4, but very little at any of the larger pore sizes. The core work has also shown these zones to have very small pores and S_{wt} in the 70% range. The zones were stimulated and had an initial production in excess of 1.4 MMCFPD. The well has produced more than 0.75 BCF in 14 months and will ultimately recover in excess of 1.5 BCF. In these sands, the resistivity is low because there is a large amount of BVI. The effective porosity is 3 pu below the cross-plotted porosity at X694, representing clay-bound porosity or microporosity missed by the NMR log.

In the above type of formation, it is learned from the bins that the zones that are gas

filled will move gas, while the zones that get stimulated that are not gas filled act like shale or siltstone and simply make no fluids at all. Many of the above types of zones also come with very prolific conventional pays mixed in with the very high BVI sands. Many of these conventional zones were produced but never stimulated because of the fear of water from nearby sands. The NMR data help find numerous new pays in formations that were produced and not depleted, or pays in formations that were bypassed completely.

5.4 Optimum Acquisition of Nuclear Magnetic Resonance Logs

As reviewed in Chapter 2, the relaxation equation is

$$\frac{1}{T_1} = \frac{1}{T_{1Bulk}} + \frac{1}{T_{1S/V}} \tag{5.17}$$

The bulk T_1 of water is 3500 ms, whereas the T_1 in porous media is between 1 and 750 ms for all sandstones and carbonates in the fast-diffusion limit. The equation for the second term (the surface-to-volume term) is

$$\frac{1}{T_{1S/V}} = \rho_1 \frac{S}{V} \tag{5.18}$$

where T_1 is the longitudinal recovery time, ρ_1 is the surface relaxivity constant, and S/V is the surface-to-volume ratio of the pore space. It is known from water-filled pores in sand or dolomite without vugs or fractures that the S/V term dominates and the fast-diffusion limit applies. The NMR tools in use all measure T_2 and not T_1, but for most sand the ratio of T_1 to T_2 is constant and approximately equal to 1.5. Because T_1 and T_2 have a constant relation, the equation can be rewritten as

$$\frac{1}{T_2} = \rho_2 \frac{S}{V} \tag{5.19}$$

where ρ_2 is the constant surface relaxivity related to T_2.

A constant relation of 1.5 between T_1 and T_2 is seen in Table 5.2, where the percentage of longitudinal recovery from each bin is shown as a function of wait time (T_W). For bin 7, which has a T_2 of 256 ms, T_1 equals 384 ms; with a wait time of 1 s, 93% of the magnetization M_0 is recovered. With a T_W of 0.75 second, only 86% is recovered. The trend of the table shows that as the wait time grows shorter and shorter, water starts to be underrecovered in the earlier bins. The less water recovered, the less T_2 will be measured, and porosity in the bin will be undercalled. At a wait time of 0.5 s, all of bin 5 has just been recovered. Bin 6 is fully recovered at T_W = 1 s, bin 7 is 98% recovered at 1.5 s, and bin 8 is 96% recovered at 2.5 seconds.

This means that if the zone is wet and flushed with filtrate, all the porosity in all eight bins will be fully recovered. Real data, however, have noise, so the echoes in the time domain are measured and the data are inverted to obtain the T_2 distribution. The calculated T_2 is a nonlinear least-squares fit of data with noise. The noise in the data smears the T_2 in the bin distribution. To understand how the noise in the data affects the T_2 distribution, it is important to look at some of the techniques of medical imaging.

It is known that protons in the water in porous media relax by means of surface interactions. The protons in oil and gas, however, are not part of the wetting phase, so they relax through other mechanisms. T_1 for gas at 5000 psi and 250 °F is 4.2 s, but T_2 for gas in a gradient field is 34 ms (because of diffusion). T_1 for water in vugs is 3500 ms, as is T_2. Therefore, depending on the situation the more important parameter to measure is sometimes T_1 and sometimes T_2 (or possibly even some combination can be best). It is the tailoring of the CPMG pulse sequence to measure different contrasts of T_1 and T_2 that is used in medical imaging; this approach can also be applied successfully to NMR logging

data acquisition.

There are three basic types of weightings (Bushong, 1996) of the CPMG pulse sequence to visualize different types of contrasts between T_1 and T_2 and the density of protons, namely, T_1, T_2, and spin-density weightings. The degree to which different weighting can affect NMR imaging outcome is shown in Figures 5.13 to 5.15, which display MR images of the human brain. There is a spin-density contrast of 20% between the white and gray matter of the brain (Figure 5.13). The T_1 of gray matter is about 700 ms, and the T_1 of white matter is about 500 ms, for about a 30% contrast (Figure 5.14). A T_2 image (Figure 5.15), on the other hand, shows no contrast between gray and white matter because the T_2 for both tissues is about 100 ms.

To understand how to go about setting up productive T_1-, T_2-, or spin density–weighted imaging, it is best to return to the physics of T_1, T_2, and the CPMG. To recover the M_z (magnetization in the z direction), the wait time (T_W) or repeat time (T_R) is set long. To see a T_1 contrast, the magnetization needs to be fully recovered for one species and only partially recovered for another. Table 5.2 shows that at T_W of 0.75 s, the first six bins are fully or essentially fully recovered, but bins 7 and 8 are only partially recovered. At T_W of 2.5 s, all the bins are fully or essentially fully recovered. In effect, once T_W exceeds 2.5 s, there is no T_1 contrast because all the bins are fully recovered. In a T_1-weighted pulse sequence, T_W should be short (less than 2500 ms), and, to minimize the T_2 effects (see next), T_E (the time between echoes) should be short.

To understand how to T_2-weight the imaging advantageously, one needs to think of the CPMG pulse sequence (see Horowitz, 1995). T_E is the amount of time the transverse magnetization (M_{xy}) is allowed to dephase once it has been tipped into the transverse plane. Echoes are created to keep the magnetization in the transverse plane and to prevent its decay through free induction decay at T_2*. This means that with very short T_E, T_2 decay is minimized per echo; with longer T_E, the effect of T_2 is enhanced. In a T_2-weighted pulse sequence, T_E needs to be greater to enhance the T_2 decay contrast, and T_W needs to be long

to diminish the effects of T_1 contrast.

The spin-density, or balanced-pulse, image is weighted not to enhance T_1 or T_2, but to see the density of protons in the sensitive volume of the NMR experiment. To diminish the effects of T_1, long wait times are used; to diminish the effects of T_2, T_E should be short.

It could be argued that all the pulse sequences used in the NMR well logging experiments are spin-density, or balanced, sequences because T_E is 1.2 ms and T_R is 2 s or greater. However, in the case of small pores in the formations, which are predominantly in the first four bins (as in Figure 5.12), a wait time of 1 s gives a better answer from BVI and MPHI than do longer wait times, of, say, 3 s (or longer). As discussed above, the shorter wait time enhances T_1 weighting. Table 5.2 provides guidance for sequence focusing regarding a given bin as the next bin begins to recover partially. A wait time of 0.5 s focuses on bin 5, 1 s focuses on bin 6, 1.5 s focuses on bin 7, and 2.5 s focuses on bin 8. These relations are loose because the mineralogic characteristics of the sand can cause ρ_2 (the surface relaxivity of the pores) to change. Thus, the ratio of T_1 to T_2 would no longer equal 1.5. Importantly, the trend of real data acquired by NMR logging is that shorter wait times do better for BVI and smaller grain sands, and longer wait times recover more porosity in oil, gas, and the larger-grained sands.

The trends described above should be kept in mind when acquiring data. When a log is run in a new area where the pore fluids and T_2 distribution are not known, a reconnaissance pass of the log may be needed to optimize the acquisition parameters before the main pass is done.

Knowing the physics of NMR is important to understanding how to obtain and interpret the log data. To optimize interpretation, the pulse sequence should be designed with appropriate T_1 and T_2 weighting in relation to the pore size of the sands under study. It is critical to understand how the data can change as the wait times change and as the weighting of the pulse sequence is changed. This knowledge can greatly enhance formation

evaluation and log interpretation. The standard method of acquiring NMR data, used by most oil companies as well as logging companies, involves in a single pass of the log, maximizing the recovery of the eighth bin for sands with gas or ninth bin for sands with oil, and ninth or tenth bin for carbonates. The method described in this thesis often requires more than one pass, and includes using wait times that maximize recovery of the predominate bin of the formation in question. The second method, while requiring somewhat more logging time, provides a more robust and repeatable answer.

Table 5.1 Clay Properties

Clay Type	CEC meq/g	Specific Area m^2/g	ϕ_{CNL}	ρ (average) g/cc	Minor Constituents
Smectite	0.8-1.5	700-800	0.24	2.45	Ca, Mg, Fe
Illite	0.1-0.04	113	0.24	2.65	K, Mg, Fe, Ti
Chlorite	0-0.1	42	0.51	2.8	Mg, Fe
Kaolinite	0.03-0.06	15-40	0.36	2.65	-

From Dewan, 1983, and Ellis, 1987.

Table 5.2 Recovery of Net Magnetization for T_1 vs. Wait Time (T_W)

Bin	T_2	T_1	T_W=0.25	T_W=0.5	T_W=0.75	T_W=1	T_W=1.5	T_W=2.5
1	4	6	100.00%	100.00%	100.00%	100.00%	100.00%	100.00%
2	8	12	100.00%	100.00%	100.00%	100.00%	100.00%	100.00%
3	16	24	100.00%	100.00%	100.00%	100.00%	100.00%	100.00%
4	32	48	99.45%	100.00%	100.00%	100.00%	100.00%	100.00%
5	64	96	92.60%	99.45%	99.96%	100.00%	100.00%	100.00%
6	128	192	72.80%	92.60%	97.99%	99.45%	99.96%	100.00%
7	256	384	47.85%	72.80%	86.82%	92.60%	97.99%	99.85%
8	512	768	27.78%	47.85%	62.34%	72.80%	86.82%	96.14%

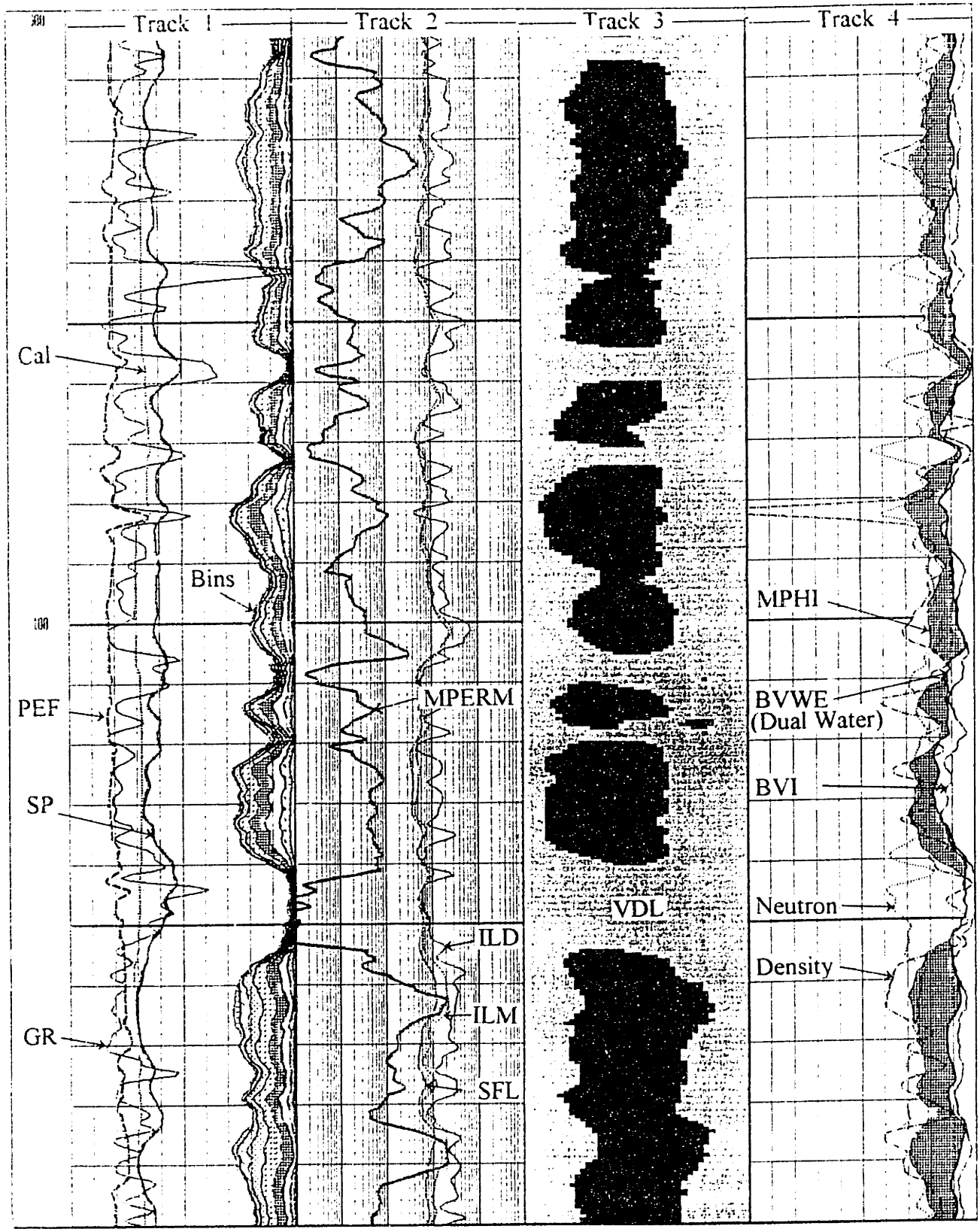

Figure 5.1 Standard NUMAR MRIAN log presentation. Track 1: Cal, caliper (inches); SP, spontaneous potential (mV); PEF, photoelectric effect (b/E); GR, gammarays (API units) (all conventional measures); bins. Track 2: MPERM, NMR-derived permeability (calculated) (md):. Resistivity (all ohm-m and all conventional)—ILD, deep induction log; ILM, medium induction log; SFL, spherically focused log. Track 3: VDL, variable density log (pu). Track 4: Porosity (all pu)—neutron (conventional); density (conventional); MPHI (effective porosity); BVI, bulk volume irreducible; BVWE, bulk volume water effective (calculated). Note that track 4 (porosity) and the bins in track 1 are read right to left.

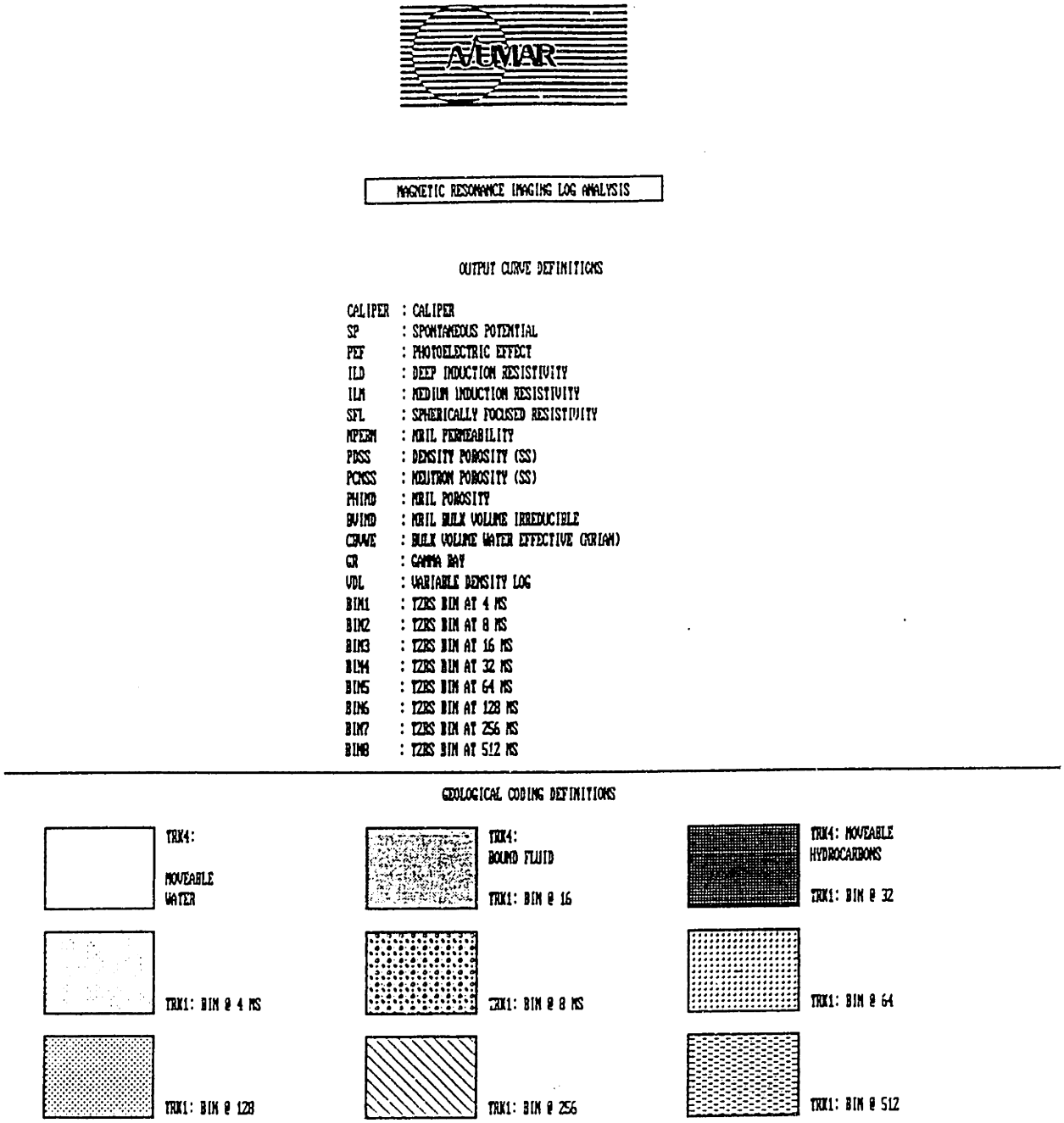

Figure 5.2a Heading of the NUMAR MRIAN (Magnetic Resonance Imaging Log Analysis) presentation, including definition of the output curves and geological coding for the curve fills. Continued as Figure 5.2b.

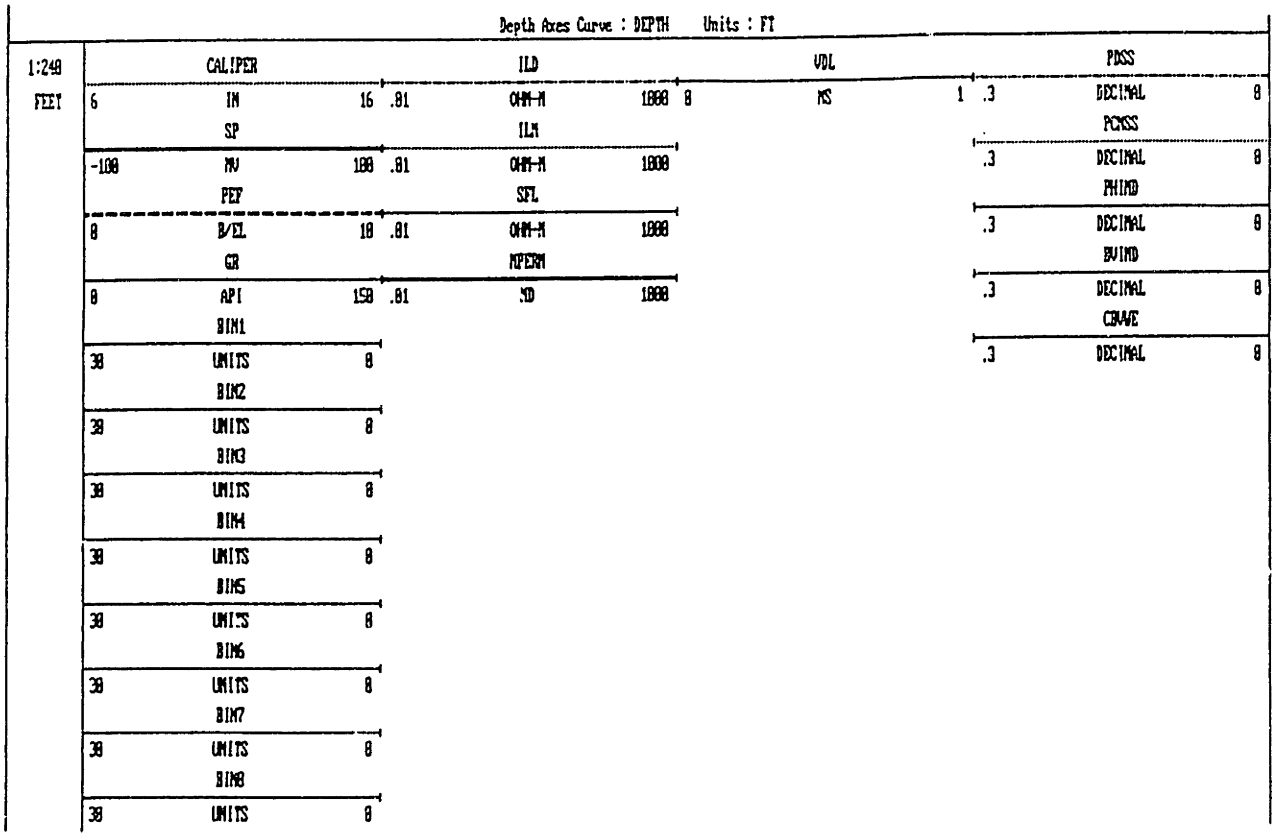

Figure 5.2b Heading of the NUMAR MRIAN presentation (continued), showing the four tracks of the display and the curve ranges within the tracks.

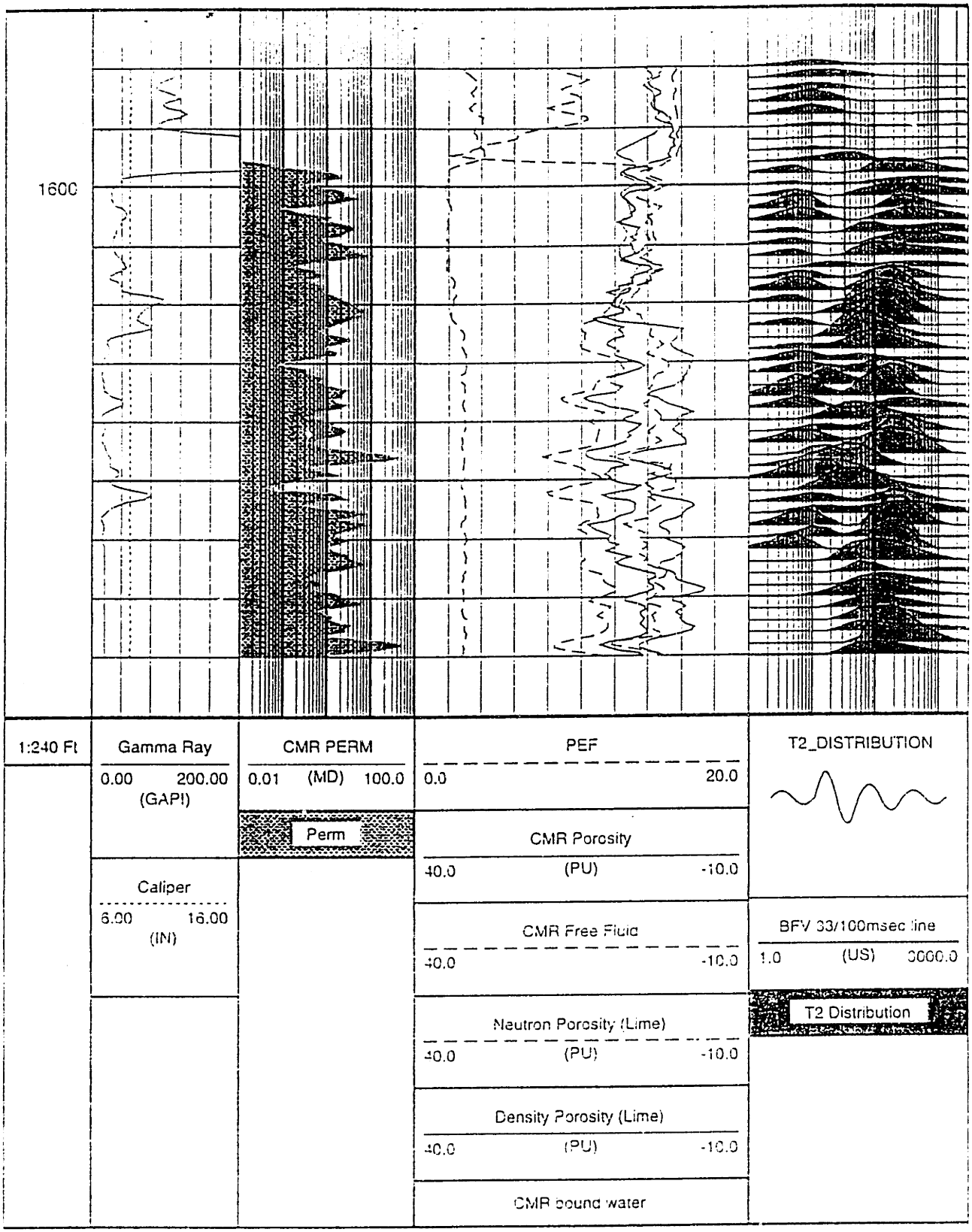

Figure 5.3 The appearance of the T_2 distribution as a wiggle trace is seen in the fourth track of this Schlumberger CMR log presentation. From Morriss, 1995.

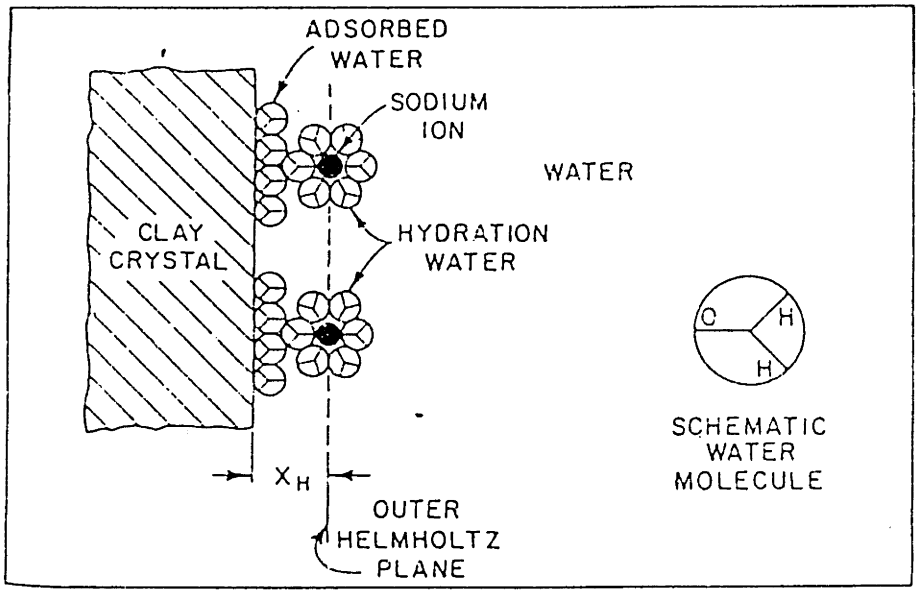

Figure 5.4 The double layer near the clay surface, where Na^+ exceeds Cl^-, and where the cation exchange capacity dominates the conductivity of the water. From Clavier et al., 1984.

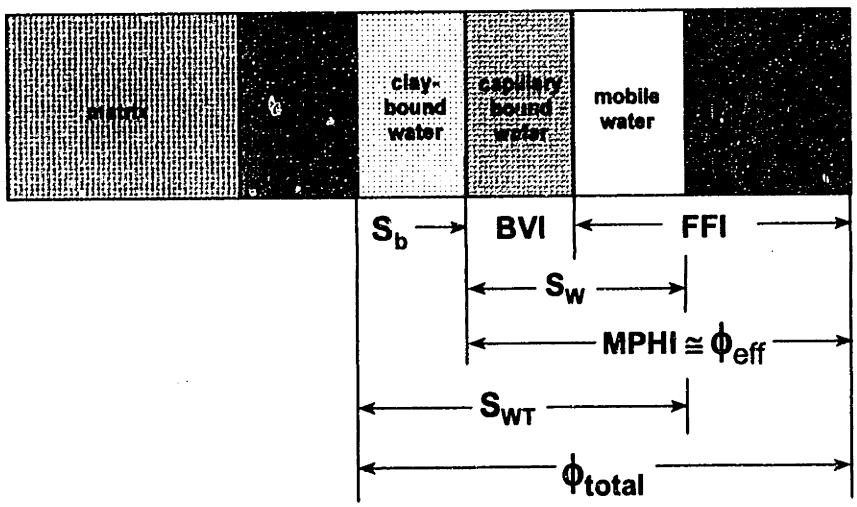

Figure 5.5 The dual-water porosity model and its relation to quantities measured by NMR, namely, BVI, FFI, and MPHI. Adapted from Cherry, 1995.

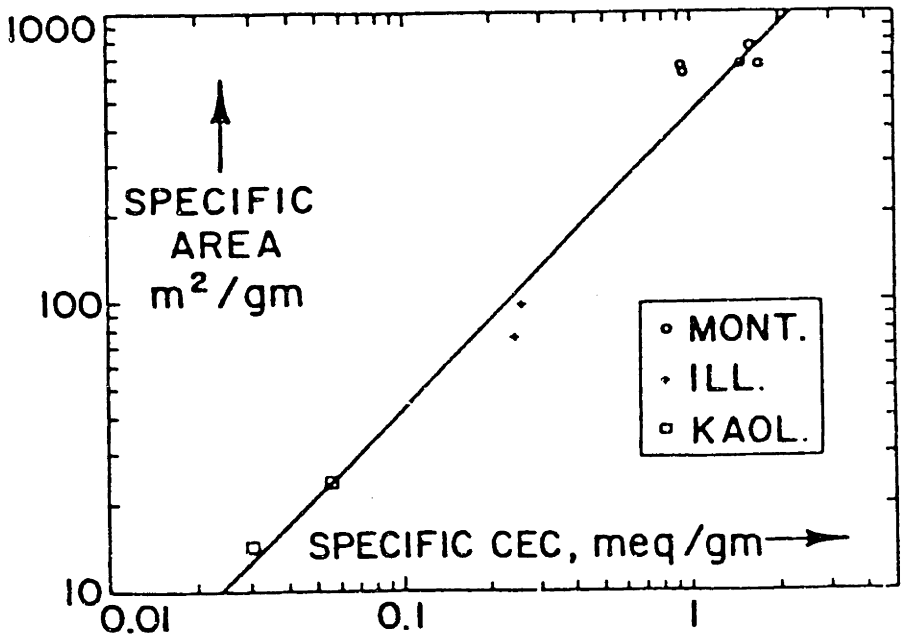

Figure 5.6 The relation between specific surface area and specific CEC is plotted for montmorillonite (smectite), illite, and kaolinite. From Dewan, 1983.

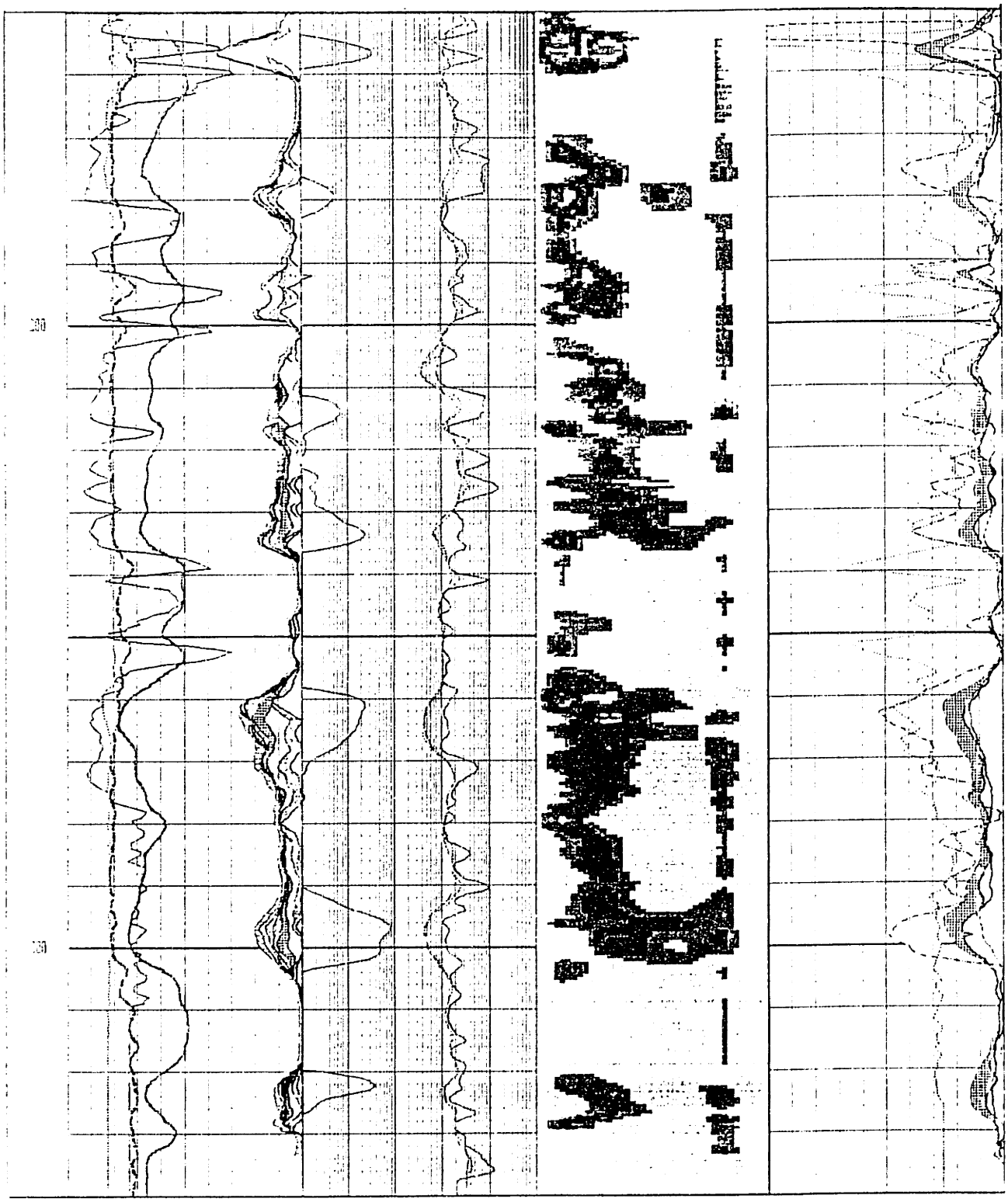

Figure 5.7 Example 1. The zones from X260 to X270 and X295 to X305 both have low resistivity (4 ohm-m) and are conventionally wet. Dual-water analysis showed the top to be productive and the bottom to have some movable water. The upper zone produced 0.43 BCF naturally during 1 year. The lower zone proved to have no movable water, so both zones were stimulated together and produced another 0.75 BCF in the next 1.5 years. Note that the bin data in track 1 and VDL in track 3 represent later reprocessing of the MRIL-B data.

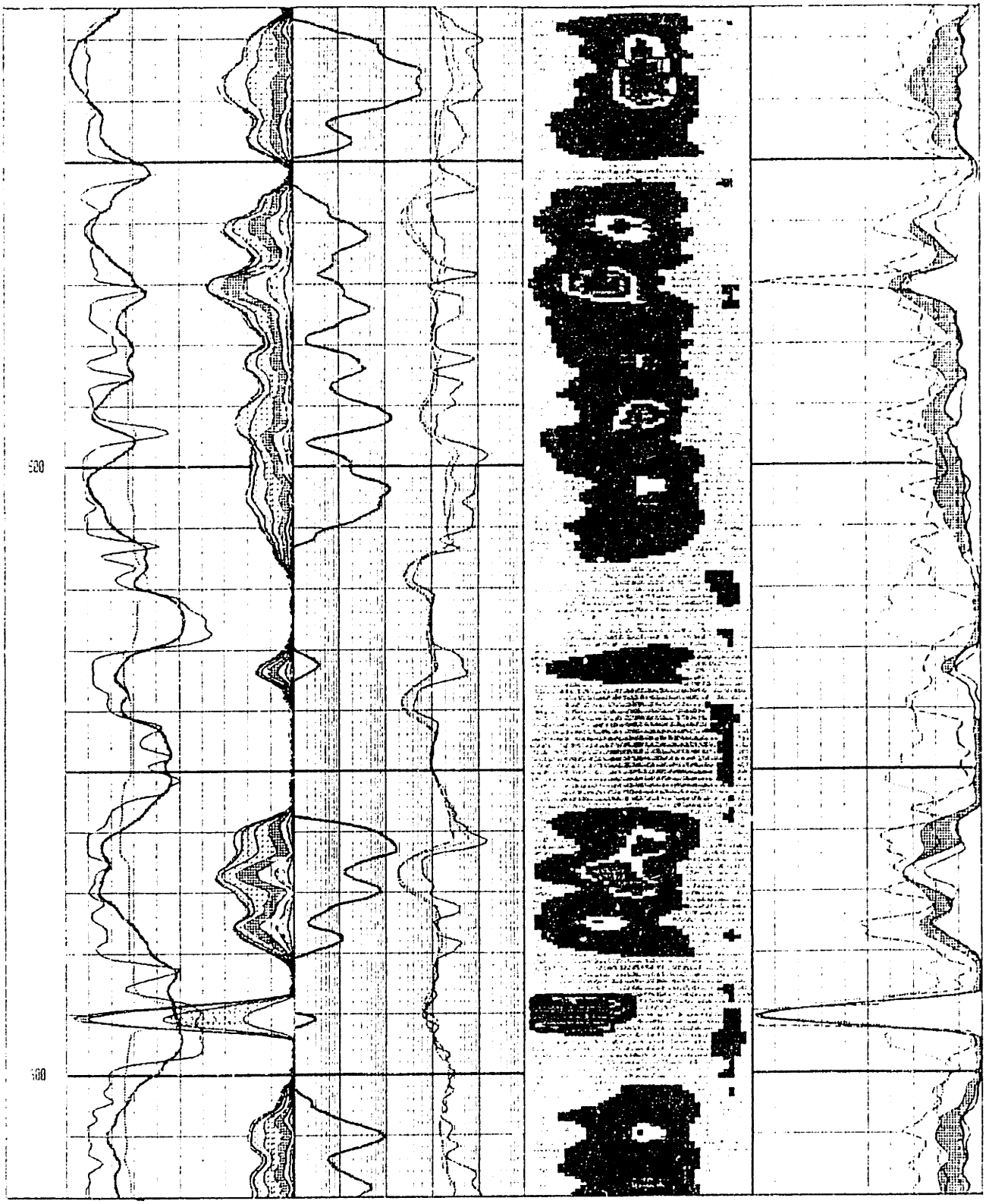

Figure 5.8 Example 2. The zone from X430 to X450 was conventional and produced about 0.5 BCF in a year and depleted. The zone was then stimulated along with the zones at X455 to X475 and X560 to X580. The latter two zones have low resistivity and appear wet but the bins show very small pores and high BVI. The interval after stimulation is still productive over 1 year later and will produce in excess of 1.5 BCF.

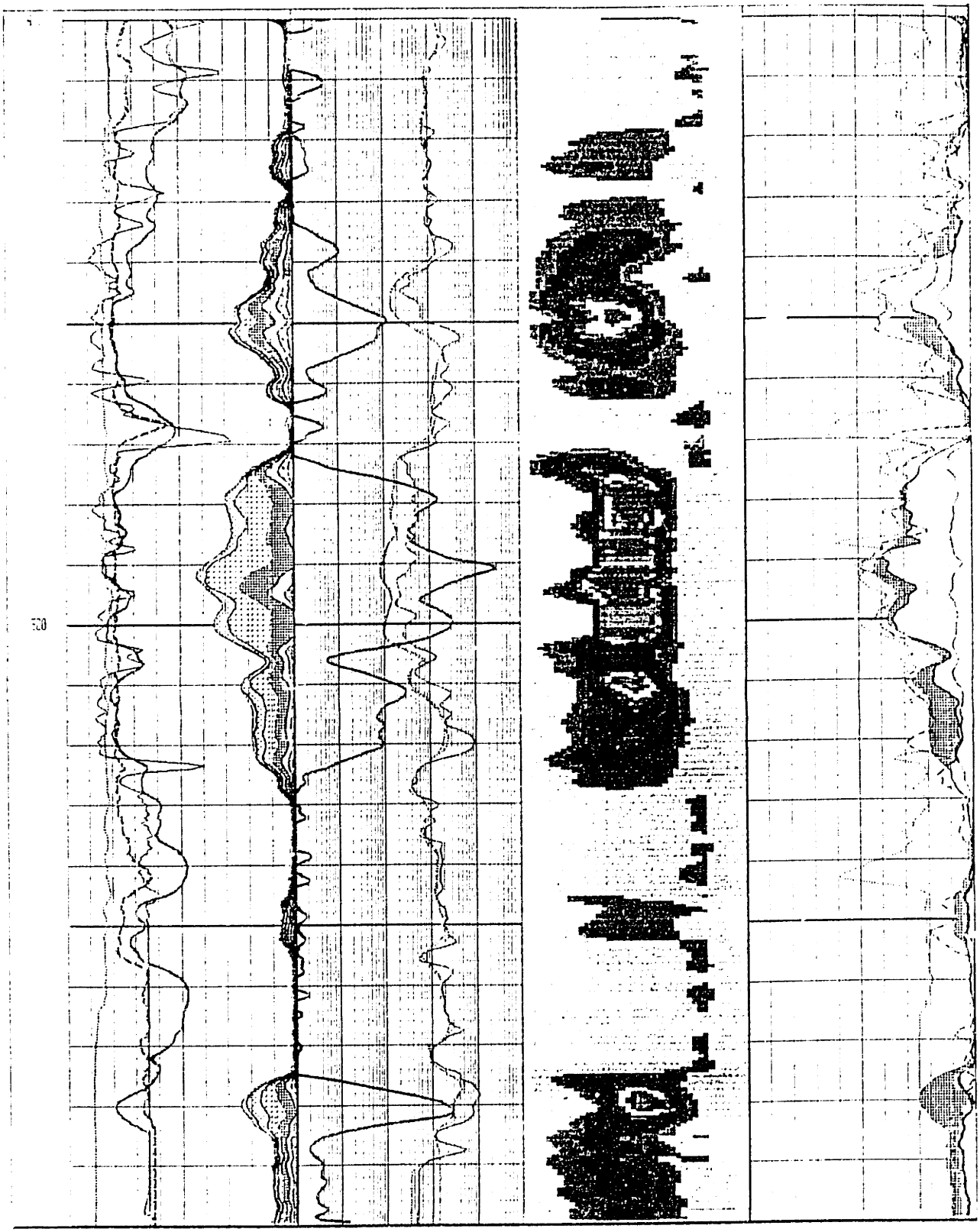

Figure 5.9 Example 3. The bottom zone from X575 to X585 was assumed nonproductive because of a minimal mud log show. It was perforated and flowed initially at 3 MMCFPD.

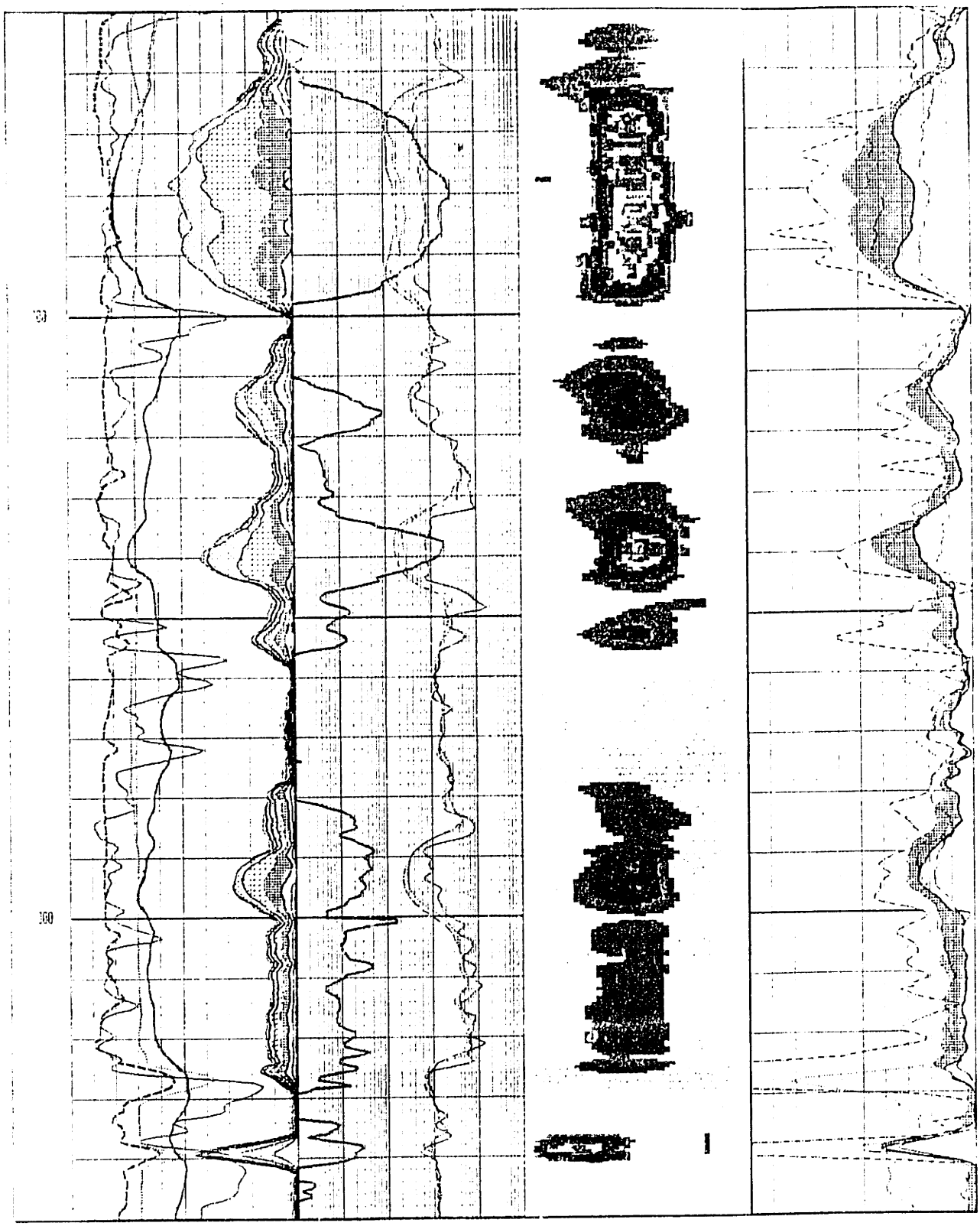

Figure 5.10 Example 4. The zones from X935 to X945 and X860 to X890 have a smectite coating and show very low resistivity. The high CEC of the clay caused dual-water to predict movable water. The zones produced at a high rate (initially over 3.5 MMCFPD) with no water. The bin distribution in track 1 (predominantly 4, 5, and 6) makes these zones detectable with NMR although they were thought to be wet.

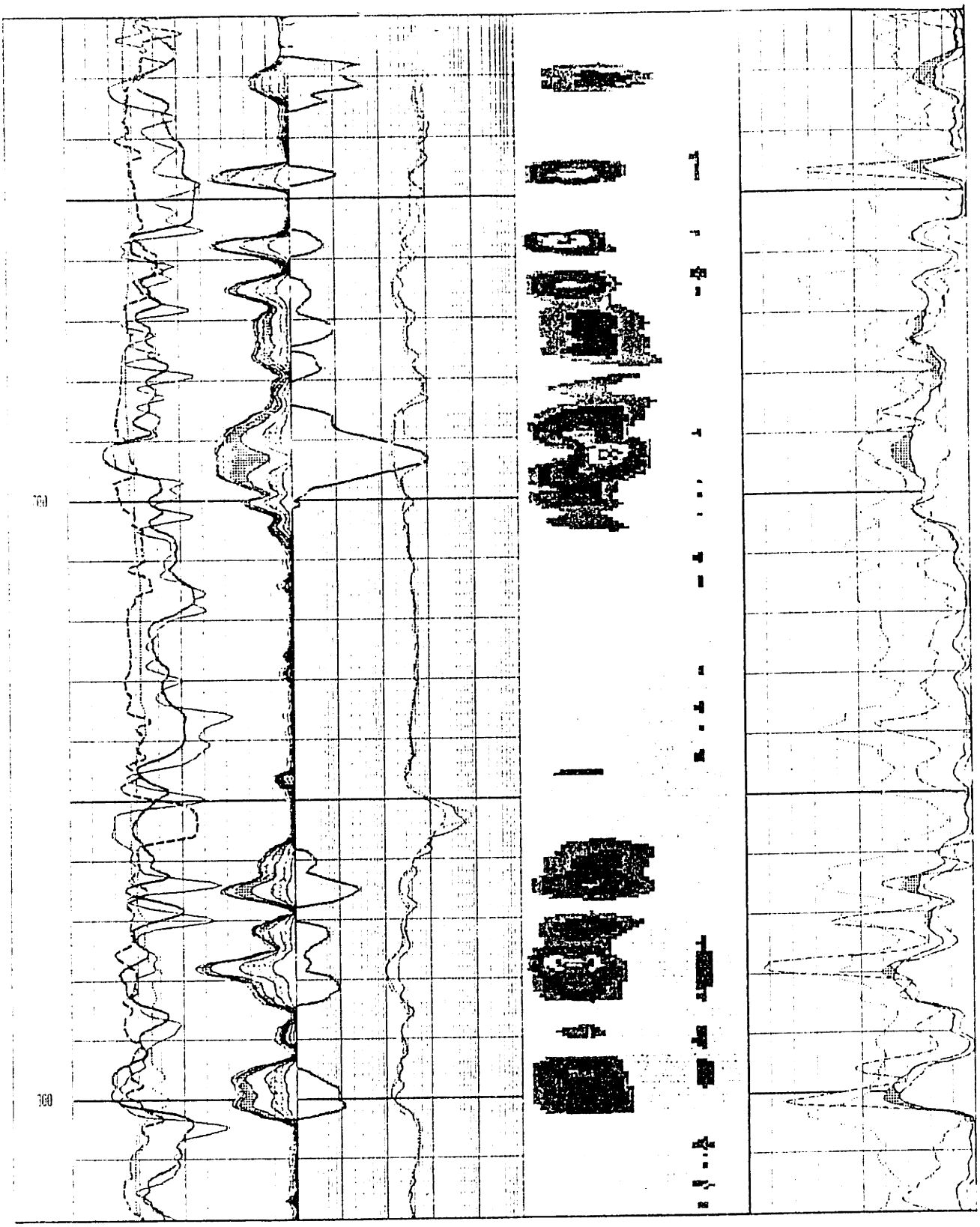

Figure 5.12 Example 6. The zones from X690 to X880 were thought to be wet from the resistivity logs showing about 1 ohm-m. The interval tested less than 20 MCFPD with no water. After stimulation, the interval has produced over 0.75 BCF with minimal water production. The bins show very small pores with extremely high BVI. The silty nature of these sands (demonstrated by the early bins) caused them, after stimulation, to produce gas or nothing. The capillary forces of the small pore structure inhibit the flow of water after stimulation.

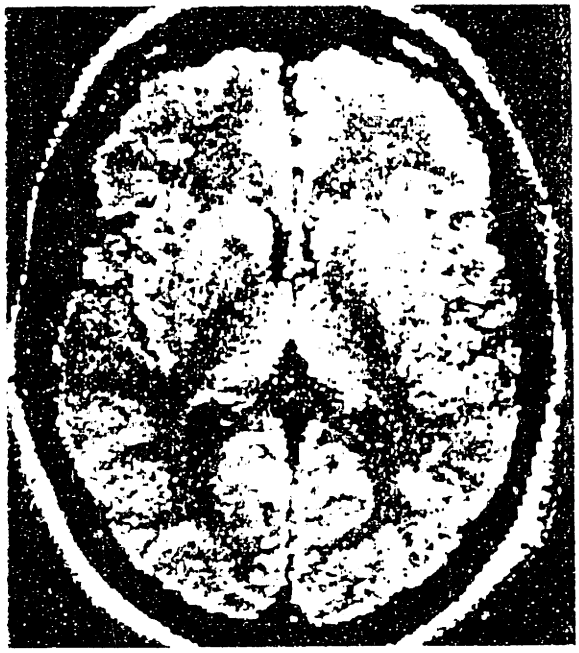

Figure 5.13 A spin density–weighted magnetic resonance image of the brain, with a 20% spin-density contrast between gray and white matter. From Bushong, 1996.

Figure 5.14 A T_1-weighted magnetic resonance image of the brain, with a 30% T_1 contrast between gray and white matter. This image provides the best resolution between gray and white matter because of the high T_1 contrast. From Bushong, 1996.

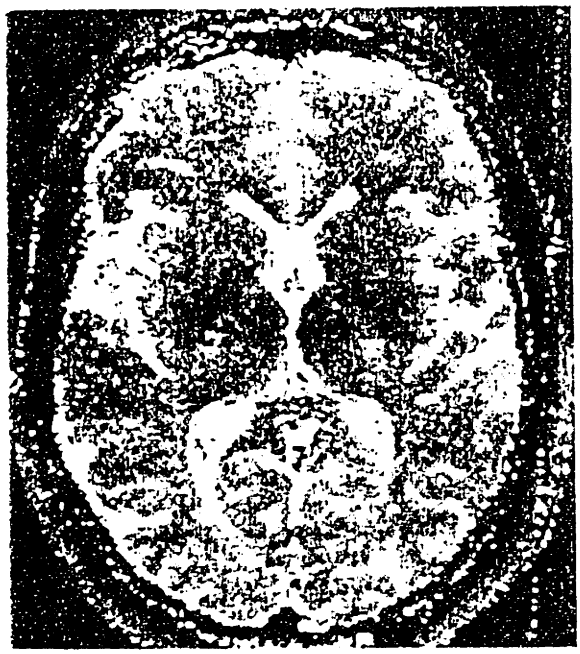

Figure 5.15 T_2 is about 100 ms for both gray and white matter. Thus, a T_2-weighted magnetic resonance image shows no contrast between gray and white matter. From Bushong, 1996.

Chapter 6

Hydrocarbon Imaging

This chapter addresses the direct detection of hydrocarbons using gradient-field pulsed NMR logs. The ability to image hydrocarbons directly with a continuous logging tool represents a major advance in well logging technology. The thesis research—how to use ideas from medical imaging (as described in Section 5.4) and the specific NMR properties of pore fluids to develop special pulse sequences to image these fluids—is presented. The thesis research represents an extension of the differential spectrum method, which was developed at Shell (Akkurt et al., 1995). Specific examples of gas imaging and novel interpretation methods are described after review of T_2 in a gradient magnetic field and in the occurrence of restricted diffusion, and of the differential spectrum method along with the modifications of T_1 weighting.

6.1 T_1 and T_2 Relaxation in a Gradient Magnetic Field

In section 4.2, it was shown how different T_E values could be used in the MRIL-C to measure the diffusion constant of pore fluids. To understand better the relaxation of fluids in porous media, it is worth reviewing the relaxation mechanisms in detail. Table 6.1 gives a summation of relaxations in porous media of interest. T_2 relaxation is best described as a sum of three terms:

$$\frac{1}{T_2} = \frac{1}{T_{2B}} + \frac{1}{T_{2S}} + \frac{1}{T_{2D}} \tag{6.1}$$

where T_{2B} is the bulk relaxivity, T_{2S} is the surface relaxivity, and T_{2D} is the T_2 for diffusion in a gradient magnetic field. It is important to note that T_{2B} and T_{2D} are independent of lithology. As reviewed in the previous chapter, T_{2S} can be stated in terms of the surface-to-volume ratio of the pore space:

$$\frac{1}{T_{2S}} = \rho_2 \frac{S}{V} \tag{6.2}$$

This is a function of the size of the pores and the surface relaxivity of the formation. The value of ρ_2 is different for sandstones and carbonates. Carbonates have a smaller relaxivity, so their T_2 distribution is shifted to the right. This term applies only to the water in the pores because it is the wetting fluid. The hydrocarbons do not have a surface relaxation term because they sit in the middle of the pores. This is also the case for water in vugs or large fractures.

For gas and light oil, the diffusion term T_{2D} will dominate the T_2 of Equation 6.1:

$$\frac{1}{T_{2D}} = \frac{(\gamma G T_E)^2 D}{12} \tag{6.3}$$

Because T_E = 1.2 ms and G = 17 gauss/cm for the MRIL-C, this term will dominate the T_2 relaxation only in the case of light oil and gas. Figure 6.1 shows the relation between T_{2D}, temperature, and pressure for methane in MRIL-C imaging (the imaging of interest here) and MRIL-B imaging.

T_1 for oil or gas is a bulk phenomenon and does not depend on surface or diffusion in a gradient field. Bulk process also dominates T_1 for water in vugs or fracturess. T_1 is a function of temperature and viscosity. The T_1 of methane gas is given as a function of temperature and pressure in Figure 6.2. It is seen that at 200 °F and 4000 psi with the MRIL-C, T_1 is 4 s. At the same temperature and pressure in Figure 6.1, T_{2D} is 35 ms. For

oil, 30° F API and 1 centipoise (cp), T_1 is 1.1 s and T_2 is 0.9 s when T_E is 1.2 ms. These examples show that T_1 and T_2 of gas are related to completely different mechanisms. The T_2 for gas is wholly related to diffusion, whereas the T_2 for oil is a function of both bulk and diffusion, relaxation mechanisms.

Thus, a number of mechanisms control the T_1 and T_2 relaxation of fluids in reservoirs. Also, the fluids differ in T_1 and T_2 and in the relaxation mechanisms that dominate the overall relaxation of the fluids. Making the T_E larger in Equation 6.3 can enhance the effect of T_{2D}. This means that the CPMG pulse sequence can be T_2 weighted by increasing the interecho spacing (T_E). By manipulating the pulse sequences, the differences in fluids can be enhanced, enabling direct imaging of the fluids. This, in many ways, is analogous to the way in which contrast between gray and white matter in the brain is obtained (see Chapter 5).

6.2 Differential Spectrum Method

To understand how best to distinguish pore fluids using NMR logs, the physics of the NMR measurement should be reviewed. T_1 (the longitudinal relaxation) is the exponential increase in the net magnetization of the sample in the M_0 direction (parallel to the external magnetic field B_0). After the spins have lined up through T_1, they are tipped 90° by the RF pulse into the transverse plane and the magnetization M_{xy} in the transverse plane (the plane perpendicular to the constant magnetic field B_0) begins to decay at T_2. The pulse echoes (after the RF tipping pulse) are created so that the true T_2 decay can be measured and the magnetization does not all decay away through free induction decay at a rate T_2*. The concept that is implied but not stated is that T_2 must follow T_1. The protons cannot be tipped into the transverse plane until they have first been aligned with B_0. Therefore, partial recovery of T_1 of a species will lead to the measurement of T_2 for only those spins that have had time to be polarized. It is the idea of partial recovery of some of the spins by T_1 weighting that leads to the differential spectrum and gas-imaging NMR concepts.

The differential spectrum method requires that the data be acquired at two separate wait times, T_L (T long wait time) and T_S (T short wait time). The T_L should be roughly $T_L > 3\ T_1$ g (gas) such that 96% of the gas is recovered. In the second pass, $T_S > 3\ T_1$ (water maximum); the wait time is chosen so that 96% or more of the water is recovered. The net magnetization recovered is given by the equation (2.17) in section 2.4.1:

$$M(t)_Z = M_0\ (1 - e^{-t/T_1}) \tag{6.4}$$

Plugging in $3T_1$ for t yields $M_Z = 96\%\ M_0$. The differential spectrum concept is illustrated in Figure 6.3, where the T_2 distribution is shown for both passes. In the T_S pass, all the water (which is shown in gray) is recovered; it is distributed from bins 1 to 8. The gas (vertical striped) is located in bins 4 to 6. However, only a portion of the gas has been recovered because of the greater T_1 for gas. The T_L pass shows the same distribution for water, but, with maximal gas recovery, a significantly increased amount of gas in the distribution. The last step is to subtract the two curves bin by bin from each other, arriving at the distribution that is only gas.

The same method can be used for oil (Figure 6.4) provided the T_1 for oil is larger than that of water in the highest bin. This method should work as long as the oil viscosity is less than 1 cp (Figure 6.5). The figure shows T_1 as a function of viscosity as well as T_2 (for a tool gradient of 20 gauss/cm) as a function of viscosity in cp. For oil of 0.5 cp, this gives a T_1 of 2.5 s and a T_2 of 1 s for a $T_E = 1$ ms. This means with $T_S = 1$ s, only 33% of the oil is recovered, but with $T_L = 8$ s, 96% of the oil is recovered. This is also optimal because T_2 from the oil is 1 s so it falls in the ninth bin. Gas is normally found in the fourth, fifth, and/or sixth bins.

The width of the T_2 spectrum of the gas is also relevant. This width is determined by T_{2D} as well as restricted and unrestricted diffusion of methane in porous media. For unrestricted diffusion, Equation 6.3 shows that T_{2D} is a function of the molecular diffusion constant D as well as the parameters set by the tool T_E and G. For the MRIL-C, T_{2D} for

methane is given in Figure 6.1. The figure shows that for gas at 3800 psi and 250 °F, T_{2D} = 30 ms. This would show up in the differential as the middle of the fourth bin. This is independent of the formation and represents the left-hand edge of the differential T_2 spectrum of the gas. The right edge of the distribution depends on restricted diffusion, which is a function of the formation that contains the gas.

The diffusion constant decreases in porous media because the surfaces of the pores restrict the motion of the molecules. For times that are short, as shown in Figure 6.6, regarding the apparent diffusion constant D(t):

$$\frac{D(t)}{D_0} = 1 - \left(\frac{4}{9\sqrt{\pi}} \frac{S}{V} \sqrt{D_0 t} \right) \tag{6.5}$$

where S/V is the surface-to-volume ratio, which, as has been shown above, is related to pore size, and $\sqrt{D_0 t}$ is the thickness of the surface layer of the pore walls. This says that the apparent diffusion constant will decrease linearly with pore size. This implies that small pores lead to a smaller apparent diffusion constant. Plugging into T_{2D}:

$$T_{2D(t)} = \frac{12}{(\gamma G T_E)^2 D(t)} \tag{6.6}$$

This would cause $T_{2D(t)}$ to increase and would cause the T_2 of the differential to widen. Using the above example in which T_{2D} = 35 ms and D(t) = ½ D_0, then $T_{2D(t)}$ equals 70 ms, or bin 5. The differential for the example would show gas in bins 4 and 5.

It can be shown that as t increases, the molecules start to diffuse from one pore to the next. In this case (Coates et al., 1993), D(t) is shown to be

$$\frac{D(t)}{D_0} = \frac{1}{\Gamma} = \frac{1}{F\phi} \tag{6.7}$$

where Γ is the tortuosity, F is Archie's formation factor, and ϕ is the porosity. The more tortuous the path, the more restricted the diffusion. If $F = 1/\phi^2$,

$$D(t) = D_0 \phi \tag{6.8}$$

If in the example above, $\phi = 10\%$, then $T_{2D(t)} = 10\ T_{2D}$, which is 350 ms, or bin 7, and the differential would be from bins 4 to 7 in this highly restricted case.

In actual logging applications, it is difficult to know the amount of restricted diffusion, so the calculations above should be used as a qualitative guide when interpreting the data. In low-porosity, tight sands, porosities are low, so the signal-to-noise ratio may be low; this translates into an often noisy differential spectrum. Knowing where the hydrocarbons can and cannot be is a very powerful tool that can be applied to interpreting noisy differential spectrum data.

6.3 Gas Imaging with T_1 Weighting

To adapt the differential spectrum method to maximally image the gas, it is imperative to examine the principles of the method. There is no T_2 contrast between water and gas because they both show up in bins 4 through 7. The differential spectrum method works because of the large contrast in T_1 between gas and water. The T_1 for water (even in the largest pores in sandstone) is approximately 600 ms, whereas the T_1 for a gas is between 3 and 5 seconds. As noted above, the T_S (or fast pass) is designed to recover all the water but only a minimum amount of gas. The T_L (or slow pass) is designed to recover all the gas and the water.

The signal in the differential spectrum of gas is proportional to the amount of gas recovered on the slow pass minus that recovered on the fast pass:

$$\Delta S = \left(1 - e^{-T_L/T_{1g}}\right) - \left(1 - e^{-T_S/T_{1g}}\right) = \left(e^{T_S/T_{1g}} - e^{-T_L/T_{1g}}\right) \qquad (6.9)$$

The nature of the exponential is such that ΔS is maximized by T_1 weighting or making T_S as short as possible. This, however, will not meet the constraint of the differential spectrum method that $T_S > 3T_1$ water maximum. This is the rule because one does not want to underrecover water and then see it on the differential and think it is gas. The constraint, however, is not crucial; Table 5.1 shows that with T_W = 1 s, recovery is 93% in bin 7 and 73% in bin 8. This means if water is not underrecovered by using T_S = 1 s, it will show up in bin 8. This is not a problem because gas, even in the most restricted case, will not be in bin 8. Therefore, anything that shows up in bin 8 in the differential spectrum must be under-recovered water or noise. Also, as seen in the examples of Chapter 5, in tight sands there is little if any porosity in bin 8 and only slight amounts in bin 7.

The Table 5.1 shows that even with a wait time of 0.75 s, the first six bins are fully recovered and any porosity in bins 7 and 8 in the differential would be easy to differentiate from a gas signal. The duty cycle of the present MRIL-C technology is limited to 1-s wait times in dual-frequency mode. This means for most sands with gas, a T_S = 1 s and a T_L = 2 T_1 g will give an optimum value for ΔS. An example would be to examine a sand with bins 7 and 8 and gas with a T_1 of 4 s. Using T_S and T_L of 1 and 8, respectively, ΔS = 64% with 73% recovery in bin 8. Using a 2, 12 on the same rock, ΔS = 56% with 98% recovery in bin 8. The T_1-weighted case is far superior because the logging speed is much greater and ΔS is much larger. The only drawback is a 15% underrecovery of water in bin 8, which would be easy to interpret.

Thus, gas effect in NMR is due to not waiting long enough for the gas to recover and thereby missing porosity from the T_2 spectrum. A second, and equally important, type

of gas effect is due to the hydrogen index. Figure 6.7 shows the hydrogen index as a function of temperature and pressure of the gas. For a gas at 250 °F and 4000 psi, the hydrogen index is 0.33. This means that only 1 pu will be detected for every 3 pu of gas-filled porosity. This implies that small amounts of gas detected in the differential could represent significant amounts of gas-filled porosity when the hydrogen index of the gas is considered. In certain tight-gas sands—such as the Bossier sand, which is highly charged with gas—NMR logs miss a considerable amount of porosity. This outcome is not due to underrecovery from short wait times, nor is it due to clay-bound porosity or microporosity; it is simply a hydrogen index effect.

Another way to detect gas is to assess the partial porosity and the rate of change as the wait time is changed. Table 6.2 shows the amount of porosity recovered if T_1 = 350, 500, or 750 ms for water or T_1=3 or 4 s for gas. For the least contrasting cases of water at T_1 = 750 ms and gas at T_1 = 3000 ms, the increase in porosity is similar for a change in wait time from 1 to 1.5 s. The contrast is greater for the change from 2 to 3 s; gas recovery increases by 14%, but water recovery increases by only 5%. This difference is made even clearer by the fact that the increase in the water porosity should be up in bins 7 and 8 when the gas is increasing in bins 4 and 5. The difference is even more evident between 3 and 8 s: the water increases very little, while the gas increases by 30%. By acquiring the data at multiple wait times, this analysis makes it apparent when the bins are increasing, whether the increases are due to gas, water, or noise.

6.4 Nuclear Magnetic Resonance Gas Imaging Log Examples and Interpretation

The first example log (Figure 6.8) shows the standard display of the differential spectrum data. Tracks 1, 2, and 4 are the same as in the earlier log sample, that is, Figure 5.1. For the bin display in track 1, the bins from one of the short-T_W passes are used. A short-T_W pass provides improved representation of pore size because it is T_1 weighted, with little gas recovery in the T_2 distribution. Track 3 is a color display of the bin-by-bin

differences in the two passes T_L and T_S. (The examples here are reproduced only in black and white.) The track has nine equal divisions, with bin 1 on the left and bin 9 on the right. As the value for the bin increases, the color grows hotter. As was described in the previous section, it is the location of the differential that is most important in the interpretation, not the absolute amount of gas detected. In the examples that follow, it can be seen that in some cases this information strengthens the interpretation and in others it clarifies ambiguous or conflicting data. As with other direct hydrocarbon detection techniques, the data are compelling. Their descriptions represent a breakthrough in well logging, enabling logging, in a continuous fashion, of large intervals and the location of zones that were not known or a priori.

Example 1 (Figure 6.8) is a repeat of Figure 5.10 except for the change to differential spectrum data in track 3. The first step is to estimate T_{2D} from the graph in Figure 6.1 (solid lines, for MRIL-C), which is about 40 ms, which is between bins 4 and 5 (see Table 3.1). In the log zone from X860 to X900, there is a good deal of gas from bin 4 to bin 6. The first part, from X860 to X866, is probably artifact because the location is a very low porosity edge, with the difference due to noise between the fast and slow pass. From X866 to X874, gas is in bin 6, shifting to bin 5 from X874 to X876. All of this makes sense because in track 1 the pore size increases in the bottom of the zone and decreases at the top. At the top, the zone has more bin 5 and less bin 6; in the lower part, it has less bin 5 and more bin 6 and some bin 7. As pore size gets smaller, diffusion is expected to become more restricted, which moves the differential to the right.

At many points up and down the log, there is an artifact in bin 8, ending abruptly at the bin's limit; see, for example, X900, X904, X922, and X978 to X986. This artifact is not water in the eighth bin but is due to rectified noise in the latter part of the echo train that is inverted into bin 8 of the T_L pass. The work of Edwards and Chen (Edwards and Chen, 1996) at Atlas Wireline provides a way of filtering these data to obtain a better inversion (Edwards, 1996).

There is a gas zone at X932 to X946; however, the differential also shows gas at X946 to X950, which is artifact below the true gas zone due to low porosity and a low signal-to-noise ratio in the tight zone. The pore size distribution and the less restricted gas effect point to X932 to X946 as having streaks of better permeability than the one above it (X860 to X900), even though it is not as thick. Testing and production of the zones proved this to be correct.

The zone from X990 to X998 shows gas from X994 to X998. The lower porosities and smaller pore sizes lead one to suspect that this zone will need stimulation to contribute but is still productive. The demonstrated productivity of these zones after stimulation suggests this to be a sound estimation.

Example 2 (Figure 6.9) has a sand that looks prolific from X164 to X178. The gas and the resistivity look similar to the top zone in the previous example. The distribution in track 1 shows that the low resistivity is due to smectite and illite, as in the previous example, so there is little recovery of movable water. The interpretation might suggest that after stimulation, this zone would be as productive as in Example 1. The problem with this zone is permeability. The top part of the zone is clearly very shaley because it is mostly bin 4. As the zone gets deeper, the porosity starts to drop; near the bottom, it becomes very tight. This zone was stimulated but never produced more than 700 MCFPD; although there was gas, the reservoir was limited away from the wellbore. Interpretation could have been improved in this example; closer examination of the zone shows the gas and best porosity to exist in only a 6-ft interval.

Example 3 (Figure 6.10) has a low signal-to-noise ratio and a good deal of artifact in both the early and late bins. The upper zone from X452 to X456 would have been suspected as wet from the dual-water model. The zone had a 20-unit gas show but did nothing in the drill stem test. The bins in the first track show that the zone is a siltstone because of the large amount of bin 4. The gas is in bin 6 but it should be in bin 4, so it is highly restricted, as would be expected in a siltstone. Zone X470 to X480 is a gas-filled

sand even though it has low porosity. The gas in the bins 6 and 7 show it as restricted, but the pore size shows that there are some larger grains even though the zone will need stimulation. Because this zone has been recognized, stimulation can be performed without worry about breaking into water.

The bottom zone from X620 to X628 is an excellent example of why the use of NMR logs is important. Despite an excellent (100+) unit show for the well, the zone was not tested because so many zones above it had been tested. The gas is in bins 4 and 5, not restricted like the zones above, so the permeability is excellent. The bin distribution in track 1 shows this to be a smectite zone, with a full 8 ft of non-restricted, preserved permeability. Since nearby zones are also gas filled, upon stimulation the entire interval should be the most prolific in the well. This example shows zones from top to bottom to have resistivity between 1 and 2 ohm-m, which conventional log analysis would have judged wet.

Example 4 (Figure 6.11) is a repeat of Figure 5.12 except for the differential, which confirms the analysis. Even though drill stem testing showed only 20 MCFPD for the entire 200-ft interval, the interval has done very well after stimulation. Because of the higher amounts of BVI in this type of rock, there is a good deal of artifact in both the early bins and bin 8. Despite minimal shows on the mud log, there is gas showing up in all the sands between X680 and X700, as well as between X760 and X800. Considering the high BVI in these zones, a large amount of invasion of filtrate would be expected, which makes it surprising to see some gas at 4 inches. into the formation. Looking at the neutron density in many of the zones shows that NMR is missing quite a bit of the porosity. Some of the missed porosity is clay, but more than half is gas effect due to the hydrogen index.

In Example 5 (Figure 6.12), zone X326 to X338 is a conventional zone that has good possibilities. This zone has resistivity and a pore size distribution indicating it to be productive. The zone shows gas in bin 4 with little restricted diffusion. Even though the zone had only a 28-unit gas show and 8 pu of effective porosity, the NMR analysis points to the zone's being productive in spite of the porosity and thickness of the zone. The zone

drill stem tested at 950 MCFPD.

Example 6 (Figure 6.13) is a very prolific interval of gas-charged zones from X900 to X070. There is a strong gas signal in about every zone, translating to a 20-unit or better show for almost every blip of porosity. The striking thing is that the effective porosity is consistently below 6% effective MPHI. The first 3 bins show a good deal of artifact; the signal is so low (because of low porosity) that there is a good deal of noise in the BVI measurement. Although the porosities are low, the permeability is in the 1-md range. Notice that there are large pores in zone X015 to X025, with porosity in bins 7 and 8. Comparing the MPHI with the neutron–density cross-plot reveals that as much as 4 pu is missing in many zones. This missed porosity is not due to clay-bound porosity and is, therefore, due to gas effect from the hydrogen index. It is remarkable that zones this tight have this much gas in the invaded zone at 3 inches. into the formation. The entire interval was stimulated and has produced more than 0.75 BCF in 18 months, with a 1.5 MMCFPD initial production.

Example 6 shows that many accepted models of invasion must be modified. A low-frequency version of the MRIL-C looks deeper into the formation, by 1 inch. Looking 1 inch deeper, or 4 inches into the formation, the amount of additional gas is astonishing. As the signal-to-noise ratio of the tool improves, in the future, we shall be able to quantify the amount of gas in the pore space as a function of the depth of investigation. Qualitatively, the fact that the method of gas imaging works as well as it does means that more gas migrated back to the borehole after the invasion of filtrate by drilling with fresh mud.

The seventh and final example (Figure 6.14) shows a clear case of underrecovered water in bin 8. In zone X215 to X227, it can be seen from the bins at the left that there was no eighth bin in the T_S pass; the bins on the T_L pass, however, had in excess of 1.5 pu of gas. In addition, an intermediate pass showed bins 7 and 8 to be growing. This was clearly a zone with large pores and movable water. The zones above it show quite a bit of artifact, but there is definitely gas signal in bins 4, 5, and 6 as well. The zones from X060 to X120

show gas and smaller pore size than the lower zones. The upper zone from X060 to X070 showed little, if any, bin 7 or 8 on the long pass and does show gas in bin 5 of the differential. The interpretation indicates that stimulating the upper zone could probably be undertaken without making much water. Zone X215 to X227 was perforated and it flowed saltwater. Zone X060 to X070 was perforated and it flowed gas and no water.

Table 6.1 Relaxation Mechanisms

		T_1	T_2	T_1/T_2
Mineral Hydrogen		10-100 s	10-100 μs	$\sim 10^6$
Water	Clastic	Surface Dominated	Surface Dominated	$T_1/T_2 = \xi$ $\xi \sim 1.5$
	Vugs	Bulk*	Bulk/ Diffusion*	$T_1 \geq T_2$
Oil	Medium to Heavy	Bulk*	Bulk*	$T_1 = T_2$
	Light	Bulk*	Bulk/ Diffusion*	$T_1 \geq T_2$
Gas		Bulk*	Diffusion*	$T_1 \gg T_2$

(*)Independent of formation. Consult appropriate chart.

From Kleinberg and Vinegar, 1996.

Table 6.2 Rate of Recovery according to T_1 vs. Wait Time (T_W)

		Wait Time (T_W) in seconds				
T_1 (seconds)		1	1.5	2	3	8
Water	0.350	94.3%	98.6%	99.7%	100.0%	100.0%
	0.500	86.5%	95.0%	98.2%	99.8%	100.0%
	0.750	73.6%	86.5%	93.1%	98.2%	100.0%
Gas	3.000	28.3%	39.3%	48.7%	63.2%	93.1%
	4.000	22.1%	31.3%	39.3%	52.8%	86.5%

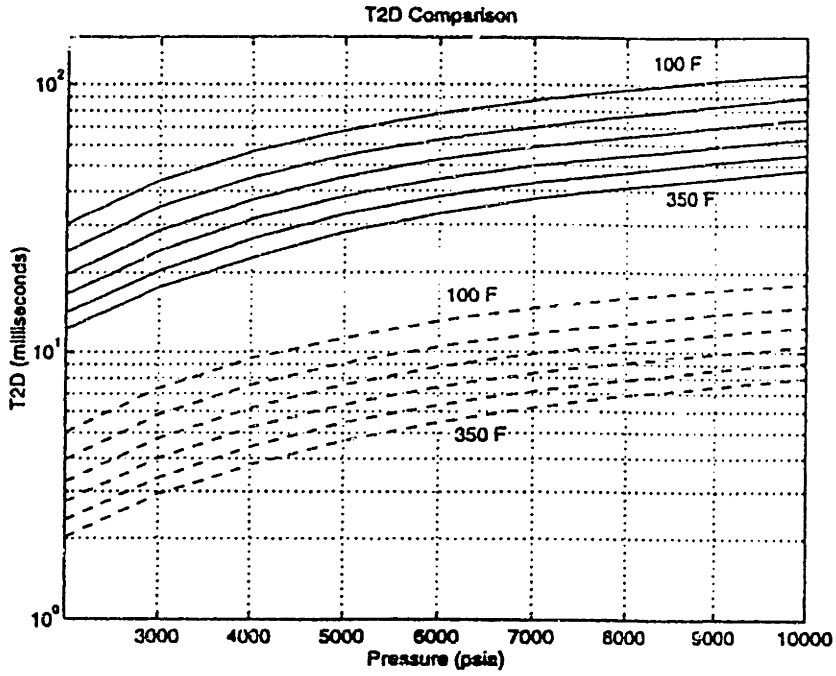

Figure 6.1 T_{2D} of methane, as a function of pressure and temperature given in 50° F increments. The curves for the MRIL-B (dashed) and MRIL-C (solid) are different. The MRIL-C has G = 17 gauss/cm and T_E = 1.2 ms while the MRIL-B has G = 25 gauss/cm and T_E = 2 ms. From Akkurt et al., 1995.

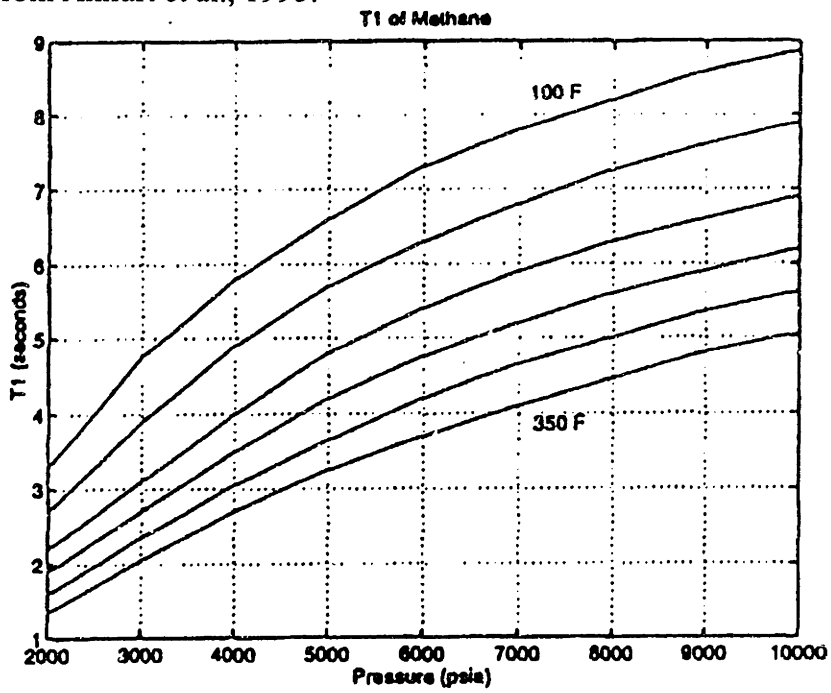

Figure 6.2 T_1 of methane, as a function of pressure and temperature given in 50° F increments. From Akkurt et al., 1995.

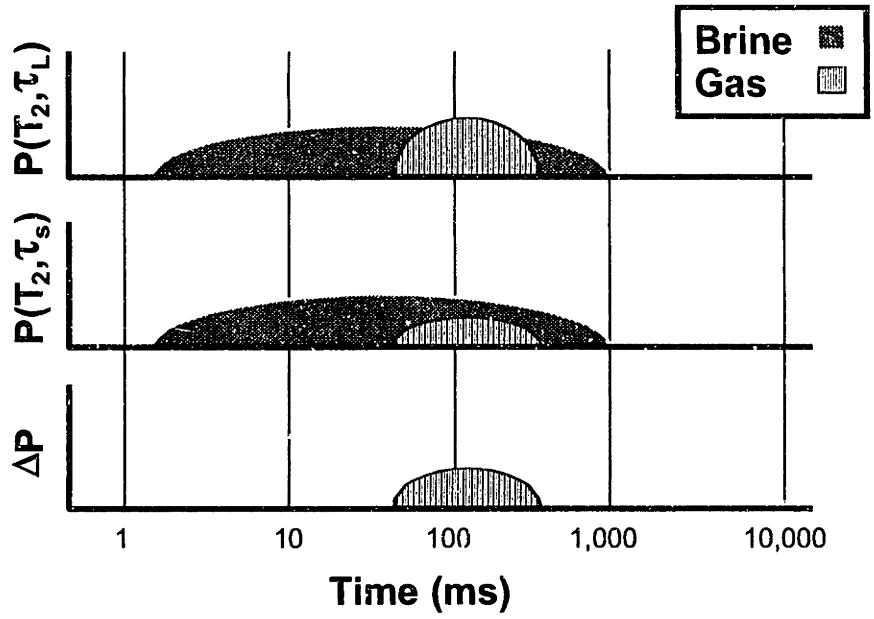

Figure 6.3 NMR differential spectrum between gas and water. The fast pass (T_S, short wait time) recovers all the water (shown in gray) and some of the gas (vertical stripe). The slow pass (T_L, long wait time) recovers all the water and almost all of the gas. The difference (ΔP) should be all gas signal. Adapted from Akkurt et al., 1995, and Cherry, 1995.

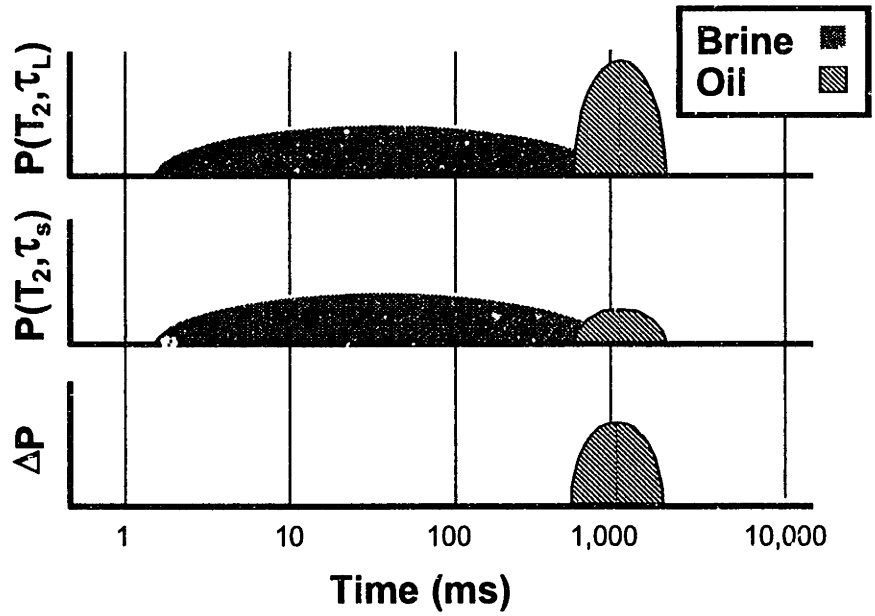

Figure 6.4 NMR differential spectrum between oil and water. The fast pass (T_S, short wait time) recovers all of the water (shown in gray) and some of the oil (diagonal stripe). The slow pass (T_L, long wait time) recovers all the water and almost all of the oil. The difference (ΔP) should be all oil signal. Adapted from Akkurt et al., 1995, and Cherry, 1995.

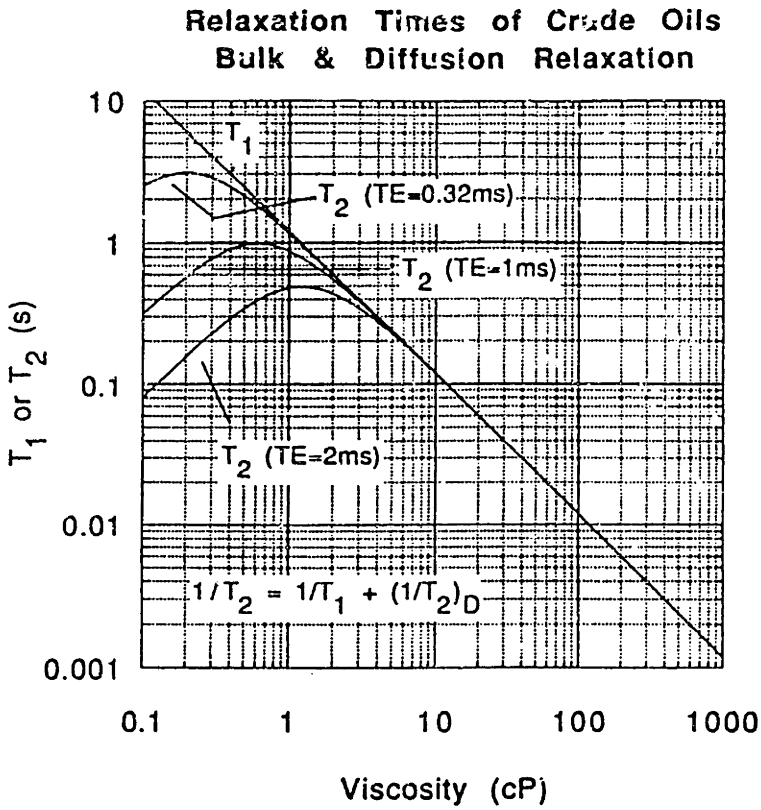

Figure 6.5 The T_1 relaxation of crude oils as a function of viscosity. The T_2 relaxation of crude oils as a function of viscosity and T_E for a logging tool with a magnetic field gradient G = 20 gauss/cm. From Kleinberg and Vinegar, 1996.

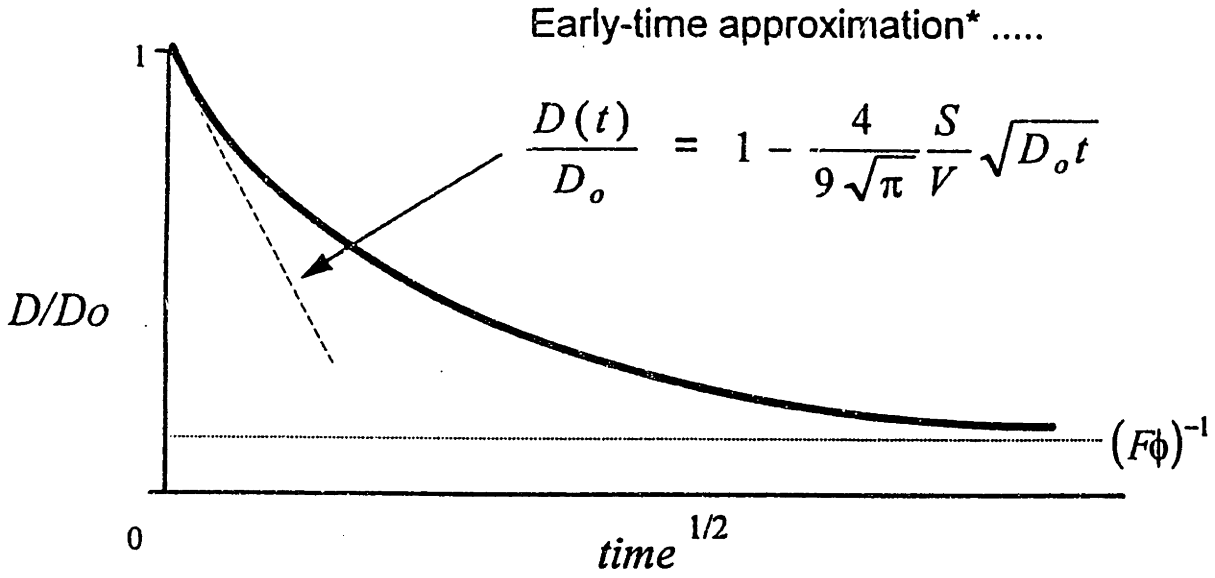

Figure 6.6 The apparent diffusion constant D(t) decreases linearly with pore size in the early-time approximation. From Mitra et al., 1992.

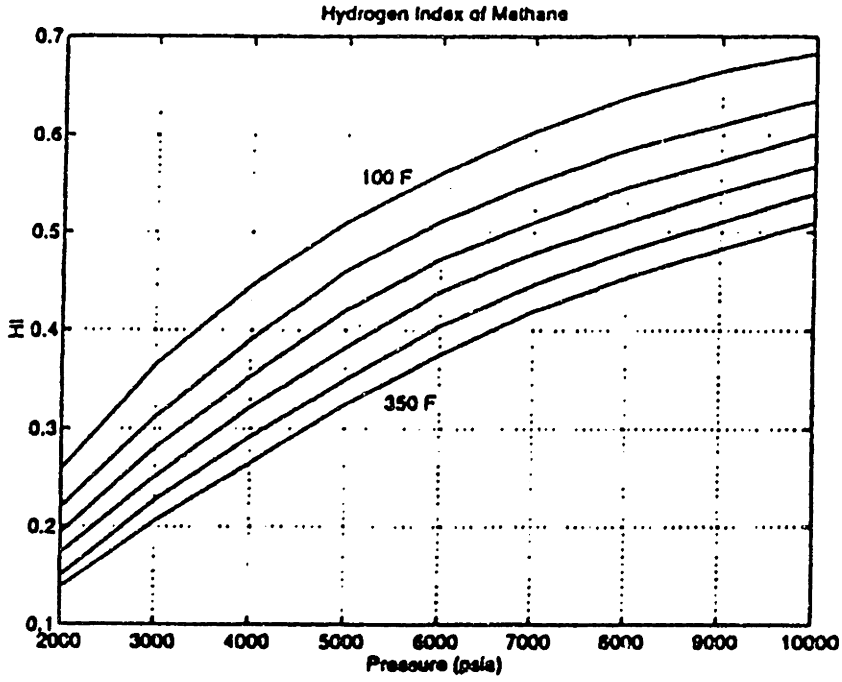

Figure 6.7 The hydrogen index of methane as a function of pressure and temperature given in 50° F increments. From Akkurt et al., 1995.

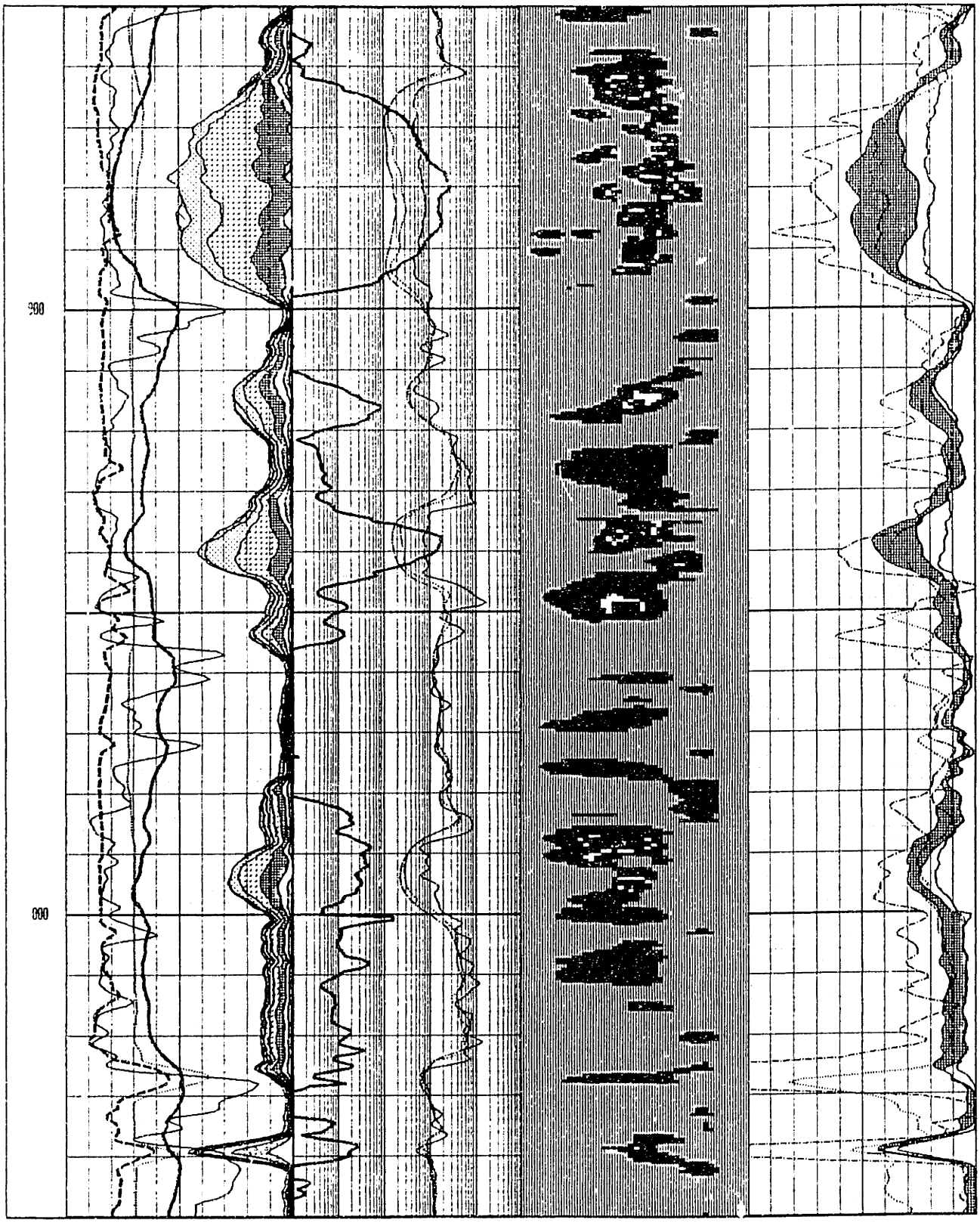

Figure 6.8 This first example is a repeat of the log in Figure 5.10 but with the gas signal (differential spectrum) displayed in track 3. The signal is shifted slightly to the right in the top zone at X862 relative to the second zone at X948. This means the diffusion is restricted and the permeability is less. This is in agreement with the ratio of bin 5 to bin 6 in the two zones.

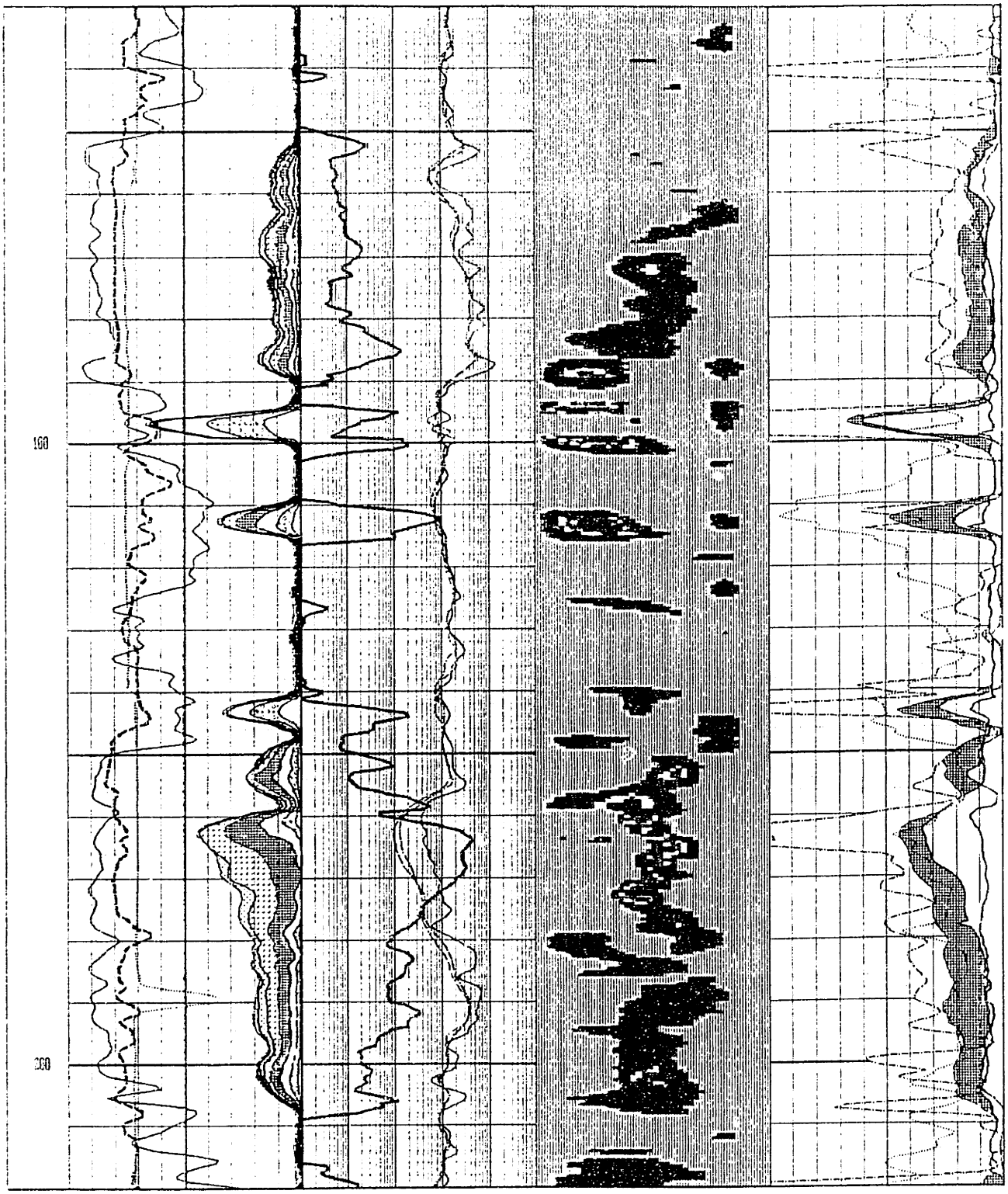

Figure 6.9 Example 2. The zone at X160 to X180 has a strong gas signal, and the bins as well as the resistivity indicate the presence of smectite. The poor performance of the zone after fracturing can be explained by the predominance of bin 4, indicating small pore structures with a large amount of clay.

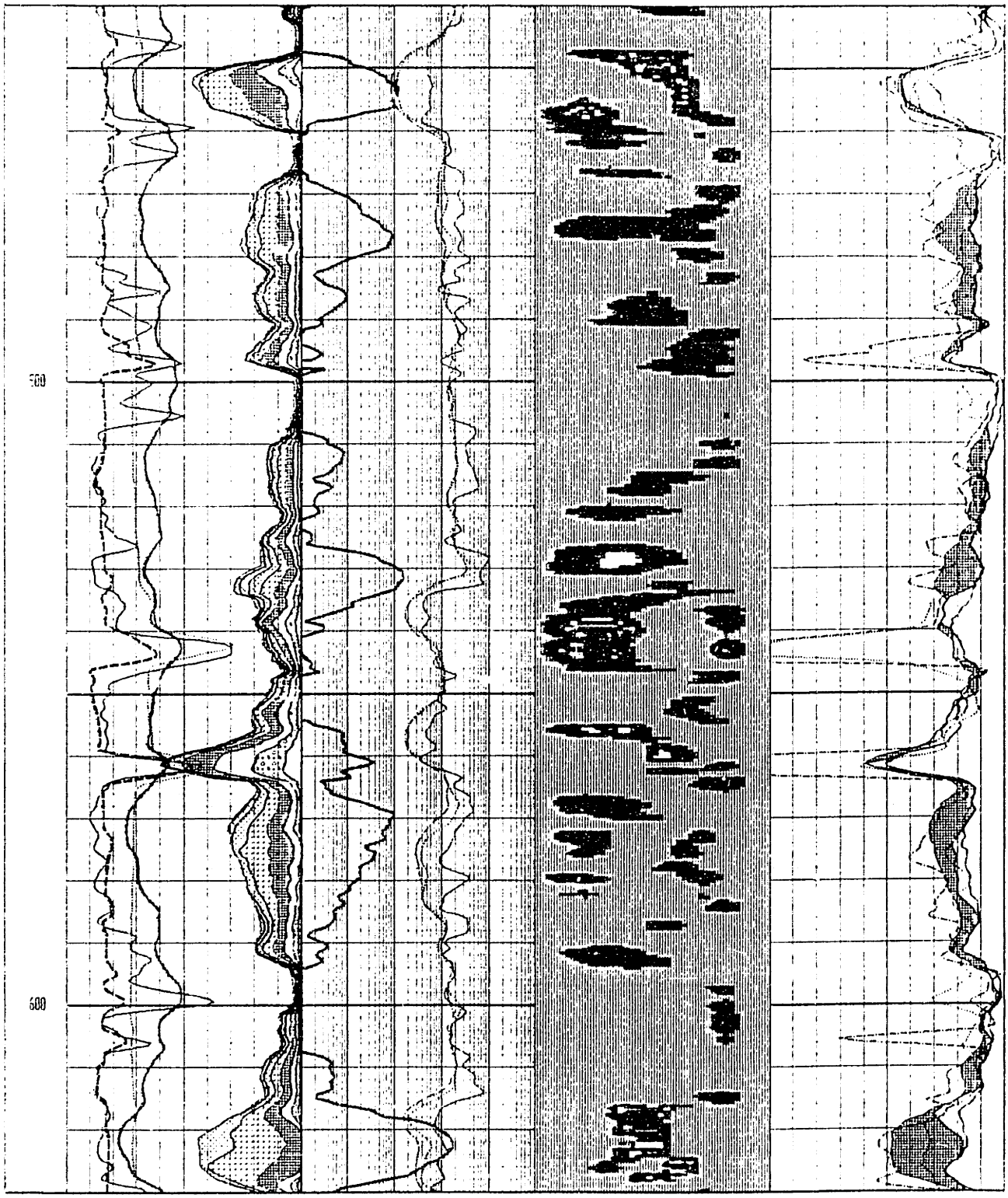

Figure 6.10 Example 3. Zone X615 to X628 has a strong, unrestricted gas signal. The bins once again predict clay coatings. The zone could be the most productive in a very prolific well and is still behind pipe. Zone X450 to X460 is conventionally wet, but the bins (mostly 4 and 5) show it is a siltstone. Drill stem testing verified this interpretation.

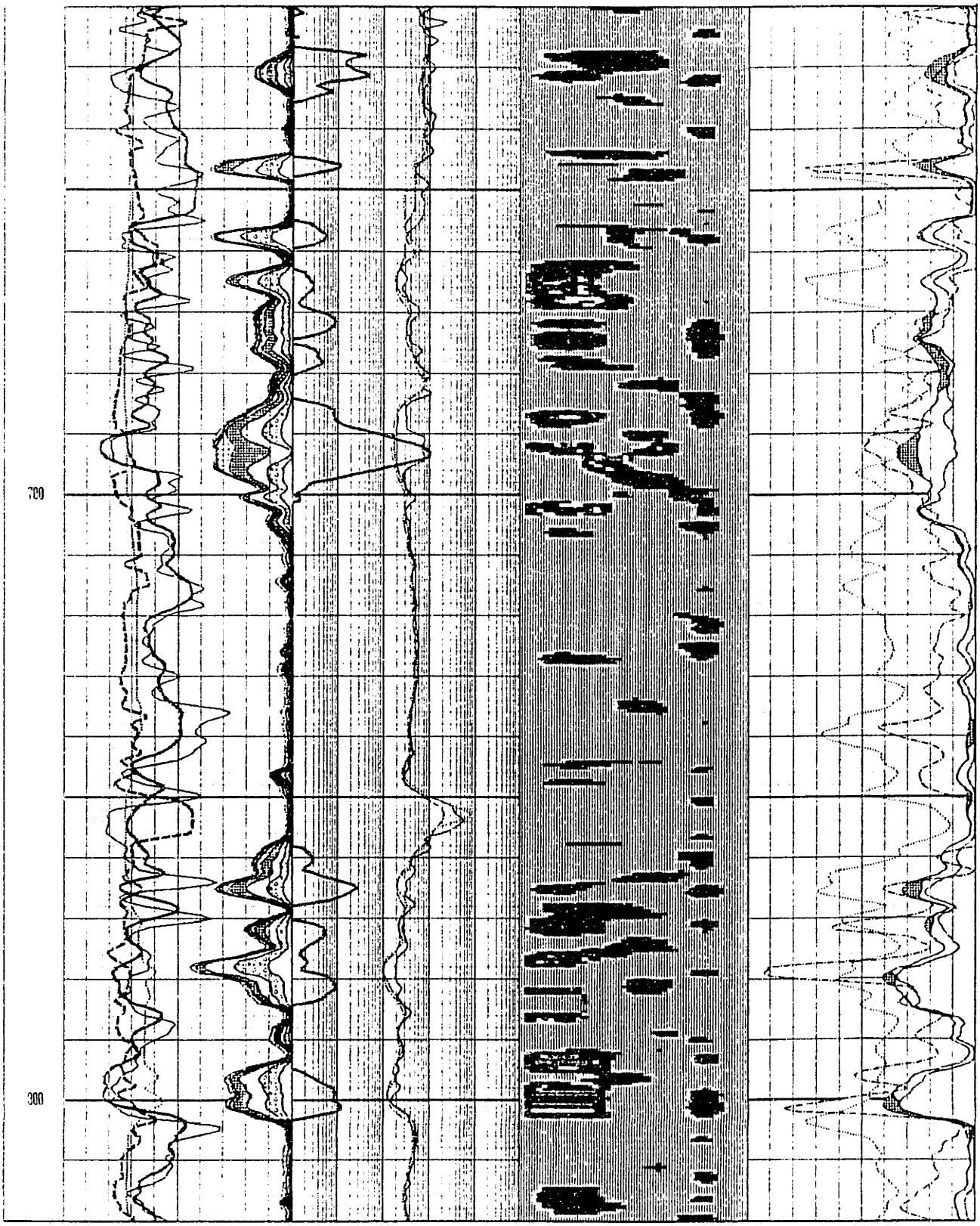

Figure 6.11 This fourth example is a repeat of Figure 5.12 except for the gas image in track 3. The zones have low porosity and a low signal-to-noise ratio causing artifacts in the early and late bins. The gas signal, although faint, shows up in most of the zones, and is strong from X692 to X696.

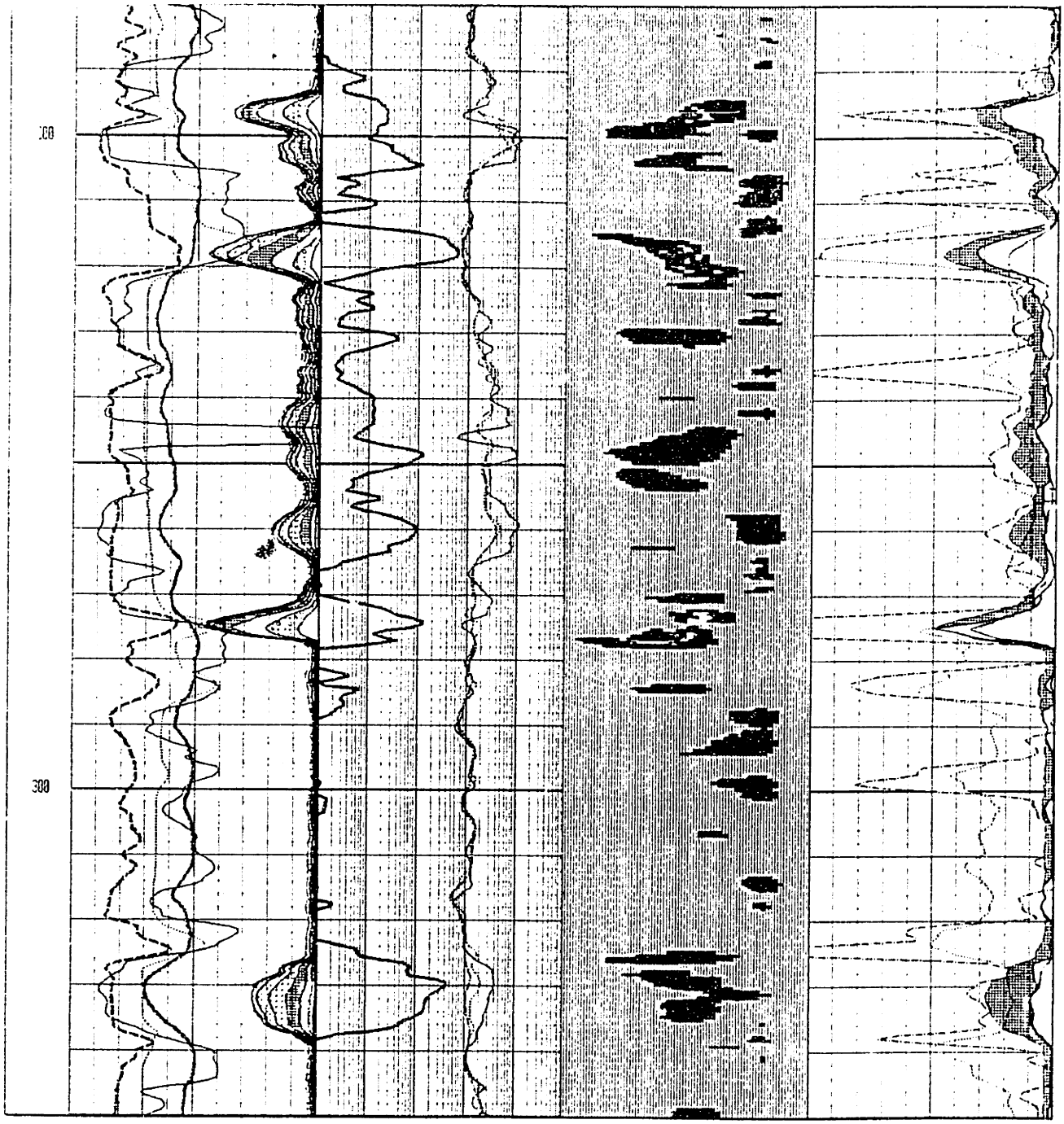

Figure 6.12 Example 5. This is a conventional zone from X325 to X338 with a strong, unrestricted gas signal in bin 4. Although the zone is thin and has only 8 pu of effective porosity, it tested at almost 1 MMCFPD.

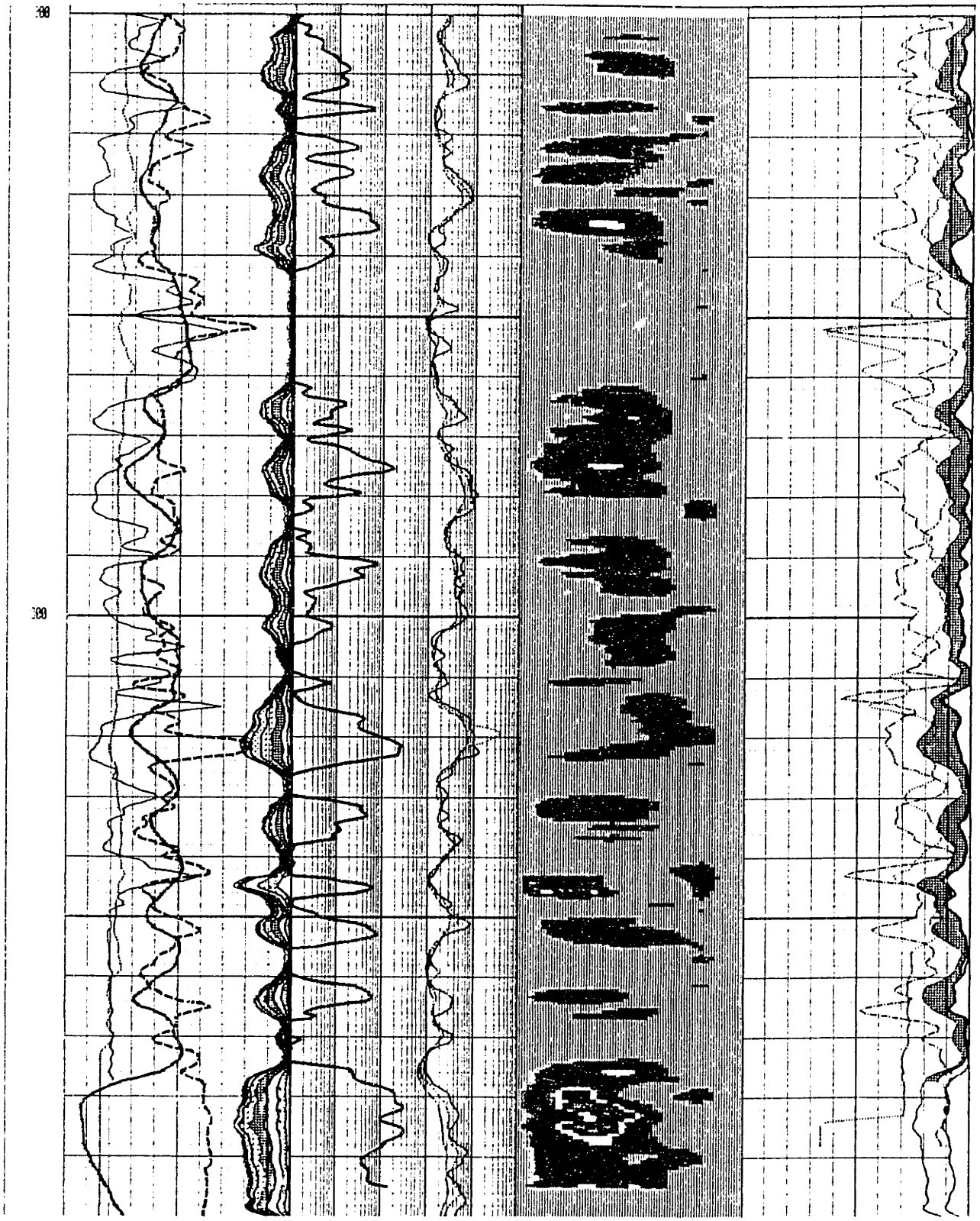

Figure 6.13 Example 6. This is a very prolific tight gas sand from X900 to X070. There is a strong gas signal throughout the interval. The missing porosity between the effective MPHI and the cross-plotted neutron–density results from the hydrogen index of the gas.

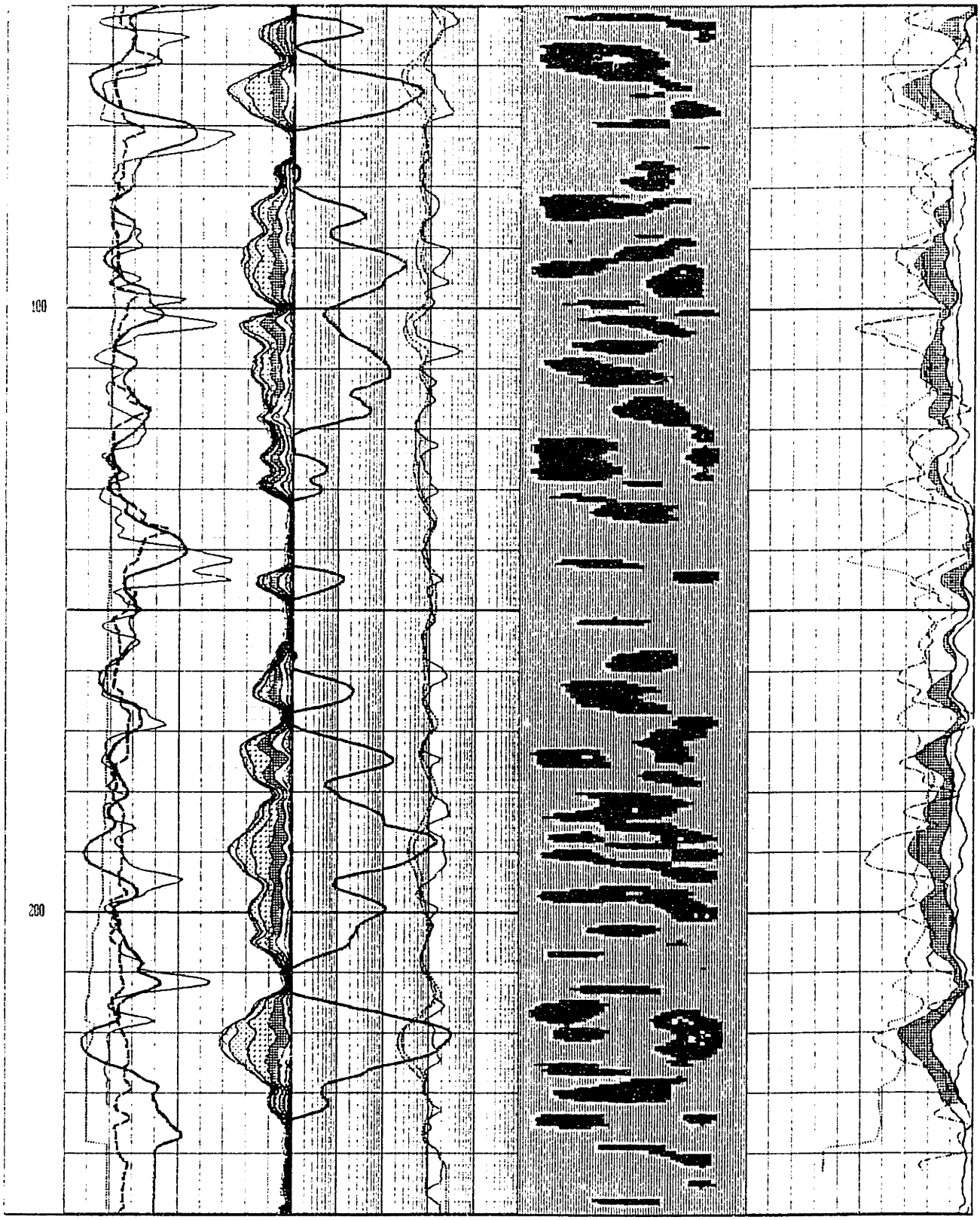

Figure 6.14 Example 7. The zone at X216 to X228 is an example of underrecovered water in bin 8. There is signal in the early and late bins of the differential, but no signal in bins 4 through 6, where the gas should be. Zone X060 to X070 has a gas signal in bin 5. The lower zone flowed water with little gas and the upper flowed gas with no water.

Chapter 7

Conclusion

This paper has described much of the basic physics of proton precession and the relaxivity mechanisms as well as the physical parameters that quantify NMR. While the hardware and processing of the NMR signals will change, the underlying physics remains constant. There are classical and quantum mechanical representations of the phenomenon, yet regardless of the description, we must always return to first principles to improve and better interpret the data acquired.

The CPMG pulse sequence was explained and the idea of T_1, T_2, and spin-density weighting of the pulse sequence in medial imaging was discussed. Also covered was the relation between medical imaging and optimum acquisition of NMR logging data. It was shown that short wait times lead to better BVI and improved measurement of small pores, whereas longer wait times are ideal in imaging larger pores, vugs, and hydrocarbons. A major conclusion of the thesis is the idea that changing the T_1 weighting changes the part of the T_2 spectrum we are focused on in logging. More than one pass of the tool is needed to cover the broad range of the T_2 spectrum, especially in the case of zones with very fine grain size and high BVI. In fact, in the limit it may be necessary to use specialized pulse sequences to measure the BVI and free fluid.

Chapters 5 and 6 provided many examples in which conventional methods of formation evaluation give incomplete or incorrect interpretations of the data. The novel approach has been used to enhance the reserves in many tight gas sands by finding bypassed pay. Further, the thesis NMR data have been used to optimize stimulation programs

through the avoidance of fracturing into zones with movable water.

Our discovery of the low-resistivity zones with smectite and illite clay, as shown in the examples, set off a flurry of exploration in the Cotton Valley trend of the East Texas Basin. This discovery can be extended to other formations and other basins. Now that we understand how to find these zones with NMR logs, we have also learned about their rock properties. Our model has grown to include the ability to predict the level of commercial success of these zones as well as how optimally to stimulate them.

The very silty sands with extremely high BVI are a second major discovery made using NMR logging. These zones were thought to be wet or simply underproductive because of low permeability. The insight into the extremely fine grain size given by the predominance of bins 1 through 4 has led to awareness that these zones are gas productive or simply are impermeable to any fluid. The result—finding an interval of sand that produced 5 to 10 MCFPD before stimulation versus 1.5 MMCFPD after fracturing—is unprecedented. These sands are anomalous because their poor reservoir quality allows them often to act as their own trap. These sands underscore the effectiveness of the NMR method for looking into the rock at the microscopic level with a downhole logging device. The petrophysical data approach the quality of core data with the added advantage of looking at the pore fluids as they exist in situ.

The thesis expanded on the differential spectrum method to optimize the data acquisition. The T_1 and T_2 relaxation mechanisms of water and hydrocarbons were discussed in detail. These characteristics of the pore fluids can be used to develop pulse sequences that enhance the contrast between the fluids, in much the same manner as in medical imaging. The thesis work has shown that the optimum way to acquire the NMR data is by using multiple wait times and observing how the bins change as a function of wait time. By studying the rate of the change of the bins, the quantities of the pore fluids as well as the amount of signal and noise can be obtained from the data.

In summary, the thesis is a novel approach to formation evaluation through the use of the T_2 distribution (the bins) and hydrocarbon imaging as the key inputs to the model. Conventional log data and well tests are integrated into the model, but the focus is the NMR response. The examples presented show that the evaluation is self-contained and often explains or clarifies ambiguities or contradictions in the other assessments. The research is ongoing as the science of NMR logging rapidly evolves. It is difficult at this point to predict just how significant this breakthrough in well logging will ultimately be.

References

Abragam, A., 1961, *Principles of Nuclear Magnetism*, Clarendon Press, Oxford.

Akkurt, R., Vinegar, H.J., Tutunjian, P.M., Guillory, A.J., 1995, "NMR Logging of Natural Gas Reserves," paper N presented at the 36th Annual Logging Symposium Transactions, Society of Professional Well Logging Analysts, Paris, France. Reprinted in *The Log Analyst*, volume 37, #6, pages 33 – 42.

Bushong, S.C., 1996, *Magnetic Resonance Imaging: Physical and Biological Principles*, Mosby, St. Louis, pages 72, 242–243.

Butler, J.P., Reeds, J.A., Dawson, S.V., 1981, "Estimating Solutions of First Kind Integral Equations with Nonnegative Constraints and Optimal Smoothing," *SIAM Journal of Numerical Analysis*, volume 18, page 381.

Carr, H.Y., Purcell, E.M., 1954, "Effects of Diffusion on Free Precession in Nuclear Magnetic Resonance Experiments," *Physical Review*, volume 94, pages 630–638.

Chandler, R.N., Drack, E.O., Miller, M.N., Prammer, M.G., 1994, "Improved Log Quality with a Dual-Frequency Pulsed NMR Tool," paper SPE 28365 presented at the 69th Annual Technical Conference and Exhibition, Society of Petroleum Engineers, New Orleans, LA, September 25-28, 1994.

Chandler, R.N., 1995, "Nuclear Magnetic Resonance Logging," Chapter 6 in *Course Notes from 36th Annual SPWLA Symposium*, Paris, France, June 26, 1995.

Cherry, R., 1995, Slide Presentation Master, NUMAR Corporation, Houston, TX.

Clavier, C., Coates, G., Dumanoir, J., 1984, "Theoretical and Experimental Bases for the Dual-Water Model for Interpretation of Shaly Sands," *The Society of Petroleum Engineers Journal*, volume 24, pages 153–168.

Coates, G.R., Vinegar, H.J., Tutunjian, P.N., Gardner, J.S., 1993, "Restrictive Diffusion from Uniform Gradient NMR Well Logging," SPE 26472 presented at the 68th Annual Technical Conference and Exhibition, Society of Petroleum Engineers, Houston, TX, October 3 – 6.

Coates, G.R., Gardner, J.S., Miller, D.L., 1994, "Applying Pulse-Echo NMR to Shaly Sand Formation Evaluation," presented at the 35th Annual Logging Symposium Transactions, Society of Professional Well Logging Analysts, Tulsa, OK, June.

Cohen, M.H., Mendelson, K.S., 1982, "Nuclear Magnetic Relaxation and the Internal Geometry of Sedimentary Rocks," *Journal of Applied Physics*, volume 53, page 1127.

Dewan, J.T., 1983, "Shaly Formation Interpretation," Chapter 7 in *Essentials of Modern Open-Hole Log Interpretation*, PennWell Books, Tulsa, pages 227–266.

Edwards, C.M., Chen, S., 1996, "Improved NMR Well Logs from Time-Dependent Echo Filtering," presented at the 37th Annual Logging Symposium Transactions, Society of Professional Well Logging Analysts, New Orleans, LA, June 16-19.

Ellis, D.V., 1987, "Nuclear Magnetic Logging," Chapter 14 in *Well Logging for Earth Scientists*, Elsevier, New York, pages 305–337.

Feynman, R.P., Leighton, R.B., Sands, M.L., 1965, *Feynman Lectures on Physics*, volume 2, Addison-Wesley, Reading, Massachusetts.

Horowitz, A.L., 1995, "Pulse Cycles, Pulse Sequences, and Tissue Contrast," Chapter 5 in *MRI Physics for Radiologists: A Visual Approach*, Springer-Verlag, New York, pages 33–37.

Jackson, J.A., 1984, "Nuclear Magnetic Resonance Well Logging," *The Log Analyst*, volume 25, pages 16–30.

Keller, P.J., 1988, "Basic Principles of Magnetic Resonance Imaging," GE Medical Systems, pages 5–12.

Kenyon, W.E., Day, P.I., Straley, C., Williamsen, J.F., 1988, "A Three-Part Study of NMR Longitudinal Relaxation Properties of Water-Saturated Sandstones," *SPE Formation Evaluation*, volume 3, pages 622–636. See also 1986, "Compact and Consistent Representation of Rock NMR Data for Permeability Estimation," SPE 15643 presented at the 61st Annual SPE Meeting, New Orleans, LA.

Kleinberg, R.L., Vinegar, H.J., 1996, "NMR Properties of Reservoir Fluids," *The Log Analyst*, volume 37, pages 20–32.

Lawson, C.L., Hanson, R.J., 1974, *Solving Least Squares Problems*, Prentice-Hall, Inc., Englewood Cliffs, New Jersey, page 161.

Leach, M.O., 1988, "Spatially Localised Nuclear Magnetic Resonance," Chapter 8 in *The Physics of Medical Imaging* (Webb, S., editor), Institute of Physics Publishing, Briston, page 389-487.

Meiboom, S., Gill, D., 1958, "Modified Spin-Echo Method for Measuring Nuclear Relaxation Times," *Review of Scientific Instrumentation*, volume 29, pages 688–691.

Miller, M.N., Paltiel, Z., Gillen, M.E., Granot, J., Bouton, J.C., 1990, "Spin Echo Magnetic Resonance Logging: Porosity and Free Fluid Index Determination," SPE 20561, presented at the 65th Annual Technical Conference and Exhibition, Society of Petroleum Engineers, New Orleans, LA, September 23 – 26.

Mitra, P.P., Sen, P.N., Schwartz, L.M., Le Doussal, P., 1992, "Diffusion Propagator as a Probe of the Structure of Porous Media" *Physical Review Letters*, volume 68, page 3555.

Morriss, C.E., 1995, "Nuclear Magnetic Resonance Logging," Chapter 7 in *Course Notes from 36th Annual SPWLA Symposium*, Paris, France, June 26.

Prammer, M.G., 1994, "NMR Pore Size Distributions and Permeability at the Well Site," SPE 28368 presented at the 69th Annual Technical Conference and Exhibition, Society of Petroleum Engineers, New Orleans, LA, September 25 – 28.

Press, W.H., Teukolsky, S.A., Vetterling, W.T., Flanners, B.P., 1988, *Numerical Recipes in C*, edition 2, Cambridge University Press, Cambridge.

Tikhonov, A.N., Arsenin, V., 1977, *Solutions of Ill-Posed Problems*, V.H. Winston & Sons, Washington, DC.

Timur, A., 1969, "Pulsed Nuclear Magnetic Resonance Studies of Porosity, Moveable Fluid, and Permeability of Sandstones," *Journal of Petroleum Technology*, volume 21, pages 775–786.

Waxman, M.H., Smits, L.J.M., 1968, "Electrical Conductivities in Oil-Bearing Shaly Sands," *The Society of Petroleum Engineers Journal*, June 1968, pages 107–122.

Appendix

NMR Inversion Theory

The time domain data from the NMR logging tool must be inverted into the T_2 domain in order to interpret the T_2 distribution of the sample (Prammer, 1994). The single decay of the echo data (Figure 3.3) can be characterized as being made up of a continuous distribution of decays $e^{-t/T2}$ with T_2 as the decay constant. The data from an NMR experiment y(t) can be written as

$$y(t) = \left[\int_{T_2=0}^{T_2^{bulk}} P(T_2)\, e^{(-t/T_2)}\, d(T_2) \right] + \varepsilon(t) \qquad (A.1)$$

where $P(T_2)$ is the T_2 distribution; and $e^{(-t/T_2)}$ represents a continuous convolution of exponential decays from $T_2 = 0$ to T_2 = the bulk relaxation of water; and $\varepsilon(t)$ is a vector that represents the noise in the data. Thus, the total effective porosity (MPHI) can be expressed as

$$MPHI = \int_{T_2=0}^{T_2 = \text{bulk relaxation}} P(T_2)\, d(T_2) \qquad (A.2)$$

Because of the noise in Equation A.1, the inversion is ill-posed (Tikhonov and Arsenin, 1977), giving many possible solutions. A method to uncover the true T_2 distribution $P(T_2)$ must be found.

Equation A.1 can be discretized and rewritten as a non-negative least-squares (NNLS) minimization:

$$\|Ax - y\|^2 \rightarrow \min \tag{A.3}$$

In the above equation, the elements of the motion, A_{ij}, are written

$$A_{ij} = e^{(-t_i/T_{2j})} \tag{A.4}$$

where t_i is the time of the ith echo and runs from 1 to N (the number of echoes) and T_{2j} is the T_2 of the jth bin and is equal to 2^{j+1} ms. Therefore, an example with 200 echoes and 8 bins would have A_{ij} as a 200 by 8 matrix. The x_j are the values for the partial porosity in each bin that the inversion scheme must solve for.

The inversion problem can be restated as:

$$y_i(t) = \mathbf{A}_{ij}\, x_j + \varepsilon_i;\ \ \mathbf{A}_{ij} = e^{(-t_i/T_{2j})} \tag{A.5}$$

The inversion of Equation A.3 is not stable because of the noise ε_i

Matrix A can be inverted using a singular-value decomposition (SVD) (Press, 1988). This method is used for solving most least-squares-type problems. Any M by N matrix with $M \geq N$ can be written as a product of an M by N column-orthogonal matrix **U** and an N by N diagonal matrix **W**, whose elements are ≥ 0 (the singular values) as well as the transpose of an N by N orthogonal matrix **V**.

$$\mathbf{A}=\mathbf{U}\begin{pmatrix} W_1 & & \\ & W_2 & \\ & & W_N \end{pmatrix}\mathbf{V}^T \tag{A.6}$$

From the above equation, the inverse of **A** is easily found

$$\mathbf{A}^{-1} = \mathbf{V} \cdot [\text{diag}\,(1/W_N)] \cdot \mathbf{U}^T \tag{A.7}$$

Where the inverse of **V** and **U** are their transposes because they are orthogonal matrices. The diagonal $(1/W_N)$ is N by N matrix of the inverse of the singular values. This becomes problematic if the W_N have any values equal to or near zero. The condition number of the matrix is the ratio of the largest to smallest of the W_N and is a measure of the singularity of the matrix. The matrix is singular if one of the $W_N = 0$ and ill-conditioned if the condition number is too large for the signal-to-noise ratio of the experiment or exceeds the precession of the measurement.

The vector space can be reduced and the inverse approximated if the $1/W_j$, which are at or near infinity, are replaced by 0. This form of regularization of the ill-conditioned, or singular, matrix is known as singular value tapering. How this method is applied for low signal-to-noise, as in NMR logging, affects the random and systematic errors of the solution. There are numerous regularization schemes that can be used. The MAP processing algorithm developed by M. G. Prammer of the NUMAR Corporation (Prammer, 1994) is optimized to solve for the inverse in NMR logging data:

$$\mathbf{X}=\mathbf{V}\cdot\left[\text{diag}\left(\frac{1}{W_1},\frac{1}{W_2},\ldots,\frac{SNR}{W_1},0,0,\ldots\right)\right]\cdot\mathbf{U}^T\mathbf{y} \tag{A.8}$$

using the signal-to-noise (SNR) characteristics of the data collected by the NMR log.

The taper term in the MAP regularization is a sharper cutoff than other methods such

as that of Tikhonov (Tikhonov and Arsenin, 1977). The taper term, SNR/W_1, is chosen such that the sequence $1/W_1$, $1/W_2$, ..., SNR/W_1 is monotonic and increasing. An example of this method would be as follows, if **A** represents an experiment with N = 200 echoes and 8 bins. The condition number is 7.9019×10^3. The 8 W_j and their inverse $1/W_j$ are:

$W_1 = 17.1739$	$1/W_1 = .0582$
$W_2 = 4.6653$	$1/W_2 = .2143$
$W_3 = 1.7318$	$1/W_3 = .5774$
$W_4 = .06654$	$1/W_4 = 1.5049$
$W_5 = 0.2403$	$1/W_5 = 4.1615$
$W_6 = 0.0791$	$1/W_6 = 12.6422$
$W_7 = 0.0233$	$1/W_7 = 42.9185$
$W_8 = 0.0022$	$1/W_8 = 454.5455$

If the taper is applied for the case of the SNR = 10, $SNR/W_1 = 0.5823$, the solution would be

$$\mathbf{X} = \mathbf{V} \cdot [\text{diag}(.0582,.2143,.5774,.5823,0,0,0,0)] \cdot (\mathbf{U}^T \mathbf{y}) \qquad (A.9)$$

To better describe why this regularization method is optimal, it is instructive to go back and study the general method of solution. Assuming white noise for $\varepsilon(t)$, the least-squares solution of Equation A.5 is

$$\Phi = \left\| A X_{LS} - y(t) \right\|^2 \rightarrow \min \qquad (A.10)$$

$$\frac{d\Phi}{dt} = 0 \qquad (A.11)$$

The least-squares solution is

$$X_{LS} = (A^T A)^{-1} A^T y \qquad (A.12)$$

This is one of many possible solutions, but not necessarily physical because of the destabilizing effect of the noise ε(t). Using the method of M. M. Lavrent'yev (Tikhonov and Arsenin, 1977), the problem can be regularized as:

$$\Phi = \|\mathbf{A}x - y\|^2 + \alpha \|\mathbf{B}x\|^2 \rightarrow \min \tag{A.13}$$

The second term penalizes all solutions that deviate from the physical solution. There are many possible regularization methods (Press, 1992). One method of inversion is the Tikhonov solution, where $\mathbf{B} = \mathbf{I}$:

$$\mathbf{X}_{TIK} = (\mathbf{A}^T\mathbf{A} + \alpha\mathbf{I})^{-1}\,\mathbf{A}^T\mathbf{y} \tag{A.14}$$

where α boosts the eigenvalue of $\mathbf{A}^T\mathbf{A}$ to stabilize the matrix inversion. The α is chosen to be optimum in the trade-off curve for the problem in question. The Butler–Reeds–Dawson method (Butler, et al., 1981) solves Equation A.14 under the constraint of the NNLS by a method of searching to find the optimum α.

For large condition numbers, the noise ε causes the X_{LS} to become unstable, so some form of tapering must be done. The Tikhonov solution can be written

$$\mathbf{X}_{TIK} = \mathbf{V} \cdot \left[\mathrm{diag}\left(\frac{W_i}{W_i^{\,2} + \alpha};\quad i = 1 \ldots M \right) \right] \cdot (\mathbf{U}^T\mathbf{y}) \tag{A.15}$$

This is another form of SVD tapering, as in the MAP solution (Equation A.8). When the SNR falls below a minimum threshold, the shortest T_2 values are gradually attenuated in the Tikhonov approach and more sharply cut off in the MAP SVD tapering approach.

There are two ways to solve for the X_{LS} using the SVD tapering approach, and

assuming that, $x_i \geq 0$. The first method involves using the Lawson and Hanson (Lawson and Hanson, 1974) non negative least-squares approach, but putting the tapered solution into the problem when the untapered solution is called for in the algorithm.

The second method to apply the tapering in MAP is an iterative process. The problem is solved with the x_i both positive and negative and then the negative components are rejected (Press, 1988). Begin by solving for all bin values, x_i, if none are negative, then the x_i are accepted. If some are negative, start with the most negative x_i, and get rid of the column in A corresponding to this component. This component is set equal to zero and the process is repeated with a reduced matrix, A', and a new solution, x_i', now with $i < M$. Once all the negative elements are reduced, the SVD tapering in Equation A.8 is applied to solve for x_i.

To find the SNR term in Equation A.8, the following approach is used in MAP processing:

$$\mathrm{SNR} = \frac{\text{amplitude of 3rd echo}}{< \delta_i >} \tag{A.16}$$

$$\hat{x} = V \cdot \frac{1}{S} \cdot (\mathbf{U}^T \mathbf{y}); \quad \hat{x}_i \geq 0 \tag{A.17}$$

$$\delta = y - A\hat{x} \tag{A.18}$$

In the above equations, $\hat{x}$ is the trial NNLS solution, δ is the difference in the real data, and the final solution, $\langle |\delta| \rangle$, is the standard deviation of the elements of the vector δ.

The last step of the method is to estimate the phase and magnitude of the echoes. The NMR data has a magnitude and phase influenced by the antenna loading. The phase can be

corrected for and used in the final processing. The phase of the third through ninth (or more, if needed) echoes can be averaged (θ_{AVG}). The corrected magnitude can then be found:

$$y_i'(t) = \|y_i(t)\| \; \mathrm{Re}\left(e^{i(\theta - \theta_{AVG})}\right) \tag{A.19}$$

The $y_i'(t)$ is then input into Equation A.8 for y and the process is continued.

An alternative method for correcting for the phase or magnitude of the data is as follows. The data are biased or have rectified noise for the later echoes. The bins can be corrected by using the RMS of the echoes.

$$y_i'(t) = \mathrm{sgn}(y^2 - 1.5\hat{\sigma}^2)\sqrt{y^2 - 1.5\hat{\sigma}^2} \tag{A.20}$$

In this case, $\hat{\sigma}^2$ is the squared standard deviation of the elements of the vector δ. The $y_i'(t)$ is once again substituted for y in Equation A.8 and the process is continued.